JAERI-M
87-001

EVALUATION REPORT ON CCTF CORE-II REFLOOD TEST C2-8 (Run 67) —EFFECT OF SYSTEM PRESSURE—

January 1987

Hajime AKIMOTO, Tadashi IGUCHI, Kazuharu OKABE*
Jun SUGIMOTO,** Tsutomu OKUBO and Yoshio MURAO

日本原子力研究所
Japan Atomic Energy Research Institute

JAERI-Mレポートは，日本原子力研究所が不定期に公刊している研究報告書です。
入手の問合わせは，日本原子力研究所技術情報部情報資料課（〒319－11茨城県那珂郡東海村）あて，お申しこしください。なお，このほかに財団法人原子力弘済会資料センター（〒319-11茨城県那珂郡東海村日本原子力研究所内）で複写による実費頒布をおこなっております。

JAERI-M reports are issued irregularly.
Inquiries about availability of the reports should be addressed to Information Division, Department of Technical Information, Japan Atomic Energy Research Institute, Tokai-mura, Naka-gun, Ibaraki-ken 319-11, Japan.

編集兼発行　日本原子力研究所
印　　刷　日立高速印刷株式会社

Evaluation Report on CCTF Core-II Reflood Test C2-8 (Run 67) - Effect of system pressure -

Hajime AKIMOTO, Tadashi IGUCHI, Kazuharu OKABE*
Jun SUGIMOTO**, Tsutomu OKUBO and Yoshio MURAO
Department of Reactor Safety Research,
Tokai Research Establishment,
Japan Atomic Energy Research Institute
Tokai-mura, Naka-gun, Ibaraki-ken

(Received January 8, 1987)

In order to study the system pressure effect of the core cooling and flow behavior during the reflood phase of a PWR LOCA, a test was performed with CCTF under the system pressure of 0.15 MPa as a counterpart test of the CCTF test C2-1 (system pressure 0.42 MPa) and the CCTF test C2-4 (system pressure 0.20 MPa). Through the comparisons of results from these three tests, the following conclusions were obtained:

(1) The higher system pressure resulted in the lower temperature rise, the shorter turnaround time and the shorter quench time as observed in the CCTF Core-I system pressure effect tests. Based on the correlation developed by Murao and Sugimoto(8), it is confirmed that the increase in the core heat transfer with the system pressure is attributed to the increase of the steam density in the early period (before 60 s). In the later period (after 60 s), the core heat transfer rate is increased with the system pressure due to the effect of the local void fraction and the distance from the quench front in addition to the effect of the steam density.

The work was performed under the contract with the Atomic Energy Bureau of Science and Technology Agency of Japan.

* Mitsubishi Atomic Power Industry

** Science and Technology Agency of Japan

(2) The higher system pressure resulted in higher core water head, higher upper plenum water head, higher mass flow rate through the primary loops. On the other hand, the higher system pressure resulted in lower downcomer water head and lower pressure drop through the primary loops and the broken cold leg. These system pressure effects on the flow behavior in the primary system are almost the same as observed in the system pressure effect tests in the CCTF Core-I test series.
(3) Before the mixture level in the upper plenum reached the level of the hot leg nozzle, the loop flow resistance coefficient of the intact loops was nearly constant regardless of the system pressure. After the mixture level reached the level of the hot leg nozzle, the loop flow resistance coefficient was increased due to the water accumulation in the hot leg piping and the inlet plenum of the steam generator in these tests.

Keywords: Reactor Safety, Loss-of-coolant, PWR, Reflood, Pressure Effect, CCTF, Heat Transfer, Two-phase Flow

大型再冠水円筒第2次炉心試験C2－8（Run 67）評価報告書
― 系圧力効果 ―

日本原子力研究所東海研究所原子炉安全工学部
秋本　肇・井口　正・岡部　一治*
杉本　純**・大久保　努・村尾　良夫

（1987年1月8日受理）

加圧水型原子炉の冷却材喪失事故再冠水期における炉心冷却と一次系内の流動に対する系圧力の影響を調べるために，円筒第2次炉心試験装置を用いて系圧力0.15MPaでの試験を行った。本試験はすでに実施された試験C2－1（系圧力0.42MPa）と試験C2－4（系圧力0.20MPa）と対をなす円筒第2次炉心試験装置による系圧力パラメータ試験のひとつである。上述の試験結果を比較検討した結果，以下の事柄が明らかとなった。

(1) 系圧力が高くなると，温度上昇は低く，ターンアラウンド時間は短かく，クエンチ時間は短かくなった。これらの傾向は，円筒第1次炉心試験での観察結果と同様であった。村尾・杉本による熱伝達率相関式で検討した結果，初期（60秒以前）では蒸気密度が大きくなることのために高系圧力下での熱伝達率が高くなることがわかった。また後期（60秒以降）では，蒸気密度の効果に加えて，局所ボイド率とクエンチ点からの距離が影響して熱伝達率を高めていることがわかった。

(2) 系圧力が高くなると，炉心水頭・上部プレナム水頭・一次系ループ流量は増加した。一方ダウンカマ水頭・一次系ループ差圧・破断コールドレグ差圧は高系圧力下で減少した。一次系内の流動に対するこれらの系圧力効果は，円筒第1次炉心試験での観察結果と同様であった。

(3) 上部プレナム内の二相混合体の液位がホットレグ取付け高さに到達するまでの期間においては，健全ループの流動抵抗係数は系圧力によらずほぼ一定であった。液位がホットレグ取付高さまで到達した後では，健全ループの流動抵抗係数は，ホットレグ配管への蓄水と蒸気発生器入口プレナムへの蓄水により増加した。

東海研究所：〒319－11　茨城県那珂郡東海村白方字白根2－4
本報告書は，電源開発促進対策特別会計法に基づき，科学技術庁からの受託によって行った研究の成果である。
* 三菱原子力工業
** 科学技術庁

Contents

目　　次

List of tables

List of figures

1.Introduction

A reflood test program using large scale test facilities has been conducted at Japan Atomic Energy Research Institute(JAERI)[1]-[4]. The facilities are the Cylindrical Core Test Facility(CCTF) and the Slab Core Test Facility(SCTF). This report presents an evaluation for the CCTF test C2-8(Run 67), which was performed with CCTF at system pressure of 0.15 MPa on July 6,1983.

The CCTF is an experimental facility designed to model a full-height core section and four primary loops and their components of a pressurized water reactor(PWR). This facility is used to provide information of thermal-hydraulic behaviors in pressure vessel (core, downcomer and upper and lower plenums) and in primary loops including steam generator and pump simulator during the refill and reflood phases of a hypothetical loss-of-coolant accident(LOCA) of a PWR.

The objectives of the test program using the CCTF are:

a. Demonstration of capability of emergency core cooling system (ECCS) during refill and reflood phases.
b. Verification of reflood analysis codes.
c. Collection of information to improve the thermal-hydralic models in the analysis codes.

As the first series of the CCTF test, the CCTF Core-I series was initiated in March 1979 and completed in April 1981. Subsequently, as the second series of the CCTF tests, the CCTF Core-II series was initiated in March 1982.

The main objective of the CCTF test C2-8(Run 67) is to study the system pressure effect on the system and core cooling behavior. The test was performed at the system pressure of 0.15 MPa as the counterpart test of the CCTF test C2-1(system pressure 0.42 MPa) and the CCTF test C2-4(system pressure 0.20 MPa) in the CCTF-II series. In the CCTF test C2-8, the other test conditions except the system pressure was planned to be identical with the CCTF tests C2-1 and C2-4.

This report presents the results from the CCTF test C2-8 in comparison with the results from the high pressure and the base case tests for reviewing of the test data and the system pressure effect.

In this report, the tests C2-1, C2-4 and C2-9 will be called "high pressure", "base case" or "low pressure" tests, respectively.

2. Test description

2.1 Test facility

A bird's eye view and schematic diagram of the CCTF are shown in Figs. 2.1 and 2.2, respectively. The scaled dimensions of the components are given in Tables 2.1 and 2.2.

2.1.1 Pressure vessel and internals

The pressure vessel is of a cylindrical type as shown in Fig. 2.3. The height is the same as the reference reactor pressure vessel. The dimension in the radial direction is scaled down based on the core flow area scaling, that is, 1/21.44. The upper ring was newly attached for the installation of the upper plenum ECC water injection lines and the instruments. Four vent valves and two downcomer water injection nozzles, which are called Core Flooding Nozzle(CFN), are also newly installed in the CCTF Core-II facility as shown in Figs. 2.3 and 2.4. Vent valves and CFNs are forcedly closed in the low pressure test.

The cross section of the pressure vessel is shown in Fig. 2.5. The dimensions of the pressure vessel is shown in Fig. 2.5. The core consists of thirty-two 8x8 rod bundles arranged in a cylindrical configuration. The rod bundles simulate Westinghouse 15x15 type fuel assemblies.

The downcomer is an annulus of 61.5 mm gap. In determining the gap size, the flow area of the core baffle region was added to that of the downcomer region. Thus, the core baffle flow area is included in the downcomer simulation in the CCTF. The vessel wall is constructed of carbon steel cladded with stainless steel lining. The wall thickness is 90 mm.

The design of upper plenum internals is based on that of the Westinghouse PWR with 17x17 type fuel assembly. The internals cosists of ten control-rod guide tubes, ten support columns and twelve open holes as shown in Fig. 2.6. The configuration of each intenal is illustrated in Fig. 2.7. The radius of each internal is scaled down by factor of 8/15 from that of a PWR. Flow resistance baffle plates are inserted into the guide tubes. Figure 2.8 shows the configurations of the baffle plates.

The end box and the upper core support plate(UCSP) are installed above the core. Figure 2.9 shows the structure of the end box tie plate for one heater rod bundle. The tie plate is a perforated plate 10 mm

thick. Plugging devices are installed in the CCTF-II facility in order to simulate the flow resistance more correctly as shown in Figs. 2.9 and 2.10. The UCSP is a perforated plate 60 mm thick.

2.1.2 Heater rod assembly

Figure 2.11 shows arrangement of heater rods in a bundle. Each bundle consists of fifty-seven heater rods and seven non-heated rods. All heater rods in a bundle have the same power density in the CCTF-II facility. As shown in Fig. 2.5, the core is subdivided into three regions to achieve a desired radial power profile.

Figure 2.12 shows the configuration of a heater rod. A heater rod consists of nichrome heating element, magnesium oxide(MgO) and boron nitride(BN) insulators, and inconel-600 sheath. BN is used only for the central part of the heated part. The length of the core heated part is 3.66 m and the diameter of the heater rod is 10.7 mm. The thickness of the sheath wall is 1.0 mm. By changing the pitch of the helical coil of the heating element, a 17-step chopped-cosine axial-power profile is attained as shown in Fig. 2.13. The axial peaking factor is 1.40 in the CCTF-II, instead of 1.489 in the CCTF-I.

Non-heated rods are either stainless steel pipe or solid pipe of 13.8 mm O.D. All pipes are utilized for installation of instruments such as superheat steam probes and thermocouples. All bars are used to support the assembly loads.

The heater rods and non-heated rods are held in radial position by grid spacers which are located at six elevations along the axial length as shown in Fig. 2.13. A grid spacer is a lattice composed of stainless plates of 0.4 and 0.8 mm thick and 40 mm high. The top and bottom edges of the stainless steel plates are sharpened in the CCTF-II.

The heater rods penetrate through the bottom plate of the pressure vessel to facilitate the connection of the power cables. The outer diameter of the heater rods in the lower plenum is reduced to 8.6 mm.

2.1.3 Primary loops and ECCS

The CCTF has three intact and a broken loops. The facility simulates the double-ended cold-leg break. Figures 2.14 and 2.15 show the primary loop arrangement in the CCTF. The inside diameter of the pipings is scaled down in proportion to the core flow area scaling. The length of each piping section is almost the same as the corresponding sections of the reference PWR.

Figure 2.16 shows the steam generator(SG) simulator. The SG is of U-tube and shell type. The primary coolant passes through the tubes. The secondary side is filled with water. The steam generator simulators of two loops are housed in a single shell assembly. The wall thickness of the U-tube is 2.9 mm instead of 1.27 mm in the reference PWR system because of higher pressure difference between the primary and secondary sides.

The pump simulator consists of the casing and vane simulators and an orifice plate as shown in Fig. 2.17. The each loop flow resistance is simulated with the orifice plate.

ECC water can be injected into each cold leg, lower plenum, upper plenum, and downcomer as shown in Fig. 2.14.

Figure 2.18 shows the upper plenum injection device. The radial locations of the water injection pipes are shown in Fig. 2.19.

2.1.4 Instrumentation

The instrumentation is divided into two groups. One is JAERI-supplied instruments. The other is the USNRC supplied instruments.

JAERI instrumentation includes 1316 channels and is recorded on magnetic tapes. The measuring location of the selected data is summarized in Appendix A.

USNRC supplied instruments include the advanced instrumentation for the two-phase flow measurement. 536 channels are used to record data from these instruments. Table 2.3 show the names and quantities of these instruments.

2.2 Planned test procedure

In the preparation for the test, the Acc tank, the LPCI tank, the saturated water tank, and the secondary side of the steam generators were filled with water which was purified with ion exchange resin. After all the components and instruments were inspected for mechanical and electrical leakages, the instruments were checked for their zero points and sensitivities.

After these preparatory operations, the primary system was heated to the specified temperatures (downcomer wall:461 K, core internals: 383 K, and the primary piping wall: 383 K) and pressurized to a specified pressure (0.15 MPa) by introduing steam into the primary system. The water in the Acc and LPCI tanks was heated to the specified temperature(308 K). The water in the LPCI tank was circulated through the

circulation line to preheat the line to the same temperature as the LPCI water. The water in the saturated water tank was preheated to the saturation temperature(383 K) at the expected primary system pressure(0.15 MPa). The water in the secondary side of each steam generator was also heated and pressurized to the specified temperature(539 K) and pressure(5.2 MPa).

After establishing these initial conditions of the test, the lower plenum was filled with the saturated water to the specified level(0.90 m from the bottom of the pressure vessel). When all initial test conditions were stabilized at the allowable tolerance, electric power was supplied to the heater rods in the core and the data recording was started. The temperature rises of the rods were monitored by using a computer. When a specified clad surface temperature(995 K) was attained at more than 4 monitoring locations of the clad surface temperatures, Acc water injection into the lower plenum was initiated(injection rate: 0.105 m^3/s). The clad surface temperature (995 K) of the heater rods for the initiation of the Acc injection into the lower plenum was predetermined by the interpolation of the clad surface temperatures at the test initiation(383 K) and the reflood initiation(1073 K). The core power decay was programmed to begin when the water level in the pressure vessel was estimated to reach the bottom of the core heated part. The core power decay followed the normarized decay curve of (ANSx1.2 + Actinidex1.1(30 s after scram)).

When the water level in the pressure vessel was estimated to reach the specified level(0.5 m from the bottom of the core heated part) the injection location of Acc water was changed from the lower plenum to the ECC ports in the intact cold legs. The Acc injection into the cold legs was planned to be 0.0892 m^3/s for 11 s. This is defined as the Acc mode in the CCTF tests. After a specified time(11 s), the valves in the Acc lines and the LPCI circulation line began to close. The valves in the LPCI injection lines started openning at the same time in order to switch the ECC water injection mode. The ECC water injection was planned to be 0.0111 m^3/s. This ECC water injection is defined as the LPCI mode in the CCTF tests.

The generated steam in core flowed with the entrained water via primary loops to the containment tanks. The steam was then exhausted to the atmosphere through the flow control valve. The pressure in the containment tank was maintained at the specified level(0.15 MPa). After all thermocouples on the surface of the heater rods were quenched, the power supply to the heater rods and the ECC water injection were terminated. Then, the data recording system was stopped.

Table 2.1 CCTF Component scaled dimensions

Component		PWR	CCTF	Ratio
Pressure vessel				
Vessel inside diameter	(mm)	4394 (173")	1084	
Vessel thickness	(mm)	216 (8 1/2")	90	
Core barrel outside diameter	(mm)	3874	961	
Core barrel inside diameter	(mm)	3760	929	
Thermal shield outside diameter	(mm)	4170		
Thermal shield inside diameter	(mm)	4030		
Downcomer length	(mm)	4849	4849	1/1
Downcomer gap	(mm)	114.3	61.5	
Downcomer flow area	(m^2)	4.23	0.197	1/21.44
Lower plenum volume	(m^3)	29.6	1.38	1/21.44
Upper plenum volume	(m^3)	43.6	2.76	1/15.8
Fuel (heater rod) assembly				
Number of bundles	(—)	193	32	
Rod array	(—)	15×15	8×8	
Rod heated length	(mm)	3660	3660	1/1
Rod pitch	(mm)	14.3	14.3	1/1
Fuel rod outside diameter	(mm)	10.72	10.7	1/1
Thimble tube diameter	(mm)	13.87	13.8	1/1
Instrument tube diameter	(mm)	13.87	13.8	1/1
Number of heater rods	(—)	39372	1824	1/21.58
Number of non-heated rods	(—)	4053	244	1/18.09
Core flow area	(m^2)	5.29	0.25	1/21.2
Core fluid volume	(m^3)	17.95	0.915	1/19.6
Primary loop				
Hot leg inside diameter	(mm)	736.6 (29")	155.2	1/4.75
Hot leg flow area	(m^2)	0.426	0.019	1/22.54
Hot leg length	(mm)	3940	3940	1/1
Pump suction inside diameter	(mm)	787.4 (31")	155.2	1/5.07
Pump suction flow area	(m^2)	0.487	0.019	1/25.77
Pump suction length	(mm)	9750	7950	1/1

Table 2.1 (cont'd)

Component		PWR	CCTF	Ratio
Cold leg inside diameter	(mm)	698.5 (27.5")	155.2	1/4.50
Cold leg flow area	(m^2)	0.383	0.019	1/20.26
Cold leg length	(mm)	5600	5600	1/1
Steam generator simulator				
Number of tubes/loop	(—)	3388	158	1/21.44
Tube length (average)	(m)	20.5	15.2	1/1.35
Tube outside diameter	(mm)	22.225 (0.875")	25.4	
Tube inside diameter	(mm)	19.7 (0.05")	19.6	1/1
Tube wall thickness	(mm)	1.27	2.9	
Heat transfer area/loop	(m^3)	4784 (51500 ft^2)	192	1/24.92
Tube flow area/loop	(m^2)	1.03	0.048	1/21.44
Inlet plenum volume/loop	(m^3)	4.25	0.198	1/21.44
Outlet plenum volume/loop	(m^3)	4.25	0.198	1/21.44
Primary side volume/loop	(m^3)	30.50 (1077 ft^3)	1.2	1/25.4
Secondary side volume/loop	(m^3)	157.33 (5556 ft^3)	2.5	1/62.9
Containment tank 1	(m^3)		30	
Containment tank 2	(m^3)		50	
Storage tank	(m^3)		25	
Acc. tank	(m^3)		5	
Saturated water tank	(m^3)		3.5	

Table 2.2 Component elevations of Cylindrical Core Test Facility

COMPONENT		PWR	CCTF	DISCREPANCY
BOTTOM OF HEATED REGION IN CORE	(mm)	0	0	0
TOP OF HEATED REGION IN CORE	(mm)	3660	3660	0
TOP OF DOWNCOMER	(mm)	4849	4849	0
BOTTOM OF DOWNCOMER	(mm)	0	0	0
CENTERLINE OF COLD LEG	(mm)	5198	4927	-271
BOTTOM OF COLD LEG (INSIDE)	(mm)	4849	4849	0
CENTERLINE OF LOOP SEAL LOWER END	(mm)	2056	2047	- 9
BOTTOM OF LOOP SEAL LOWER END	(mm)	1662	1959	+297
CENTER OF HOT LEG	(mm)	5198	4927	-271
BOTTOM OF HOT LEG (INSIDE)	(mm)	4830	4849	+ 19
BOTTOM OF UPPER CORE PLATE	(mm)	3957	3957	0
TOP OF LOWER CORE PLATE	(mm)	- 108	- 50	+ 58
BOTTOM OF TUBE SHEET OF STEAM GENERATOR SIMULATOR	(mm)	7308	7307	- 1
LOWER END OF STEAM GENERATOR SIMULATOR PLENUM	(mm)	5713	5712	- 1
TOP OF TUBES OF STEAM GENERATOR SIMULATOR (avg)	(mm)	17952.7	14820	

Table 2.3 Instruments provided by USNRC

Instrument	Number of sets	Number of sensors
DC FDG	18	162
DC VOP	1	1
DC drag disk	4	4
Core velocimeter	4	4
Core impedance probe	12	24
Core LLD	6	96
LP LLD	3	15
End box turbine meter	8	8
UP turbine meter	4	4
UP FDG	11	110
UP film probe	2	4
UP prong probe	2	4
UP VOP	1	1
VV turbine meter	2	2
VV string probe	2	2
HL film probe	2	4
HL VOP	1	1
Reference probe	1	1
Spool piece	8	89
Total	92	536

Note :

DC : Downcomer, FDG: Fluid distribution grid,
VOP: Video optical probe, LLD: Liquid level detector,
LP : Lower plenum, UP : Upper plenum,
VV : Vent valve

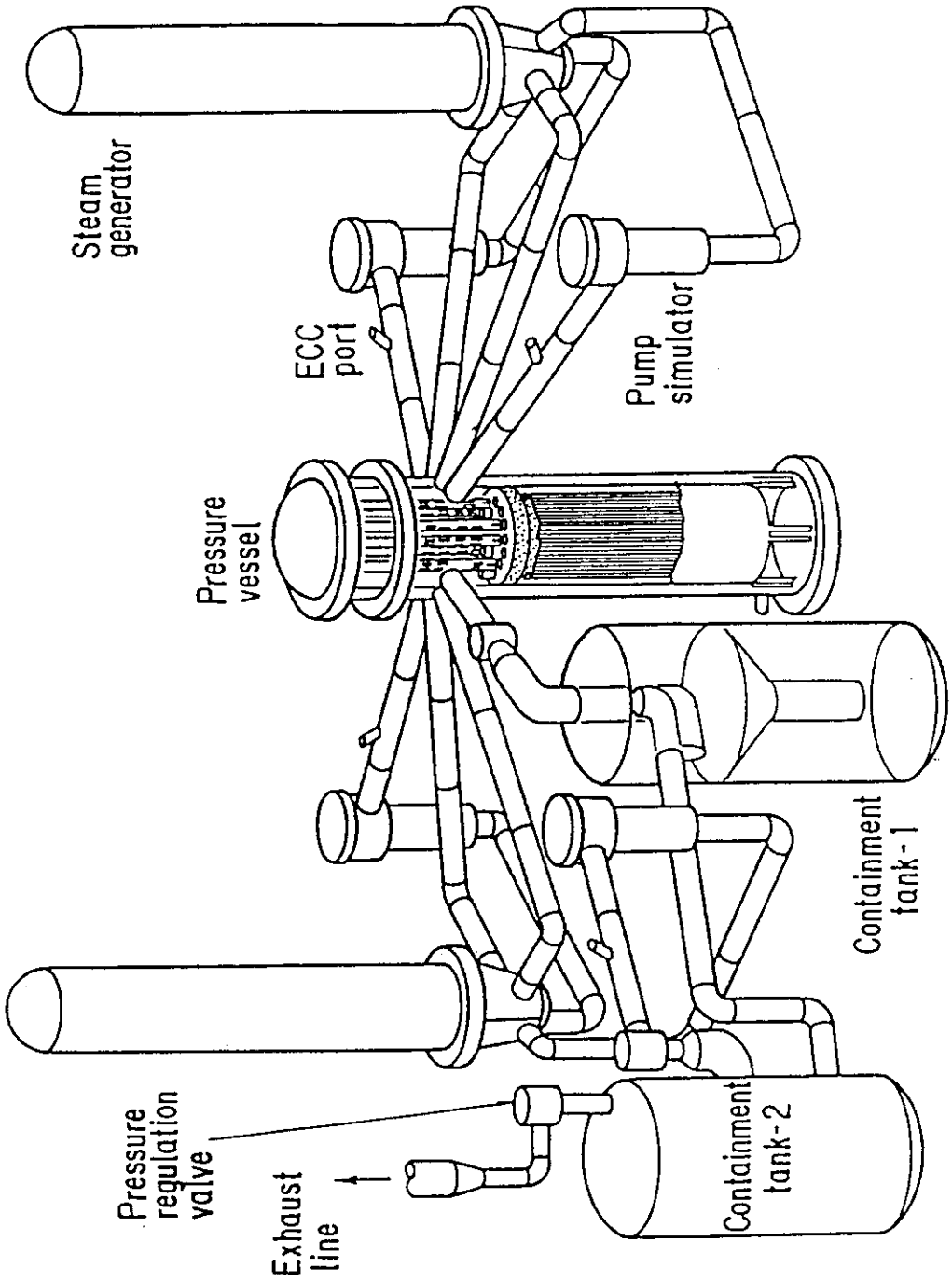

Fig. 2.1 Bird's-eye view of CCTF

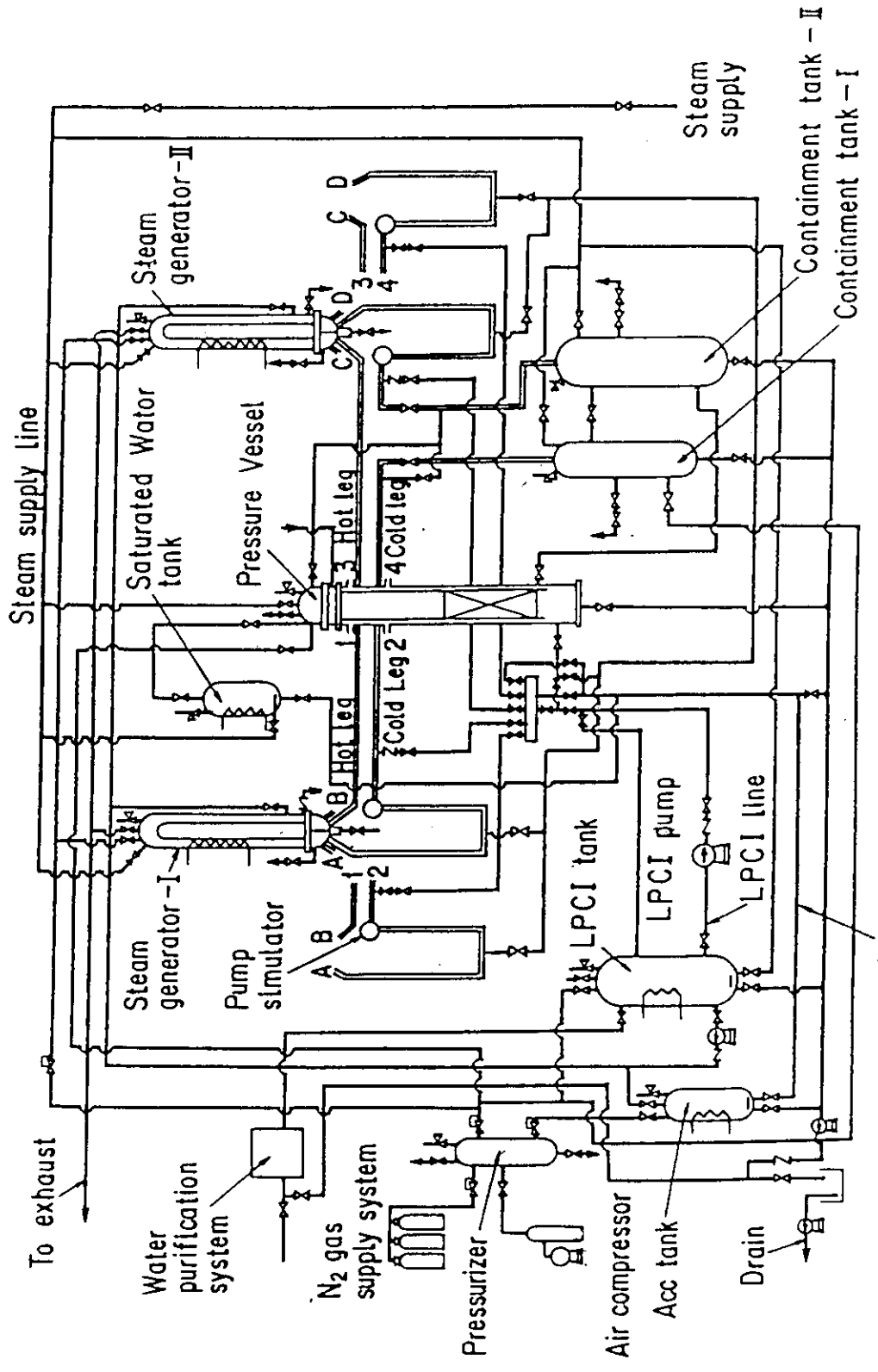

Fig. 2.2 Schematic diagram of CCTF

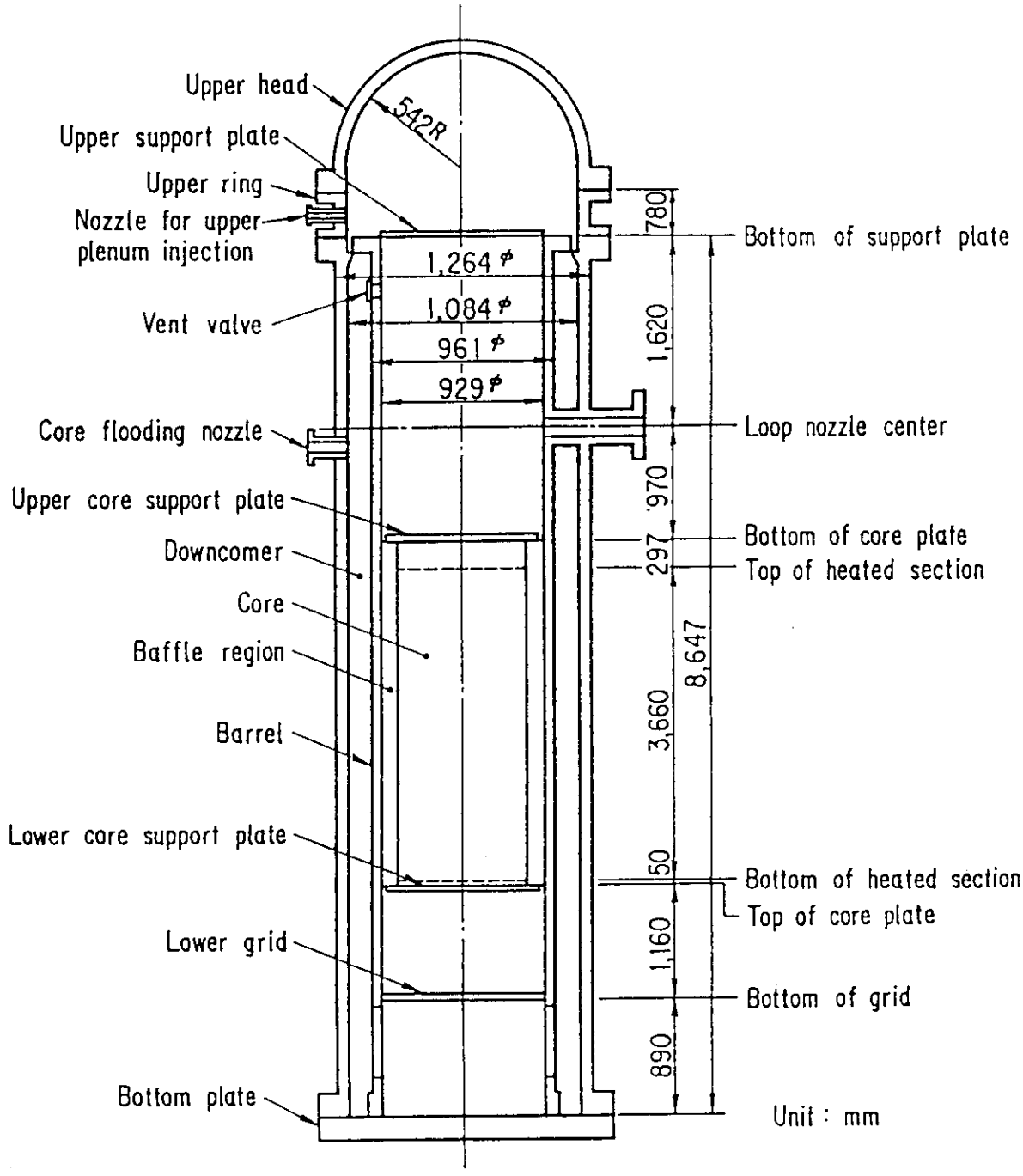

Fig. 2.3 CCTF Core-II pressure vessel

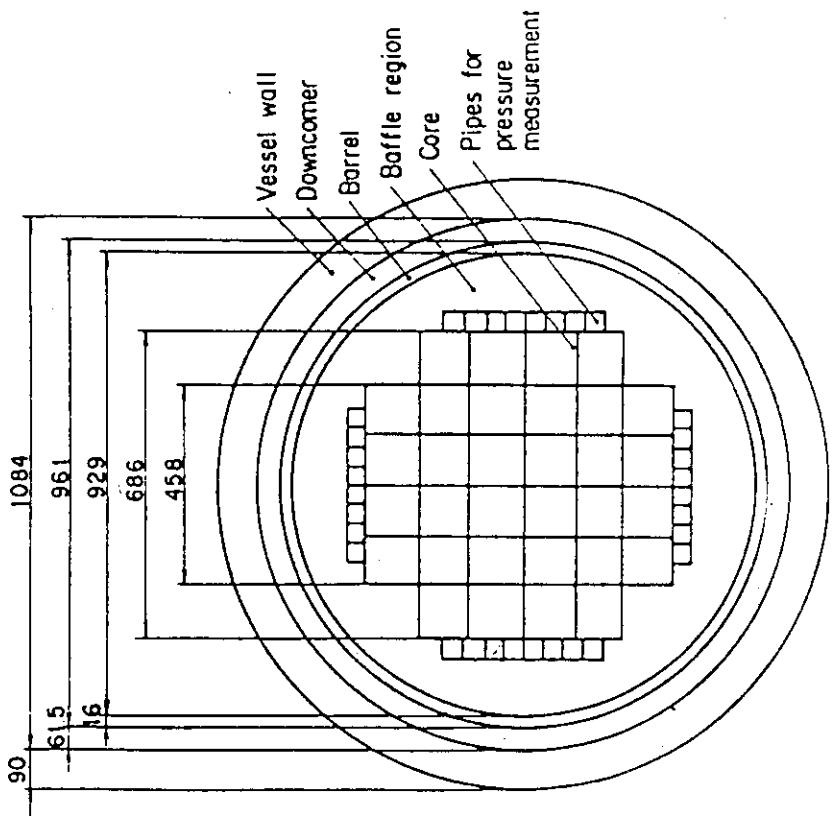

Fig. 2.5 Dimension of CCTF Core-II pressure vessel cross section

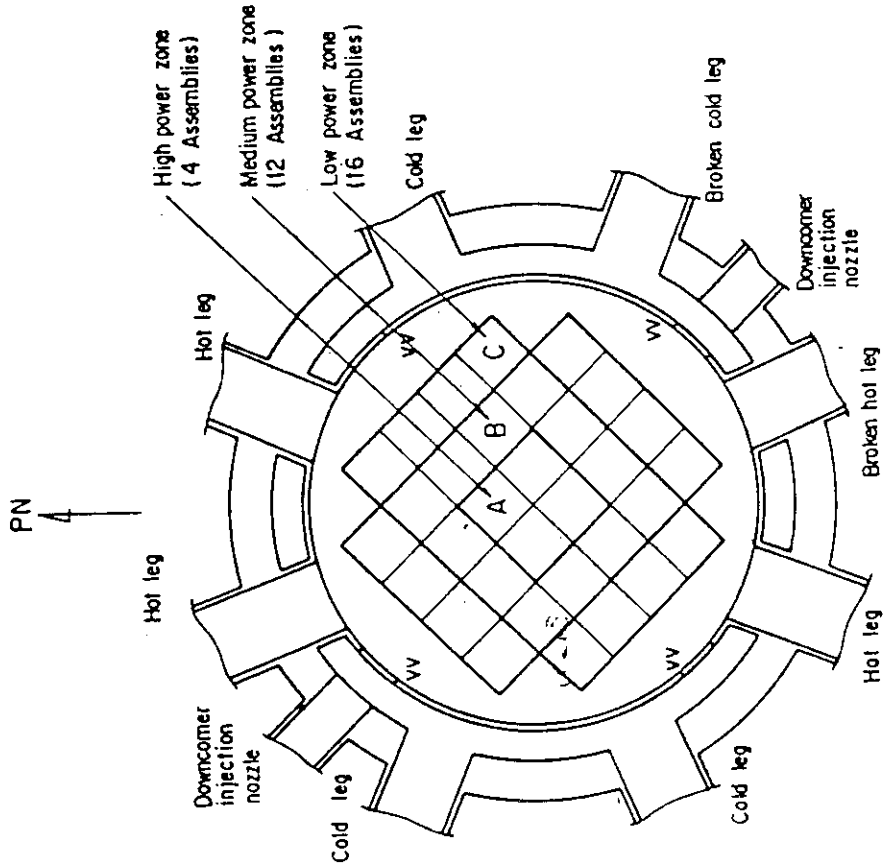

Fig. 2.4 Cross section of CCTF Core-II

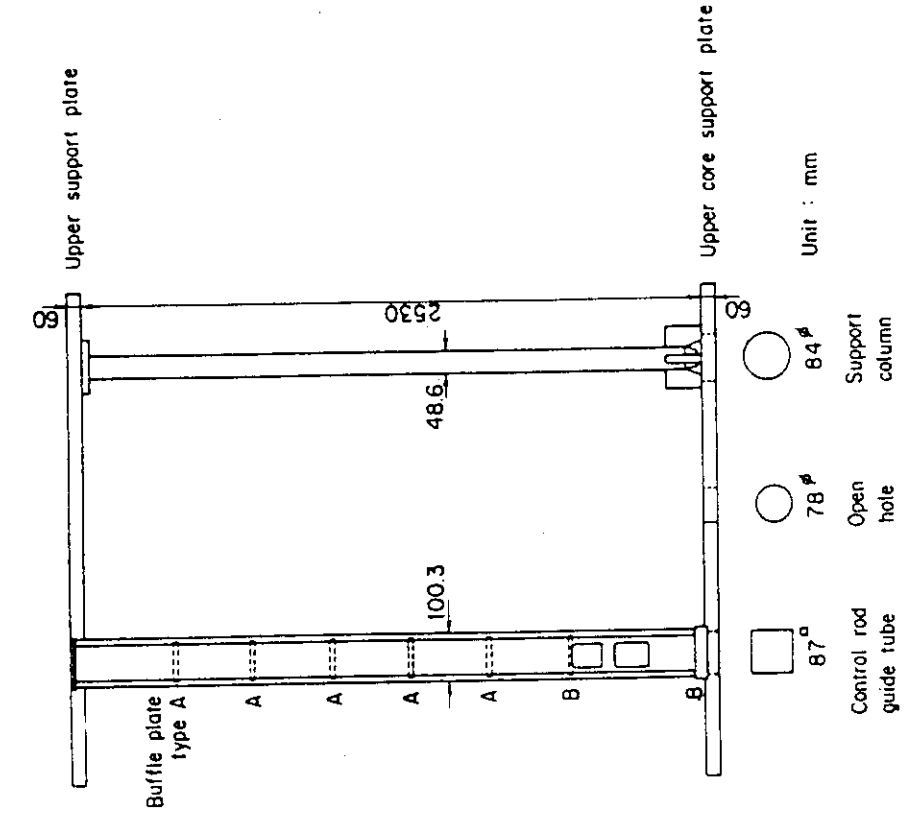

Fig. 2.7 Upper plenum internals

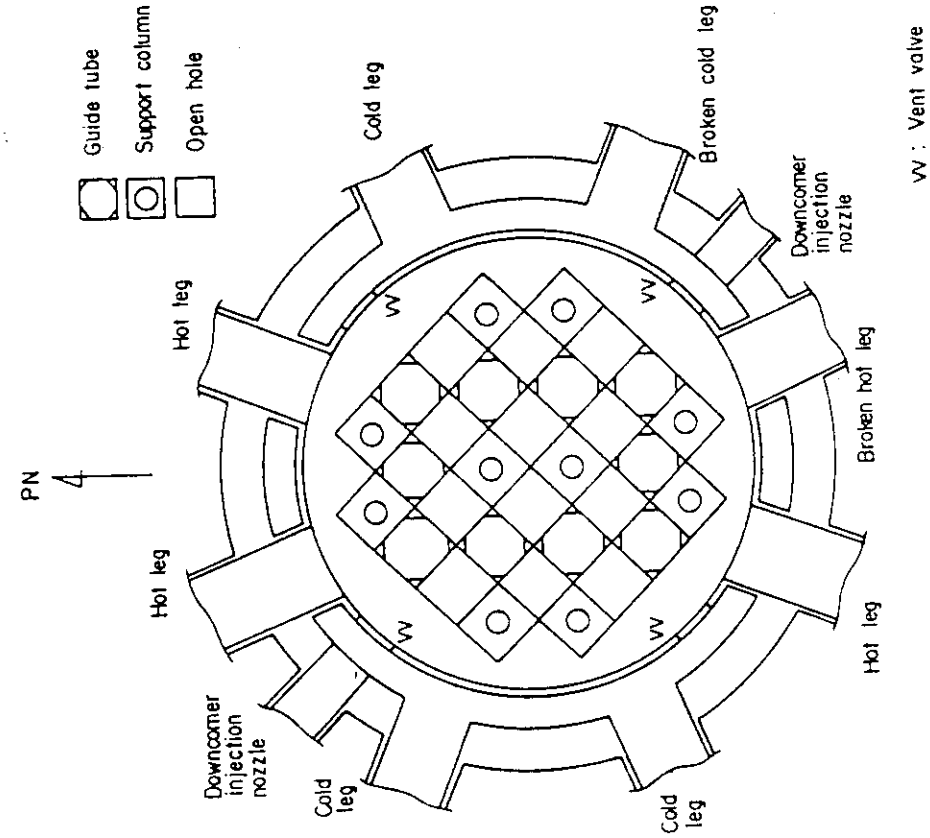

Fig. 2.6 Arrangement of upper plenum internals

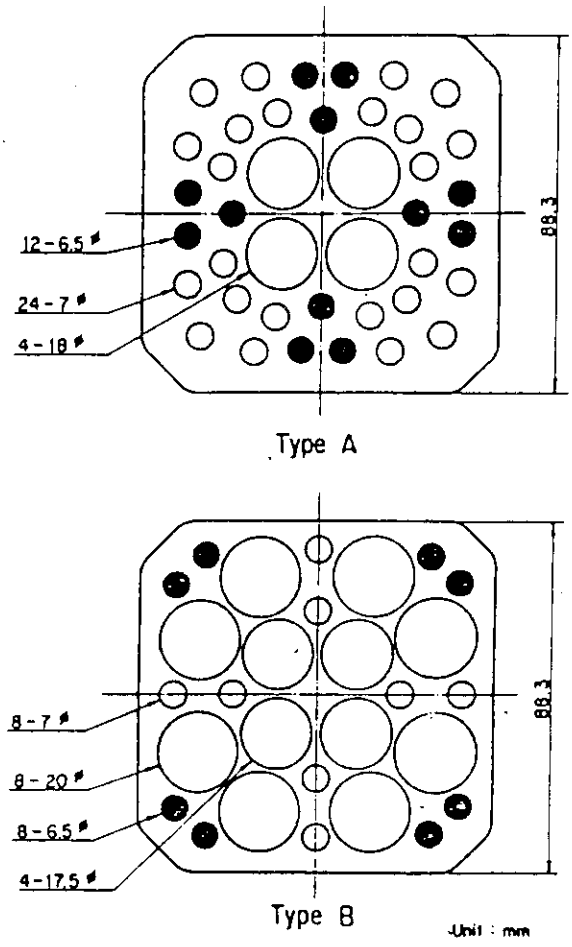

Fig. 2.8 Buffle plates in control rod guide tube

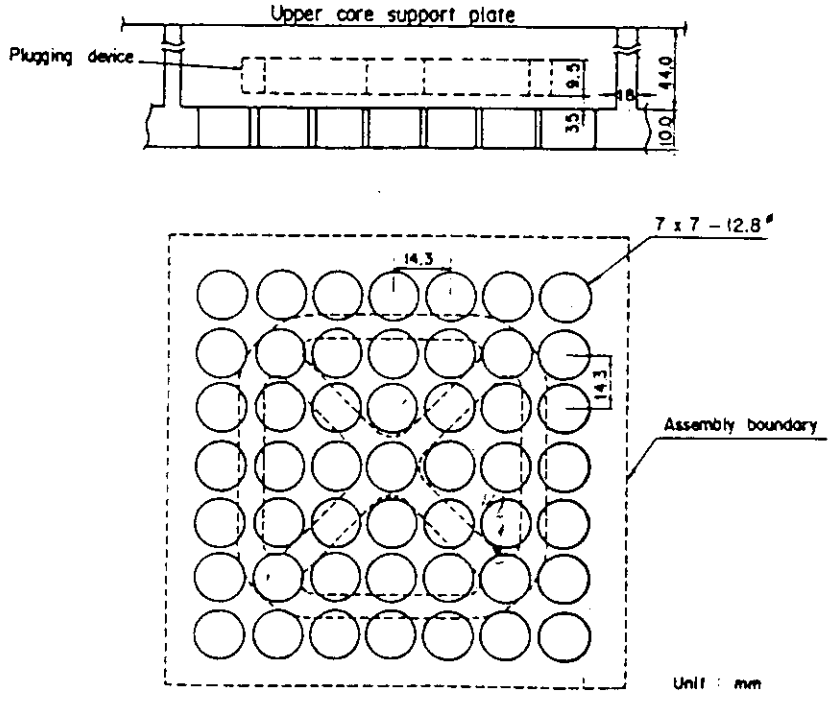

Fig. 2.9 Dimensions of holes of end box tie plate

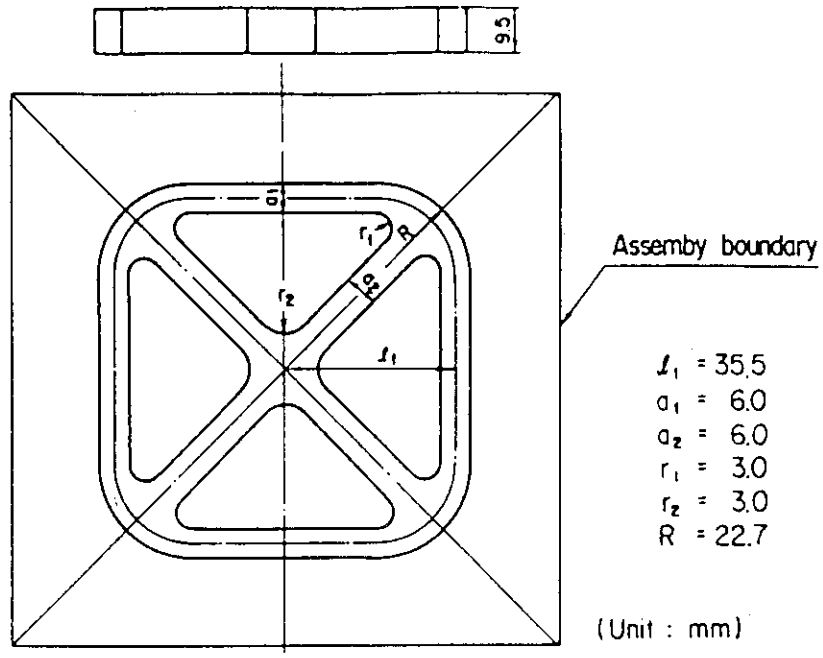

Fig. 2.10 Dimensions of plugging device

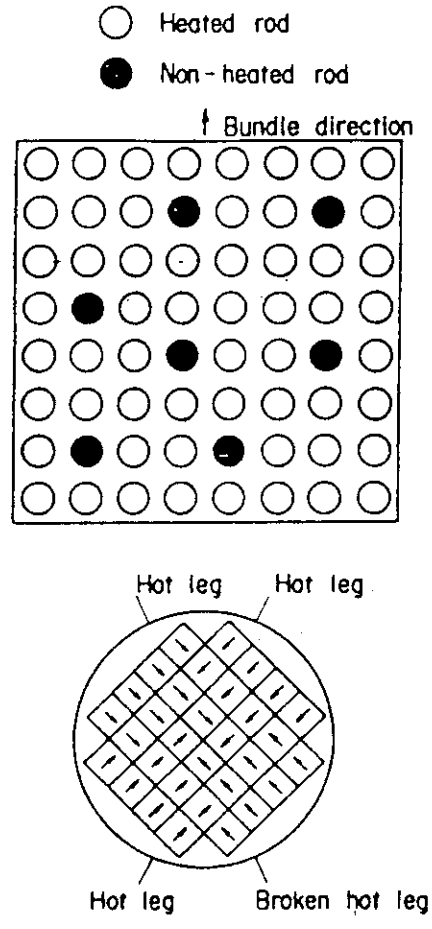

Fig. 2.11 Arrangement of non-heated rods bundle direction

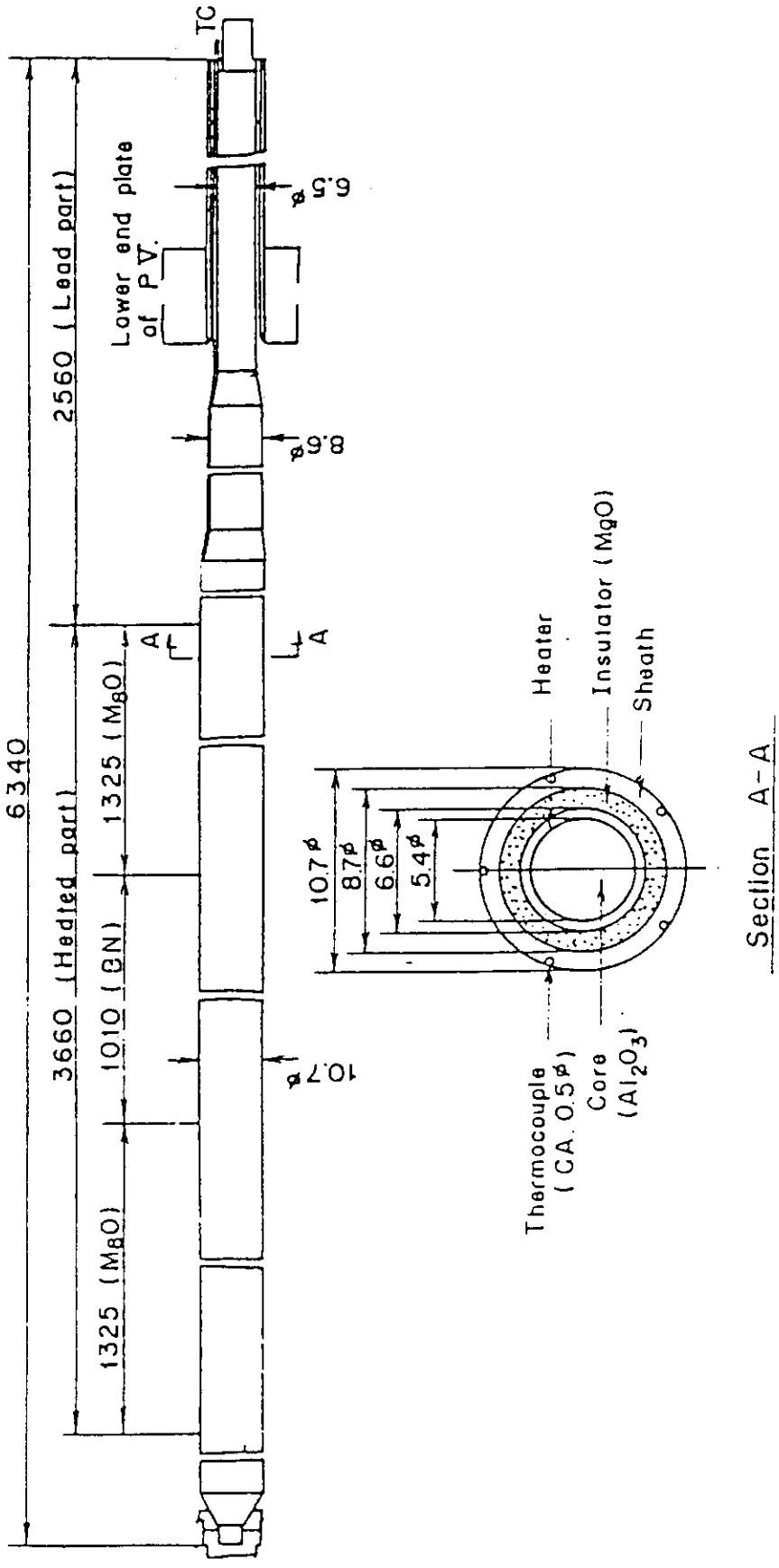

Fig. 2.12 Heater rod

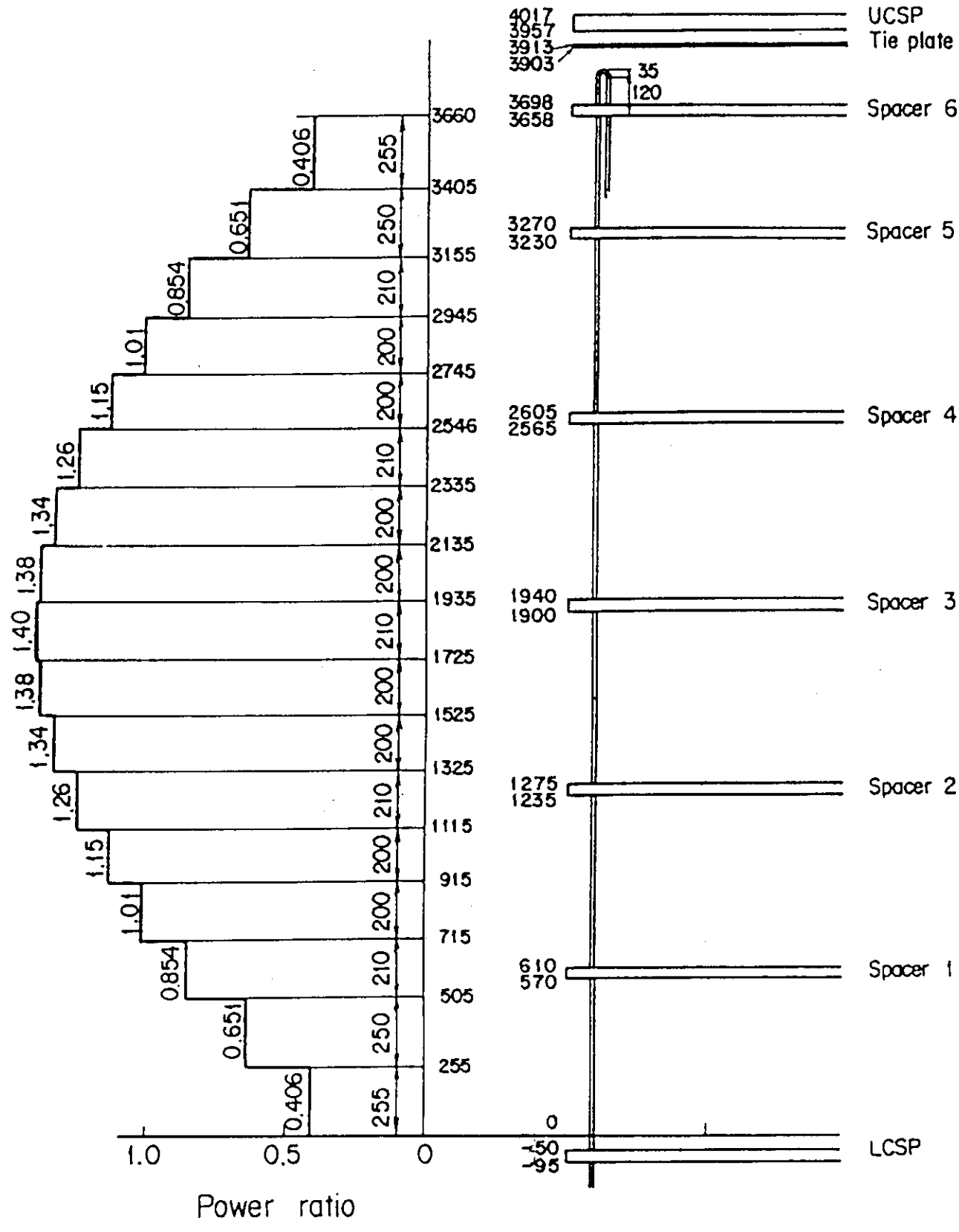

Fig. 2.13 Axial power profile of CCTF Core-II heater rod

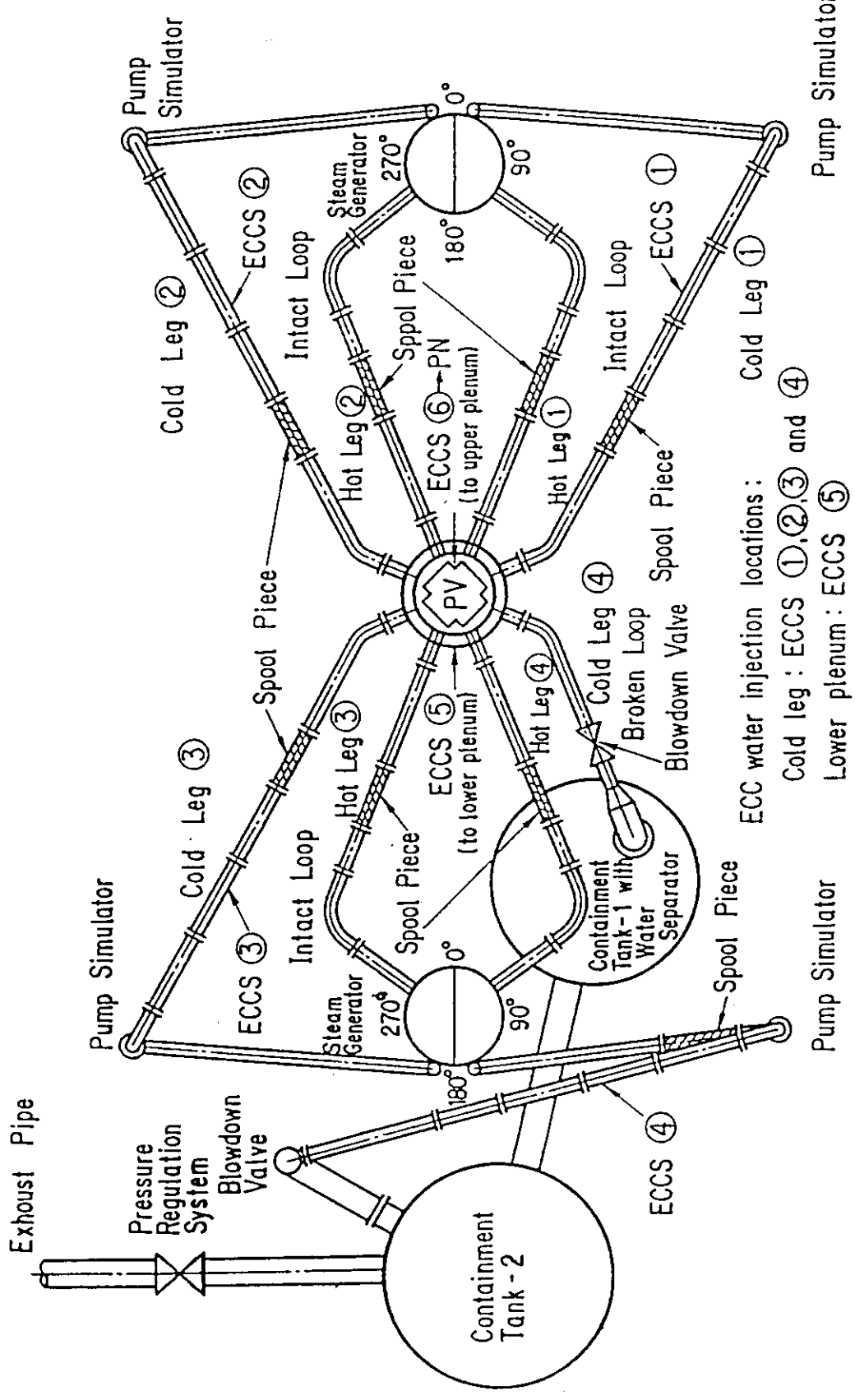

Fig. 2.14 Top view of primary loop pipings

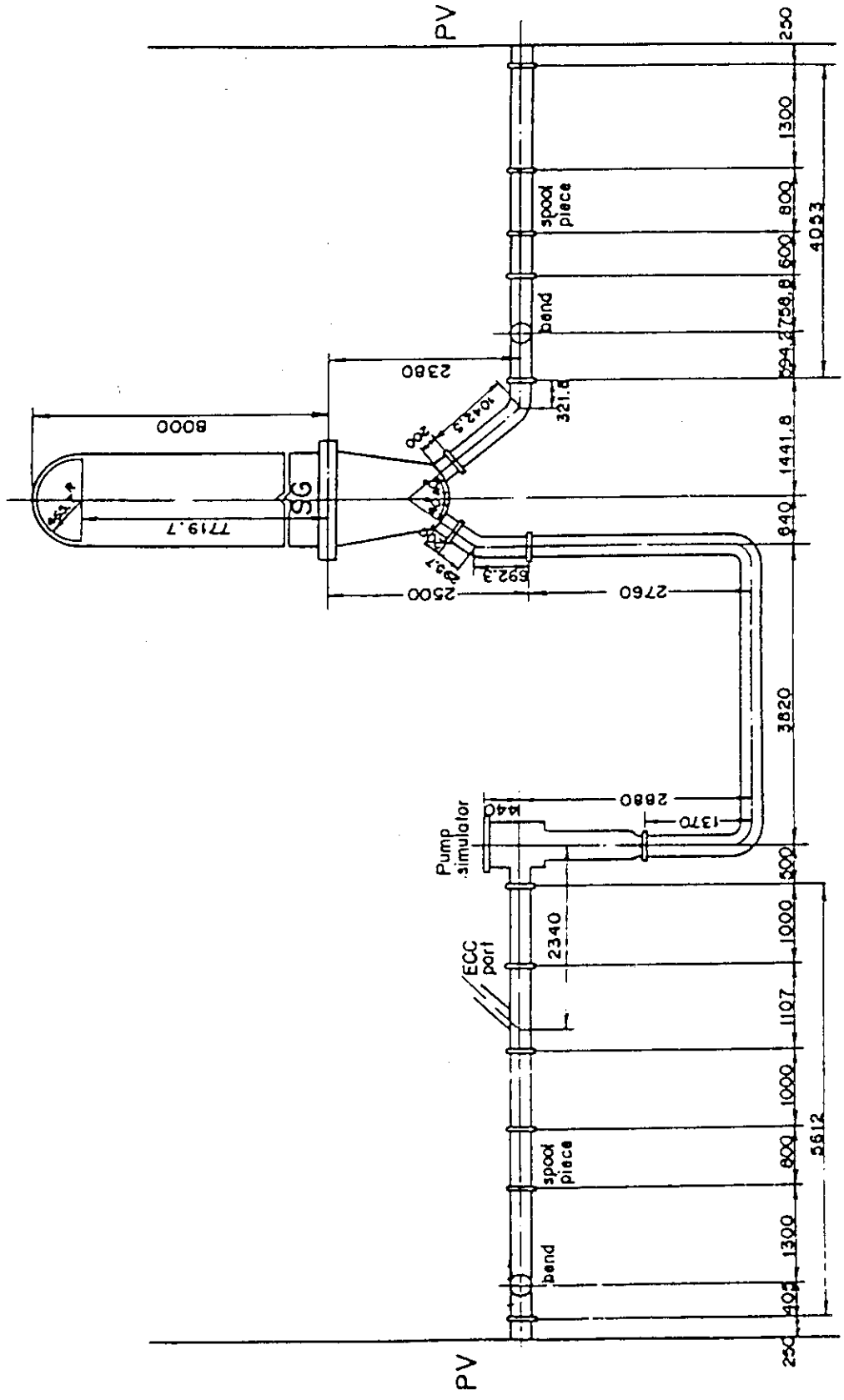

Fig. 2.15 Dimensions of primary loop

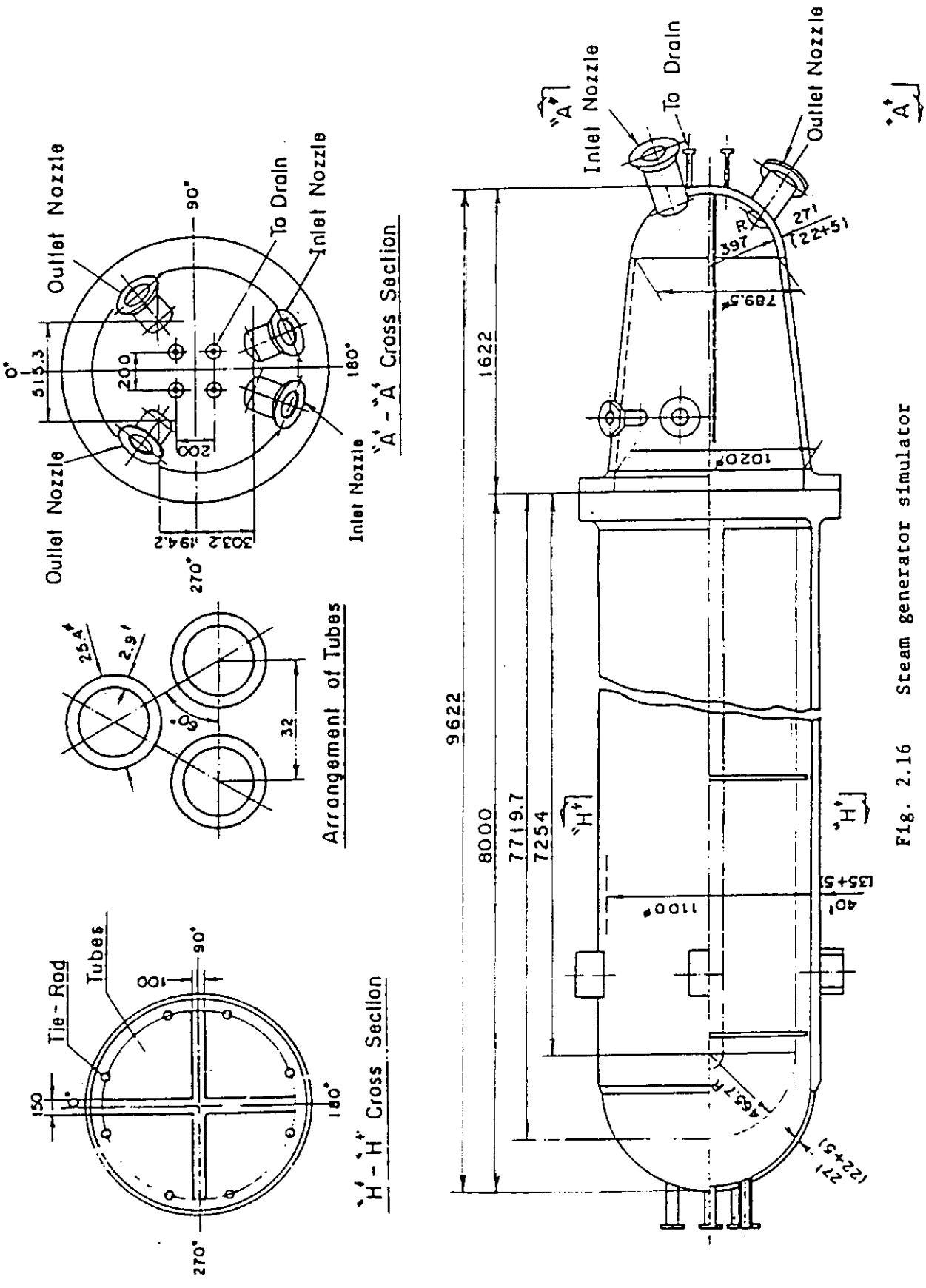

Fig. 2.16 Steam generator simulator

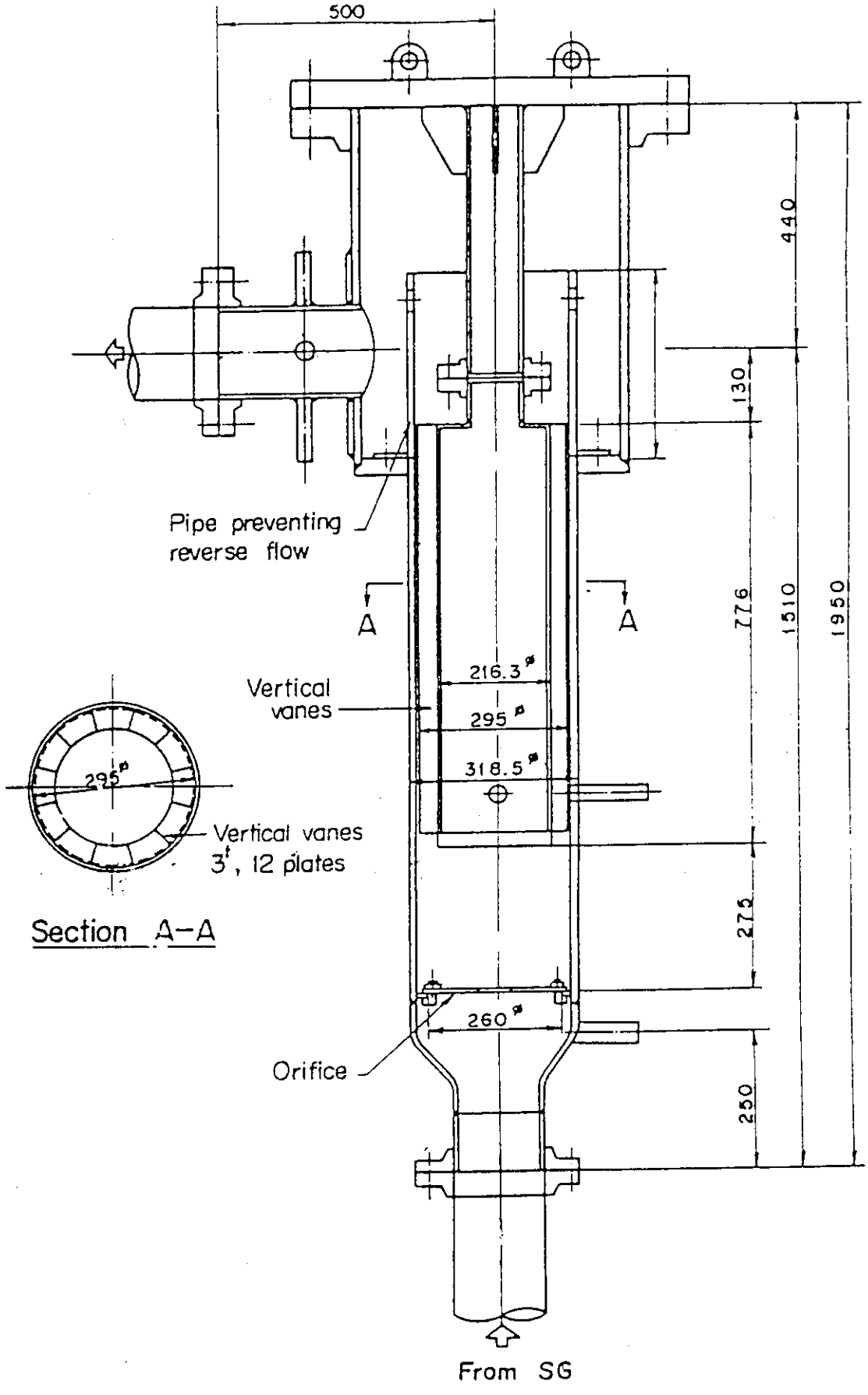

Fig. 2.17 Pump simulator

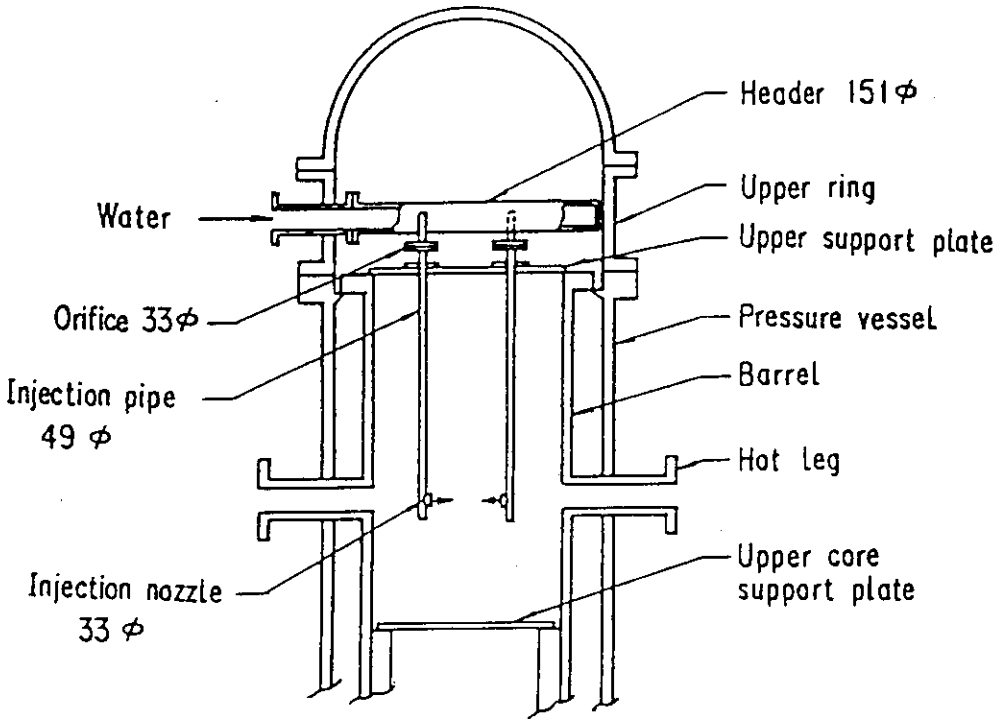

Fig. 2.18 Configuration of upper plenum injection pipe

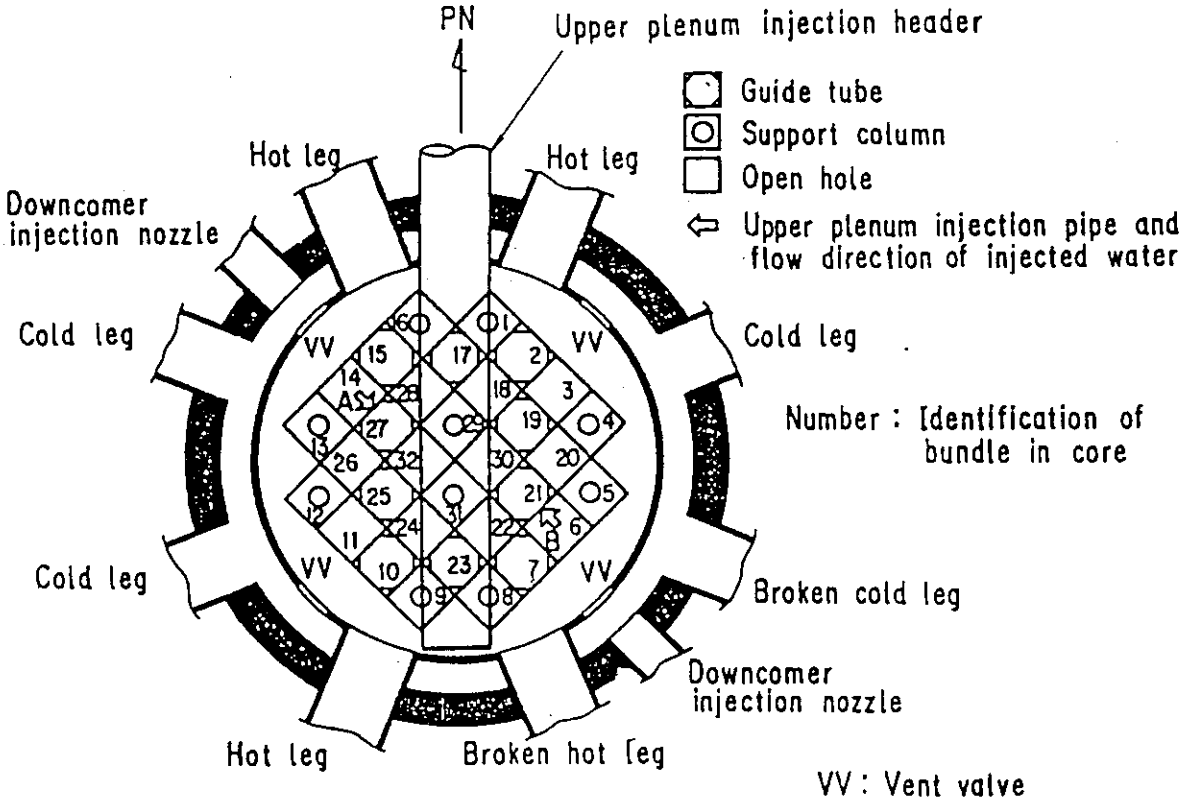

Fig. 2.19 Arrangement and location of upper plenum injection pipe

3. Measured test conditions and data presentation

3.1 Measured test conditions

When the low pressure test, or the CCTF test C2-8, was initiated(t= 0 s), the core was filled with the saturated steam at 0.15 MPa. The clad temperature of heater rods was about 383 K at t=0 s. The bottom of the pressure vessel was filled with saturated water to the level of 0.86 m from the bottom of the pressure vessel. The initial downcomer wall temperature was 461 K. The wall of the primary piping was preheated to the saturation temperature before the test initiation. The water level in the secondary side of the steam generator 1 and 2 were 7.30 and 7.50 m at the test initiation, respectively. The water temperature in the secondary side of the steam generator was about 540 K.

Figure 3.1 shows the transient of the total power supplied to heater rods in the core. At 0 s, the power is turned on. At 4 s,it reaches 9.32 MW. The average linear power of all heater rods in the core is 1.396 kW/m. The decay of the power starts at 95.0 s. The power follows the decay curve type of (ANSx1.2+Actinidex1.1(30 s after scram)).

Figure 3.2 shows the pressure in the containment tank 2. The initial pressure is 0.153 MPa as planned. Figure 3.2 shows that the pressure control was performed successfully in the CCTF test C2-8.

Figure 3.3 shows the transients of the ECC water injection rates into the lower plenum and the three intact cold legs. Figure 3.4 shows the transients of the fluid temperatures at ECC water injection nozzles. The maximum clad surface temperature reached the specified level(995 K) at 86.5 s and then the ECC water injection into the lower plenum was initiated. The injected water was accumulated in the lower plenum. At 96 s, the lower plenum was filled with water and the reflood of the heater rods started. At 98.5 s, the flow control valve in the lower plenum injection line began to close and the ECC water injection into lower plenum was terminated at 102.5 s. The flow control valves in the cold-leg accumulator injection line started openning at 98.5 s. The injection location of ECC water was switched from the lower plenum to the intact cold legs. The injection rate into cold legs increased with time and reached the setting rate(0.0910 m^3/s) at 103 s. The high injection rate simulates the accumulator injection in a PWR LOCA. At 110.0 s, the ECC water injection mode was switched to the LPCI mode. The ECC water injection from the accumulator tank was terminated at 114.0 s. The subcooled water(310 K) in the LPCI tank was pumped out to the intact

cold legs by 1010 s.

Table 3.1 summarizes the measured test conditions with the planned test ones. The chronology of events are summarized in Table 3.2.

3.2 Data presentation

The selected data from the CCTF test C2-8(Run 67) are presented in Figs. B-1 through B-27 in Appendix B. The Tag-ID of each measurement channel is shown in the upper part of each figure. Tag-IDs of each figure are listed in appendix A with short descriptions of the data processing.

3.3 Comparison of test conditions among the high pressure, base case and low pressure tests

Table 3.3 shows comparisons of test conditions among high pressure , base case, and low pressure tests. The test conditions of the base case test (Test C2-4) was determined based on the safety analysis for the actual PWRs with the evaluation model (EM) codes.[3] The core power was determined to simulate the decay curve type of (ANS x 1.2 + Actinide x 1.1 (30 s after scram)). The total power is scaled down by factor of 1/21.4 to simulate the power per unit volume of the core. The system pressure of the base case test (Test C2-4) was 0.20 MPa. In the high pressure (Test C2-1) and low pressure (Test C2-8) tests, the system pressure were 0.42 and 0.15 MPa, respectively. The initial superheat of the downcomer wall was adjusted to simulate the heat release from the wall to the unit volume of the downcomer.[3] The temperature of the primary piping wall was set at the saturation temperature of each system pressure. The saturation temperatures are 417, 393 and 383 K at 0.42, 0.20 and 0.15 MPa, respectively. The fluid temperature in the secondary side of the steam generator was set at 540 K in these three tests.

Table 3.4 shows the comparisons of the chronology of events in the CCTF Core-II system-pressure-effect tests. The time of 0 indicates the time of the reflood initiation in each test. The power decay was initiated at the same time of the reflood initiation. The accumulator injection location was switched at about 3.0 s from lower plenum to cold legs. The ECC injection mode was switched at about 17 s from the Acc mode to the LPCI mode. All heater rods in the core were quenched at 326.5, 558.0 and 666.0 s in the high-pressure, the base-case and the low-pressure tests, respectively.

Table 3.1 Initial conditions for low pressure test

	Planned	Measured
Power		
Total (MW) :	9.345	9.32
Linear (kW/m) :	1.400	1.396
Radial power distribution(kW/m) :	1.910:1.674:1.067	1.901:1.674:1.067
Decay type : ANSx1.2 + Actinidex1.1 (30 s after scram)		
Pressure		
System (MPa) :	0.15	0.15
Steam generator secondary (MPa) :	5.20	5.18
Temperature		
Downcomer wall (K) :	461	461
Primary piping wall (K) :	383	387
Steam generator secondary (K) :	540	540
Peak clad at ECC initiation (K) :	995	995
Peak clad at reflood initiation (K) :	1073	1073
Lower plenum liquid (K) :	383	386
ECC liquid (K) :	308	310
Water level		
Lower plenum (m)	0.90	0.86
Steam generator secondary (m) :	7.40	7.40
ECC water injection rate		
Accumulator to lower plenum (m^3/s) :	0.1050	0.105
Accumulator to cold legs (m^3/s) :	0.0892	0.091
LPCI to cold legs (m^3/s) :	0.0111	0.0113

Table 3.2 Chronology of events for low pressure test

Event	Time (s)
Test initiated (Heater power on) (Data recording initiated)	0.0
Accumulator injection to lower plenum initiated	86.5
Power decay initiated	95.0
Bottom of core recovery(BOCREC) (Reflood initiated)	96.0
Accumulator injection to cold legs initiated	98.5
Accumulator injection to lower plenum ended	102.5
LPCI injection to cold legs initiated	110.0
Accumulator injection to cold legs ended	114.0
All heater rods quenched	760.0
Power off	1010.0
LPCI injection to cold legs ended	1010.0
Test ended (Data recording ended)	1040.0

Table 3.3 Comparison of test conditions among CCTF Core-II system pressure effect tests C2-1, C2-4 and C2-8

Item	Test C2-1	Test C2-4	Test C2-8
Core power			
Total(MW)	9.35	9.37	9.32
Core-averaged linear power(kW/m)	1.40	1.40	1.40
Radial power profile	1.90:1.68:1.06	1.90:1.67:1.07	1.90:1.67:1.07
System pressure			
Containment(MPa)	0.42	0.20	0.15
Temperature			
Initial superheat of downcomer wall (K)	74	74	78
Primary piping wall (initial) (K)	425	394	387
Fluid in secondary side of steam generator(K)	538	539	540
Peak clad at reflood initiation (K)	1073	1072	1073
ECC water temperature(K)	309	308	310
ECC water injection rate			
Acc into cold legs(m^3/s)	0.089	0.091	0.091
LPCI into cold legs(m^3/s)	0.011	0.011	0.011

Table 3.4 Chronology of events for system pressure effect tests

Event	Time (s)		
	Test C2-1	Test C2-4	Test C2-8
Test initiated (Heater power on) (Data recording initiated)	-90.5	-94.0	-96.0
Accumulator injection to lower plenum initiated	-9.5	-9.5	-9.5
Power decay initiated	0.0	-0.5	-1.0
Bottom of core recovery(BOCREC) (Reflood initiated)	0.0	0.0	0.0
Accumulator injection to switched from lower plenum to cold legs	4.5	3.0	2.5
LPCI injection to cold legs initiated	17.0	18.0	16.0
All heater rods quenched	326.5	558.0	666.0
Power off	617.5	911.0	914.0
LPCI injection to cold legs ended	737.5	911.0	914.0
Test ended (Data recording ended)	938.5	941.0	944.0

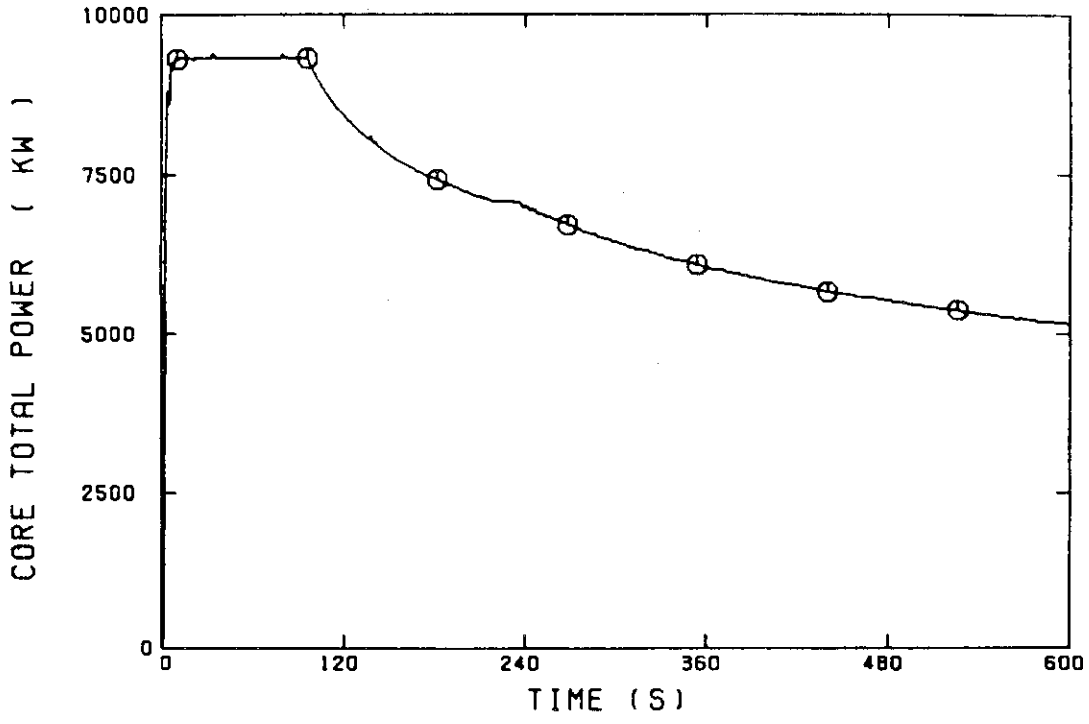

Fig. 3.1 Total power supplied to heater rods in core in CCTF test C2-8

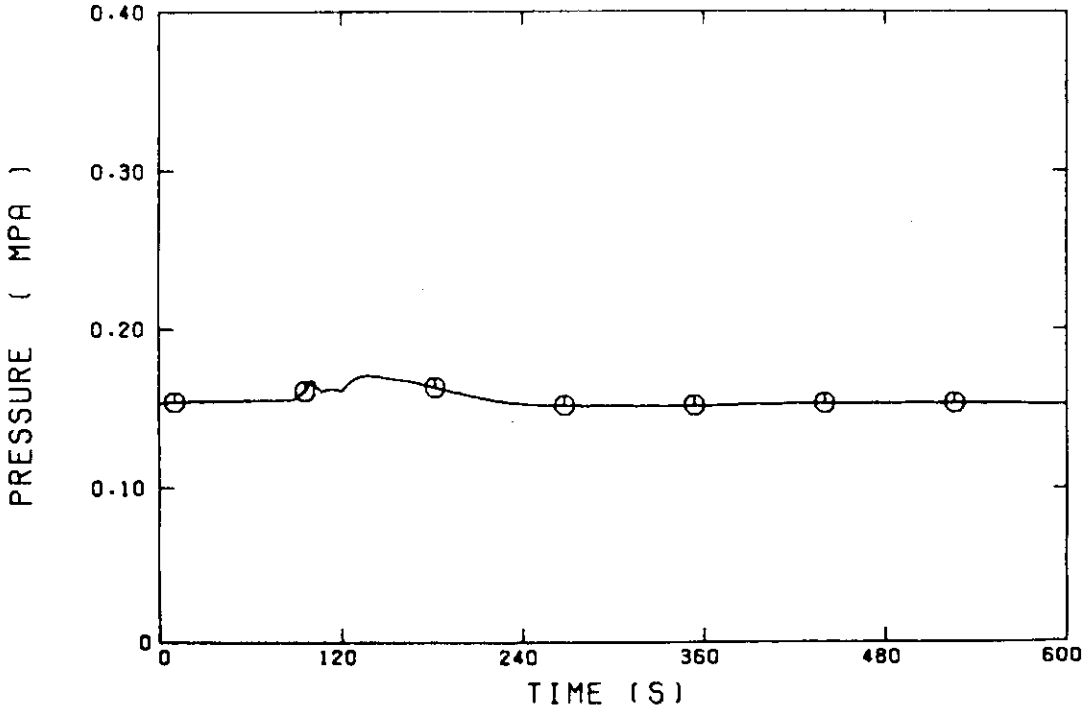

Fig. 3.2 Pressure in containment tank 2 in CCTF test C2-8

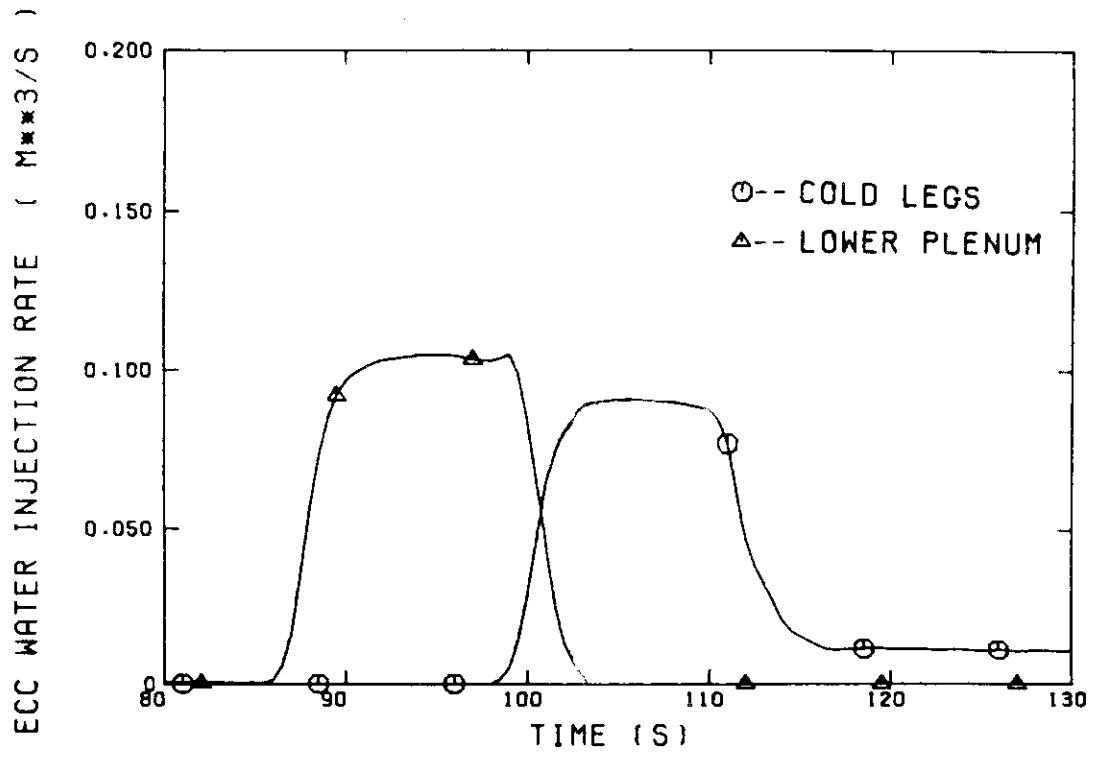

Fig. 3.3 ECC water injection rates into lower plenum and three intact cold legs in CCTF test C2-8

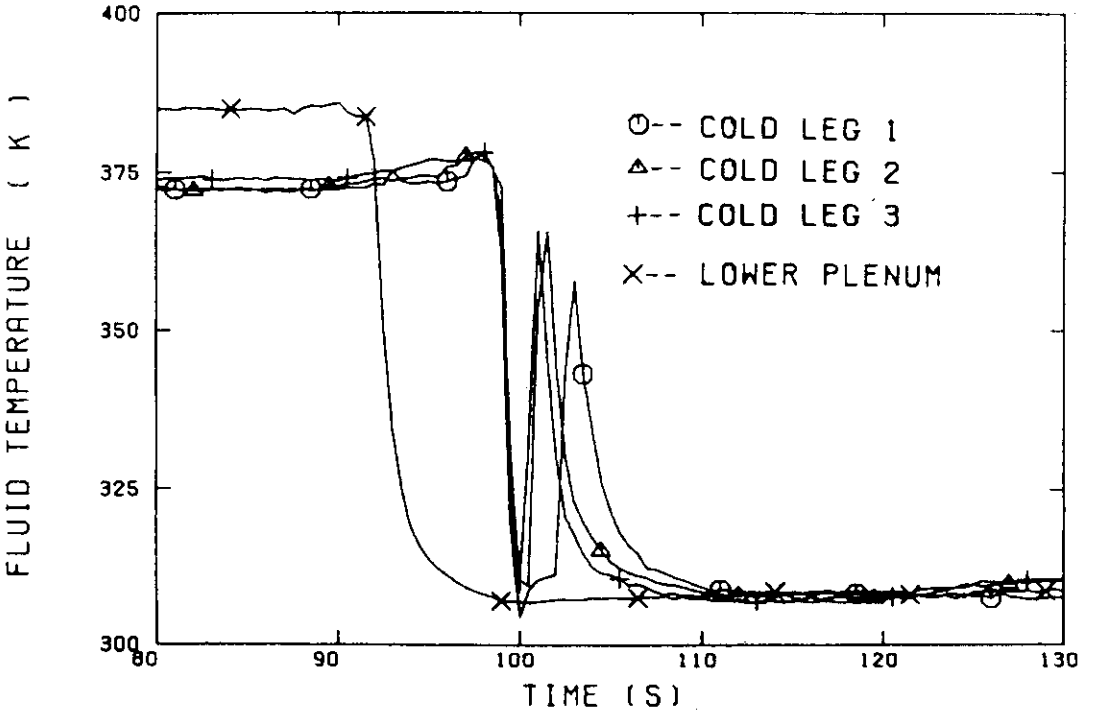

Fig. 3.4 Fluid temperatures at ECC water injection nozzles in CCTF test C2-8

4. Results and discussion

4.1 System pressure effect on system behavior

Figure 4.1 shows the comparisons of the downcomer water head among the high pressure test (system pressure 0.42 MPa, Test C2-1), the base case test (system pressure 0.20 MPa, Test C2-4) and the low pressure test (system pressure 0.15 MPa, Test C2-8). The water head was measured through the vertical section between the bottom of the pressure vessel and the elevation of 8.183 m from the bottom of the pressure vessel. The cold leg nozzles are connected to the downcomer at the elevation of 7.0 m from the bottom of the pressure vessel.

The water head increases quickly due to the high ECC water injection rate into the lower plenum and/or the cold legs. The water head reaches the maximum at about 20 s. The densities of the saturated water are 921, 943 and 950 kg/m^3 at the pressure of 0.42, 0.20 and 0.15 MPa, respectively. If the downcomer is filled with the saturated water to the level of the cold leg nozzle, the static water heads in the downcomer are equal to 63.2, 64.7 and 65.2 kPa at 0.42, 0.20 and 0.15 MPa, respectively. These water heads are almost the same as the observed maximum water heads in these tests. It is considered that the spill-over of the downcomer fluid was initiated at about 20 s.

The ECC injection mode was switched from the Acc mode to the LPCI mode at about 17 s as shown in Table 3.4. After about 20 s the downcomer water head decreases with time. The minimum downcomer water heads of 51.8, 55.0 and 55.7 kPa are observed at 142, 174 and 220 s in the high pressure (0.42 MPa), the base case (0.20 MPa), the low pressure (0.15 MPa) tests, respectively. The test result shows that the higher system pressure results in the lower downcomer water head during the LPCI mode. This is consistent with the observed result in the CCTF Core-I tests.[4]

Figure 4.2 shows the comparisons of the core water head. At the end of the Acc mode (about 17 s), the core water head is about 10 kPa and then it increases gradually with time during the LPCI mode. The whole core quench times are 326.5, 558.0 and 666.0 s in the high pressure (0.42 MPa), the base case (0.20 MPa), the low pressure (0.15 MPa) tests, respectively. The core water head increases with the system pressure, in other words, more water is accumulated in the core at higher system pressure.

Figure 4.3 shows the differential pressure through the end box region. The end box region is defined as the section between the top of

the core heated part (5.76 m from the bottom of the pressure vessel) and the top surface of the upper core support plate (6.117 m from the bottom of the pressure vessel). The differential pressure begins to increase at the reflood initiation and it shows the constant differential pressure of about 0.9 kPa after 100 s. The differential pressure corresponds to the average void fraction of 73 % with the assumption of the negligible friction and acceleration pressure losses.

Figure 4.4 shows the system pressure effect on the differential pressure above the upper core support plate. The higher system pressure results in the higher differential pressure. In the high pressure test (0.42MPa), the differential pressure is nearly constant at 3.4 kPa after 350 s. In the CCTF, the hot leg nozzle is located at the section between 6.95 and 7.10 m from the bottom of the pressure vessel. Assuming that the upper plenum is filled with the homogeneous two-phase mixture between the upper core support plate and the hot leg nozzle, the differential pressure corresponds to the void fraction of 56 % in the upper plenum.

Figures 4.5 and 4.6 show the comparisons of the mass flow rate and the differential pressure through the intact loop. The mass flow rate was evaluated using the differential pressure through the pump orifice plate, assuming that the flow resistance coefficient is 15. The differential pressure through the intact loop decreases with the system pressure. On the other hand, the mass flow rate through the intact loop increased with the system pressure. System pressure effect on the mass flow rate and the differential pressure is similar for the broken loop as shown in Figs. 4.7 and 4.8. These results suggest that the steam binding effect decreases with the system pressure.

Figures 4.9 and 4.10 show the comparisons of the flow resistance coefficients of the intact and broken loops, respectively. The flow resistance coefficient K was defined by

$$K = \frac{\Delta P}{\frac{1}{2}\rho U^2} \quad , \tag{1}$$

where ΔP : Differential pressure through a loop (Pa),

ρ : Steam density in the upper plenum (kg/m^3),

U : Velocity ($= m/\rho A$) (m/s),

m : Mass flow rate through a loop (kg/s),

A : Flow area of a loop ($= 0.01892$) (m^2).

Before the entire quench of the heater rods, the flow resistance coefficients are nearly constant with time. It is insensitive to the system pressure. The result confirms that weaker steam binding effect at higher system pressure is attributed to higher steam density.

In the high pressure (0.42 MPa) test, the flow resistance coefficient starts to increase at about 300 s. It was found by the check of the sectional differential pressure measurements along the loop that the increase of the flow resistance coefficient is caused by the increase of the water accumulation in the vertical part of the hot leg piping and the inlet plenum of the steam generator. In the test, the differential pressure above the upper core support plate was constant with time after 350 s as shown in Fig. 4.4. It is guessed that the mixture level in the upper plenum reached the level of the hot leg nozzle at about 350 s in the high pressure (0.42 MPa) test. The approach of the mixture level to the level of the hot leg nozzle seems to lead the increase of the entrained water from the upper plenum to the hot legs and cause the increase of the water accumulation in the vertical part of the hot leg piping and the inlet plenum of the steam generator.

Figure 4.11 shows the system pressure effect on the steam and water mass flow rates and the differential pressure through the broken cold leg. In these tests, the ECC injection mode was switched at about 17 s from the Acc to the LPCI modes. During the Acc mode, the differential pressure through the broken cold leg is low. The differential pressure starts to increase at 19 s in the base case test (0.20 MPa) and it reaches the maximum of 50.6 kPa at 87 s.

The water mass flow rate was evaluated by the differentiation of the water level data in the containment tank 1. In the differentiation, the data was smoothed using the data for 20 s with the moving average method in order to suppress high frequency components of the data. The water level in the containment tank 1 began to increase at about 22 s. The time was almost equal to the time when the mixture level in the downcomer was estimated to reach the bottom of the broken cold leg nozzle. It is considered that the increase in the water mass flow rate around 22 s is caused by the initiation of the spill-over of the fluid in the downcomer. The reduction of the water mass flow rate at about 25 s is attributed to the switch of the ECC injection mode from the Acc mode to the LPCI mode because the water flow rate from the intact cold legs to the downcomer is reduced to only about one ninth.

The steam mass flow rate fluctuates with time during the Acc mode. In the base case (0.20 MPa) test, the steam mass flow rate begins to increase at 21 s and reaches the maximum at 81 s. The superficial steam velocity with the flow area of the broken cold leg (= 0.01892 m^2) is 85 m/s at 81 s. In the period between 40 and 500 s, the superficial steam velocities vary between 11 and 45, 55 and 85, 65 and 106 m/s in the high pressure (0.42 MPa), the base case (0.20MPa) and the low pressure (0.20

MPa), reapectively.

The test results show that the higher system pressure results in the lower superficial steam velocity and the lower differential pressure through the broken cold leg.

Figures 4.12 and 4.13 show the system pressure effect on the core inlet mass flow rate and the core inlet mass flow. The core inlet mass flow rate was estimated using the mass balance in the pressure vessel.[3] The error of the mass flow rate was estimated to be 15%. The core inlet mass flow indicates the integration of the core inlet mass flow rate. It means the total mass flow through the core inlet after the reflood initiation. During the Acc mode (before 17 s), the core inlet mass flow rate is high due to the high ECC water injection rate. In the period, the core inlet mass flow rate is almost the same regardless of the system pressure. After the switch of the ECC injection mode from the Acc mode to the LPCI mode, the core inlet mass flow rate decreases with time in these tests. The time averaged core inlet mass flow rates between 20 and 100 s are 7.11, 5.49 and 5.01 kg/s in the high pressure (0.42 MPa), the base case (0.20 MPa) and the low pressure (0.15 MPa) tests, respectively. The core inlet mass flow rate increases with the system pressure in the period just after the switch of the ECC injection mode. Even after 100 s, the same system pressure effect on the core inlet mass flow rate can be observed. The time averaged core inlet mass flow rates between 100 and 500 s are 4.97, 4.48 and 4.22 kg/s in the high pressure (0.42 MPa), the base case (0.20 MPa) and the low pressure (0.15 MPa) tests, respectively.

Figure 4.14 shows the comparisons of the core inlet pressure. After the reflood initiation, the core inlet pressure increases with time due to the increase in the downcomer water head and the differential pressure through the broken cold leg. The maximum pressure of 0.492, 0.303 and 0.262 MPa are recorded at 50, 67 and 80 s in the high pressure (0.42 MPa), the base case (0.20 MPa) and the low pressure (0.15 MPa) tests, respectively. The core inlet pressure vary between 0.46 and 0.492, 0.268 and 0.303, and, 0.227 and 0.262 MPa in the high pressure (0.42 MPa), the base case (0.20 MPa) and the low pressure (0.15 MPa) tests, respectively. The discrepancy between the containment pressure and the core inlet pressure decreases with the system pressure. This is attriduted to the decrease in the differential pressure through the broken cold leg.

Figure 4.15 show the comparison of the core inlet subcooling of the fluid. The subcooling increases with time by about 80 s. The subcoolings are 24.9, 31.2, and 32.3 K at 80 s in the high pressure (0.42 MPa), the base case (0.20 MPa) and the low pressure (0.15 MPa) tests, respectively. The test result shows that the core inlet subcooling decreases slightly

with the system pressure. After 100 s, the subcooling of the fluid decreases gradually with time and it approaches to saturation temperature in these tests.

4.2 System pressure effect on core thermal behavior

Figure 4.16 shows an example of the clad surface temperature at the midplane (1.83 m from the bottom of the core heated part) of a heater rod in the central region (30 bundle). The clad surface temperature increases gradually after the reflood initiation. The maximum temperature in each temperature history is called the turnaround temperature. The temperature rise is defined as the difference between the turnaround and the initial clad surface temperatures. The time to the maximum temperature recording is called the turnaround time.

Figures 4.17 and 4.18 show the system pressure effect on the temperature rise and the turnaround time, respectively. Below 1.425 m from the bottom of the core heated part, the turnaround was recorded before the switch of the ECC water injection mode from the Acc to the LPCI modes. In the region, the temperature rise and the turnaround time are insensitive to the system pressure. At the elevation of 2.035 m, the turnaround time is shorter than that at the elevation of 1.83 m. The grid spacer is located at 1.940 m in the CCTF Core-II. The faster turnaround and the lower temperature rise may be attributed to the grid spacer effect.[9] Above 1.83 m (except 2.035 m), the system pressure effect is significant as shown in Figs. 4.17 and 4.18. The higher system pressure resulted in the shorter turnaround time and the lower temperature rise.

Figures 4.19 and 4.20 show the system pressure effect on the quench temperature and time, respectively. The higher system pressure resulted in the higher quench temperature and the faster quench at the same elevation. Even though grid spacer effect is significant in the quench temperature, it is not obvious in the quench time at the elevation of 2.035 m.

Figure 4.21 shows the comparisons of the heat transfer coefficients at the midplane of the heater rod in the peripheral region between the experimental and estimated results. For the estimation of the heat transfer coefficients, the correlation developed by Murao and Sugimoto[8] was applied. The correlation is given by

$$h = h_f + h_r \ , \qquad (2)$$

where

$$h_f = 0.94 \left(\frac{k_g^3 \rho_g \rho_\ell h_{fg} g}{L_q \cdot \mu_g \cdot \Delta T_{sat}} \right)^{\frac{1}{4}} (1-f_g)^{\frac{1}{4}} , \quad (3)$$

$$h_r = E\varepsilon (1-f_g)^{\frac{1}{2}} (T_w^4 - T_{sat}^4) / \Delta T_{sat} . \quad (4)$$

h : heat transfer coefficient (W/m^2K),
k : thermal conductivity (W/mK),
ρ : density (kg/m^3),
h_{fg} : latent heat for evaporation (J/kg),
f_g : void fraction,
g : acceleration of gravity (m/s^2) or suffix for gas phase,
l : suffix for liquid phase,
L_q : distance from quench front (m),
μ_g : viscosity (Pas),
T_{sat} : wall superheat (K),
E : Stefan Boltzman constant (W/m^2K^4),
e : emmisivity,
T_w : wall temperature (K),
T_{sat} : saturation temperature (K).

The first and second terms of Eq. (2) indicate the heat transfer due to the film boiling and the radiation, respectively.

In the estimation, the measured clad surface temperature, fluid temperature, and the pressure in the core were used to evaluate the wall superheat and the physical properties of steam and water. The quench data were also used to calculate the distance from the quench front in each region. The void fraction at the elevation of 1.83 m was estimated from the differential pressure measurement through the section between 1.22 and 2.44 m. The estimated results show higher total heat transfer coefficient h at higher system pressure as observed in the experiment.

The estimation shows that the heat transfer coefficient due to the radiation is insensitive to the system pressure as shown in Fig. 4. 21. On the other hand, the film boiling term increases with the system pressure. The estimation shows that the increase of the heat transfer with the system pressure is caused by the increase in the film boiling heat transfer.

Equation (2) indicates that the heat transfer coefficient due to film boiling is affected by the local void fraction, the distance from the quench front and the physical properties of steam and water. Table 4.1 shows the system pressure effect on the heat transfer coefficient through the effect of the physical properties of steam and water. In the evaluation for Table 4.1, void fraction f_g, distance from the quench front L_q, and clad surface temperature T_w were assumed to be 0.9, 1.0 m and 1000 K, respectively. The estimated total heat transfer coefficients h are 68.7, 73.4 and 86.7 W/m^2K at 0.15, 0.20 and 0.42 MPa, respectively. The estimated heat transfer coefficient at 0.42 MPa is higher by 26 % than that at 0.15 MPa. The estimation confirms that the heat transfer coefficient in the core is increased with the system pressure when both of the void fraction and the distance from the quench front are identical. Table 4.1 shows that the increase of the heat transfer coefficient with the system pressure is attributed mainly to the increase of the steam density.

Figures 4.22 and 4.23 show the comparisons of the void fraction at the elevation of 1.83 m, and the distance from the quench front at the elevation of 1.83 m, respectively. In the early period of the test (by about 20 s), both the void fraction and the distance from the quench front are almost the same. As shown in Table 4.1, the higher system pressure results in the higher heat transfer coefficient because of higher steam density in the early period of the test.

The higher heat transfer coefficient leads to the faster propagation of the quench front in the successive period. After 60 s, the void fraction becomes lower and the distance from the quench front becomes shorter at the higher system pressure. According to Eq. (2), both of the lower void fraction and the shorter distance from the quench front give the higher heat transfer coefficient. Figures 4.22 and 4.23 prove that the higher system pressure enhances core heat transfer not only by the effect of the steam density but also by the effect of the local void fraction and the distance from the quench front after 60 s.

Table 4.1 System pressure effect on heat transfer coefficient through the effect of physical properties of steam and water

System pressure(MPa) / Item	0.15	0.20	0.42
Thermal conductivity of steam k_g (W/mK)	0.0569	0.0575	0.0590
Density of steam ρ_g (kg/m^3)	0.476	0.637	1.336
Density of water ρ_l (kg/m^3)	951	944	923
Latent heat of evaporation (J/kg)	2.29×10^6	2.20×10^6	2.13×10^6
Viscosity of steam μ_g	2.52×10^{-5}	2.54×10^{-5}	2.59×10^{-5}
Wall superheat (K)	617	607	582
Heat transfer coefficient due to film boiling h_f (W/m^2K)	55.0	59.5	72.3
Heat transfer coefficient due to radiation h_r (W/m^2K)	13.7	13.9	14.4
Total heat transfer coefficinet($=h_f+h_r$) (W/m^2K)	68.7	73.4	86.7

Notes:Assumptions in the estimation

Void fraction=0.90

Distance from the quench front=1.0 m

Clad surface temperature = 1000 K

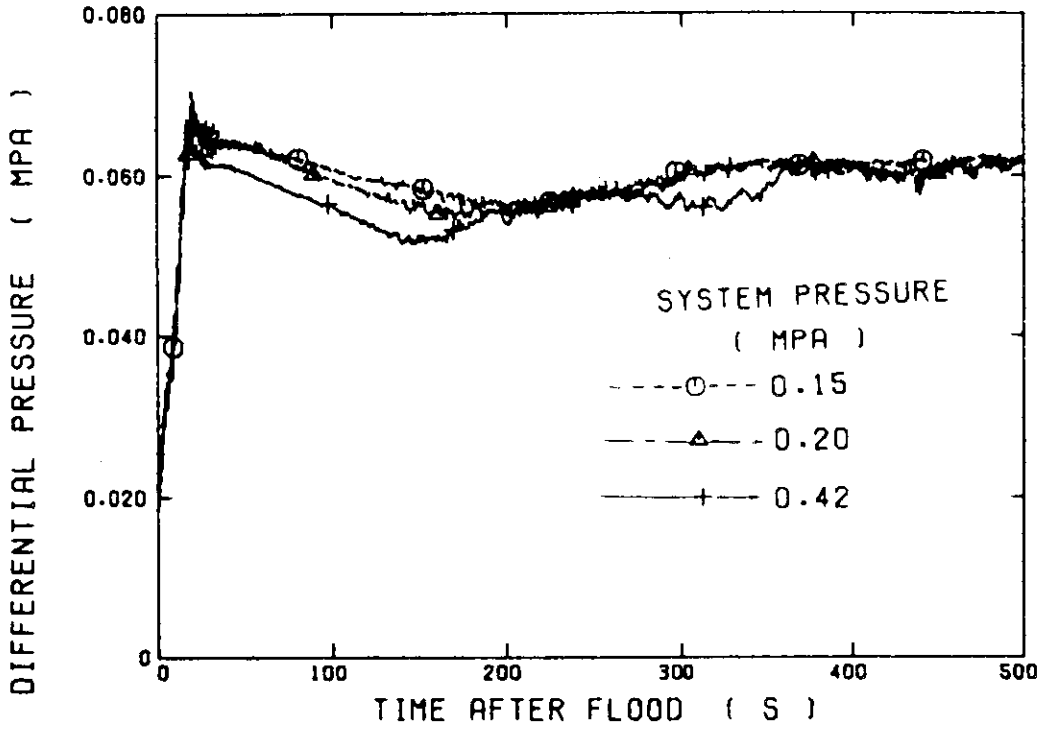

Fig. 4.1 System pressure effect on the downcomer water head

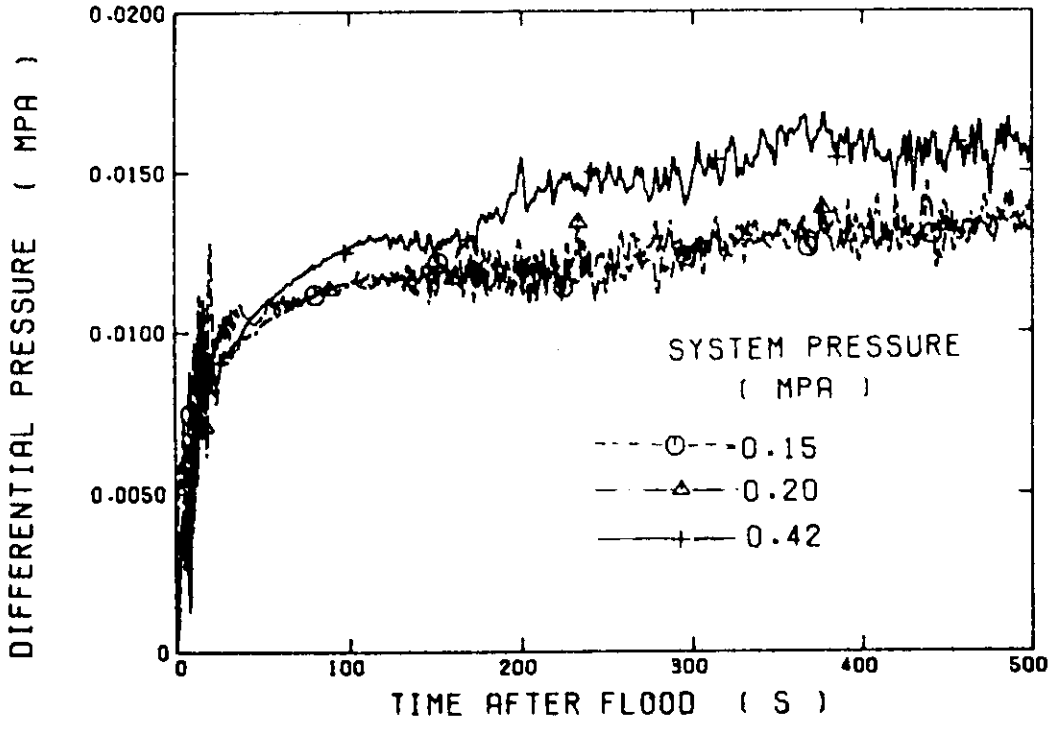

Fig. 4.2 System pressure effect on the core water head

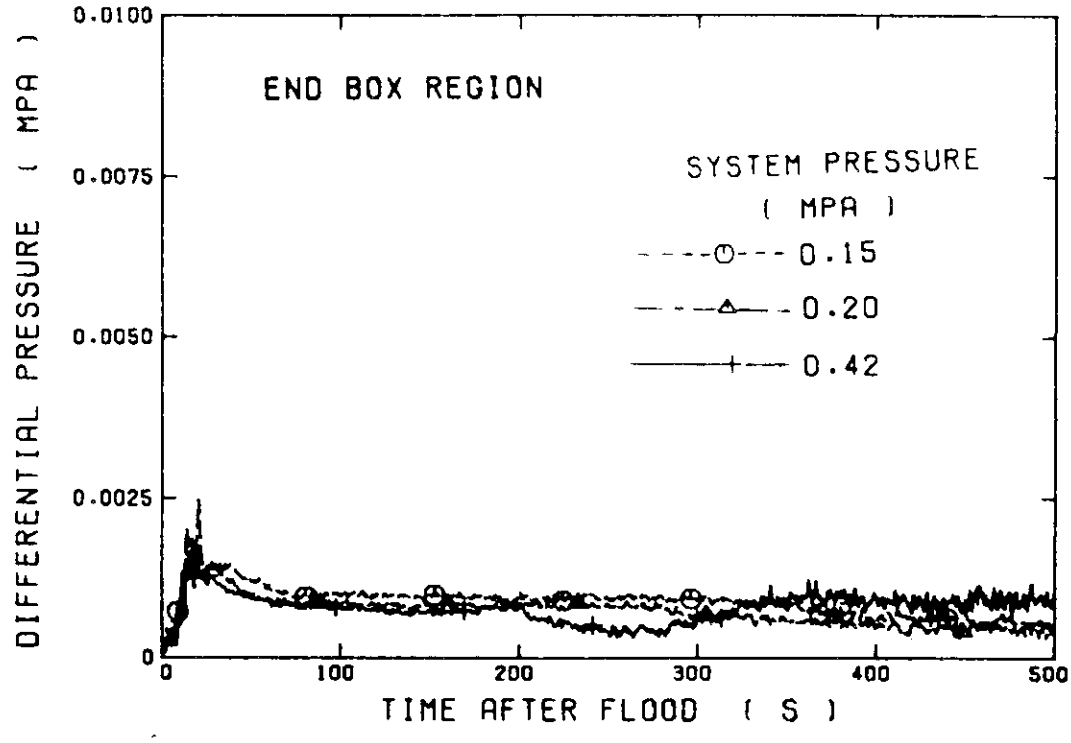

Fig. 4.3 System pressure effect on the differential pressure through the end box region

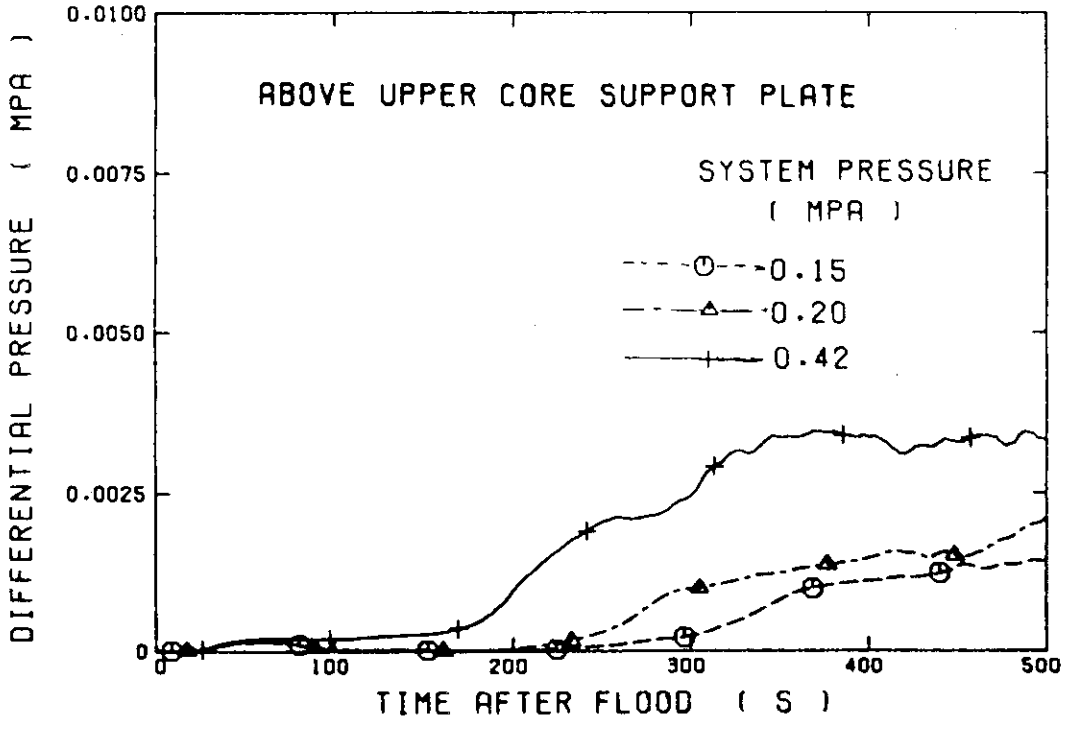

Fig. 4.4 System pressure effect on the differential pressure above upper core support plate

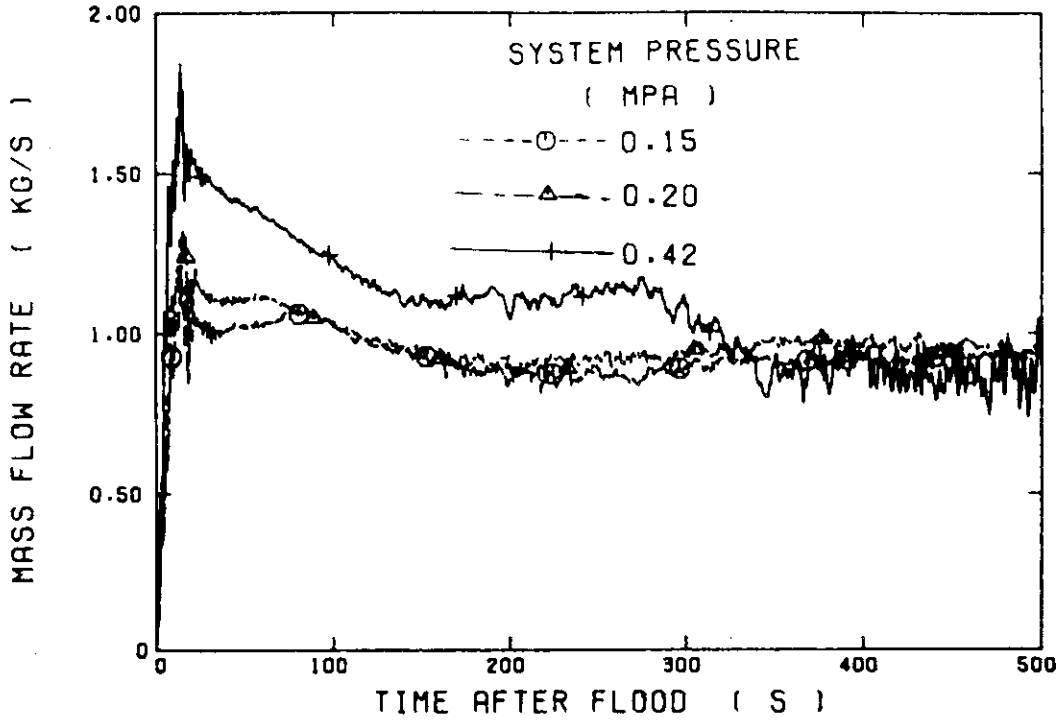

Fig. 4.5 System pressure effect on the mass flow rate through the intact loop

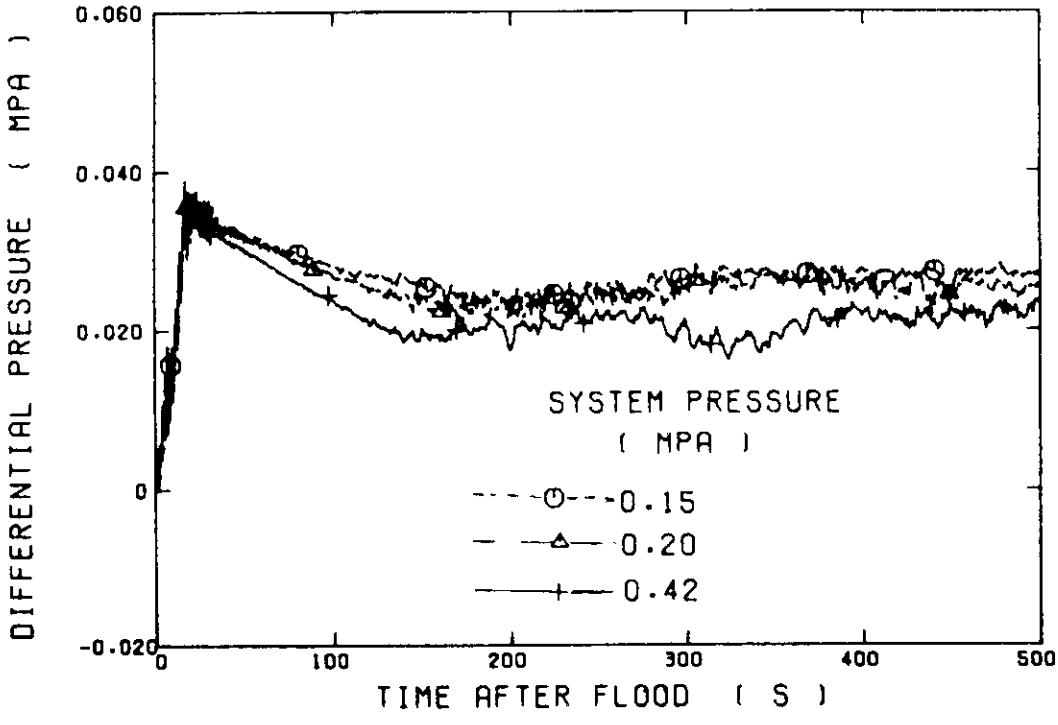

Fig. 4.6 System pressure effect on the differential pressure through the intact loop

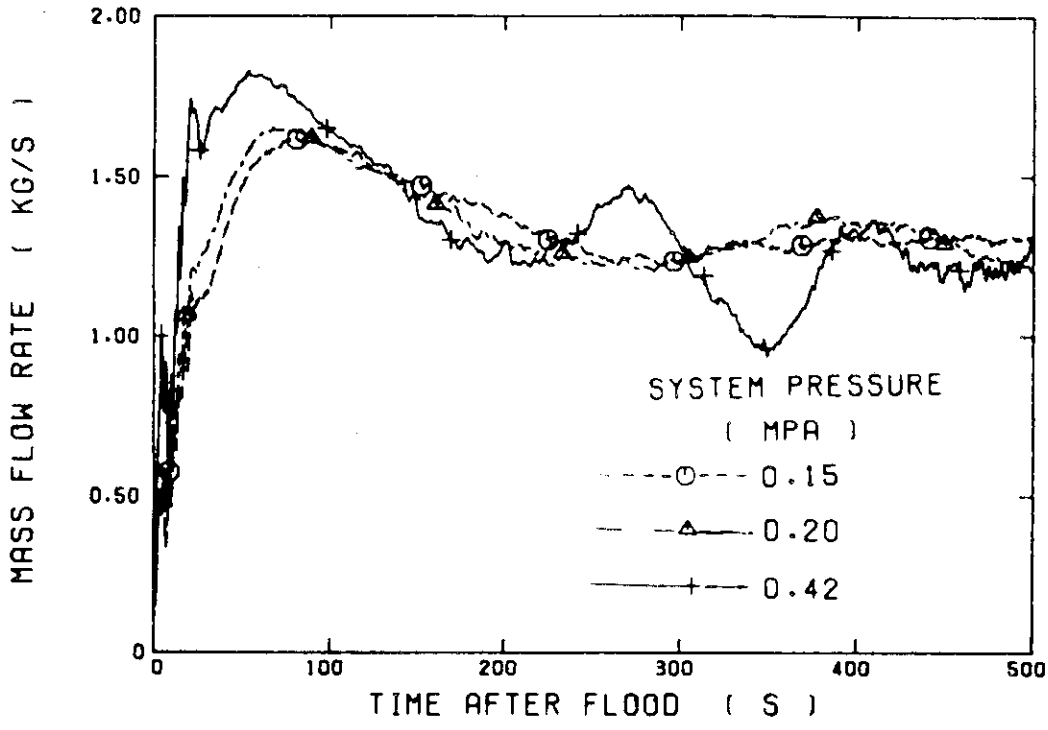

Fig. 4.7 System pressure effect on the mass flow rate through the broken loop

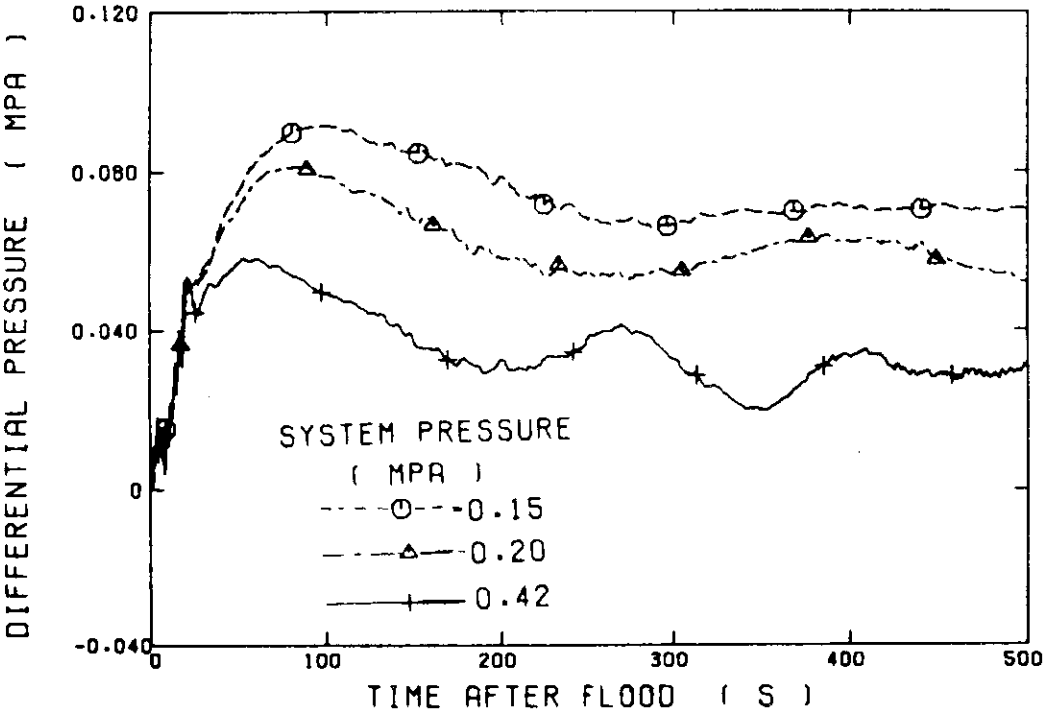

Fig. 4.8 System pressure effect on the differential pressure through the broken loop

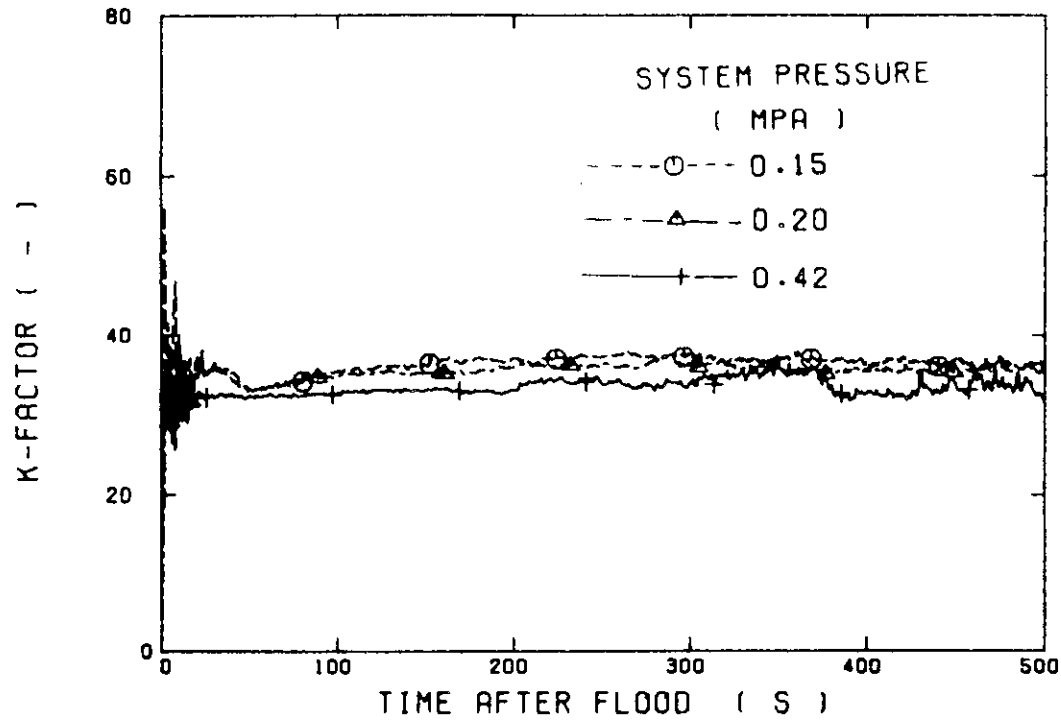

Fig. 4.9 System pressure effect on the flow resistance coefficient through the broken loop

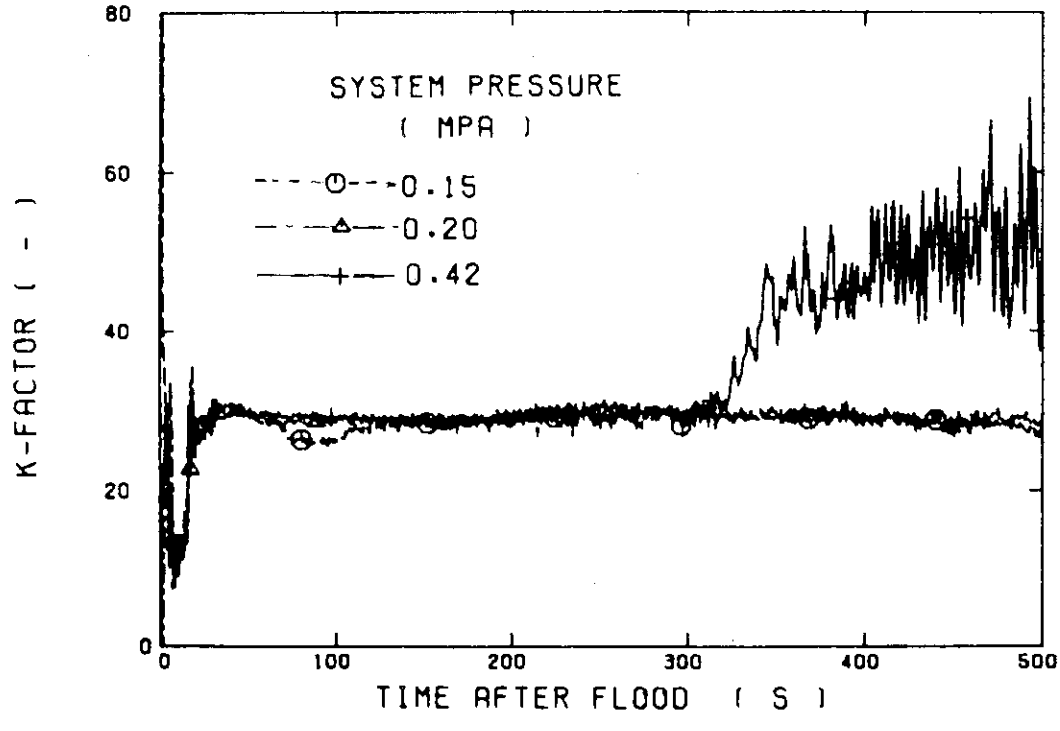

Fig. 4.10 System pressure effect on the flow resistance coefficient through the intact loop

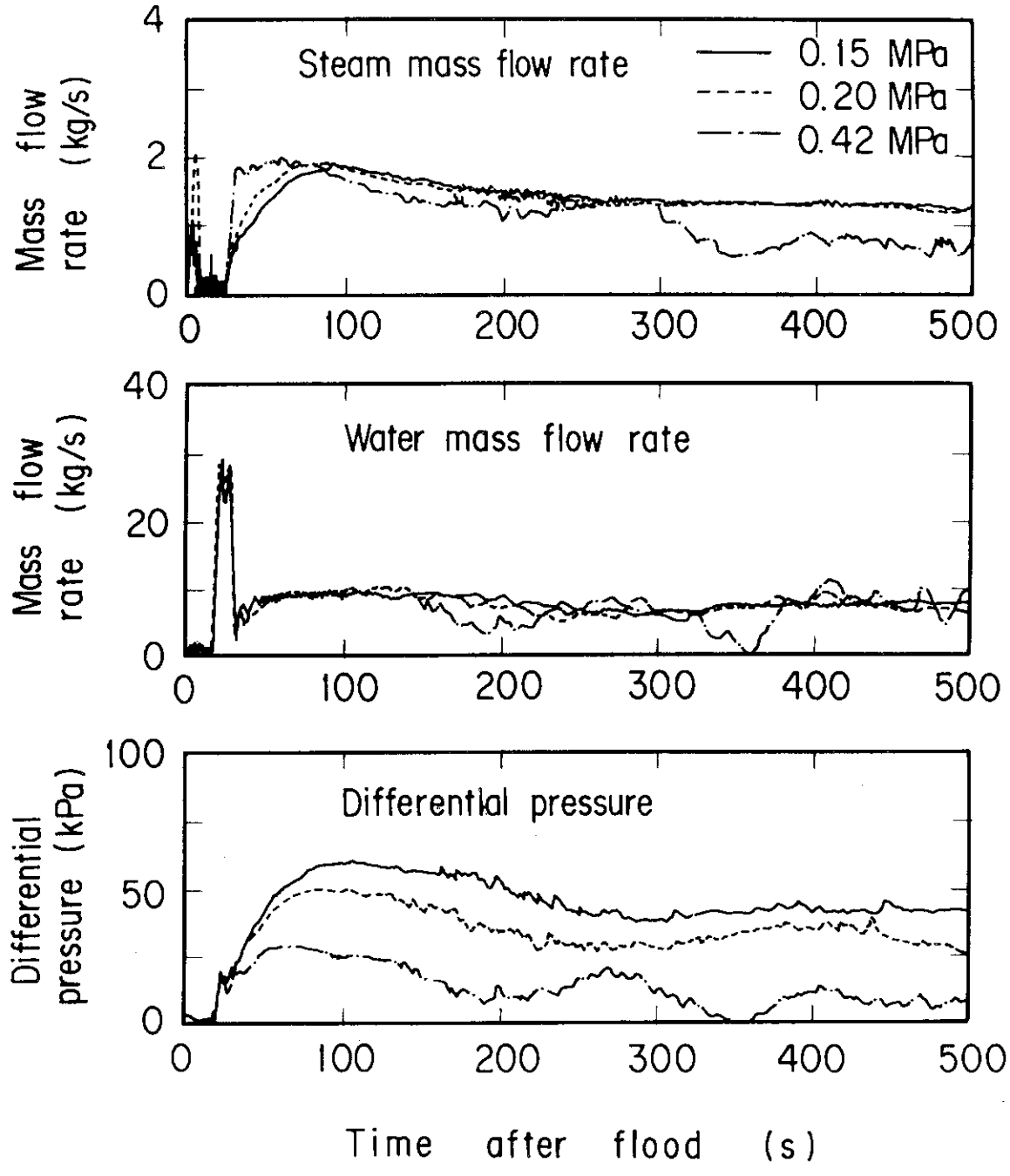

Fig. 4.11 System pressure effect on the steam and water mass flow rates and the differential pressure through the broken cold leg

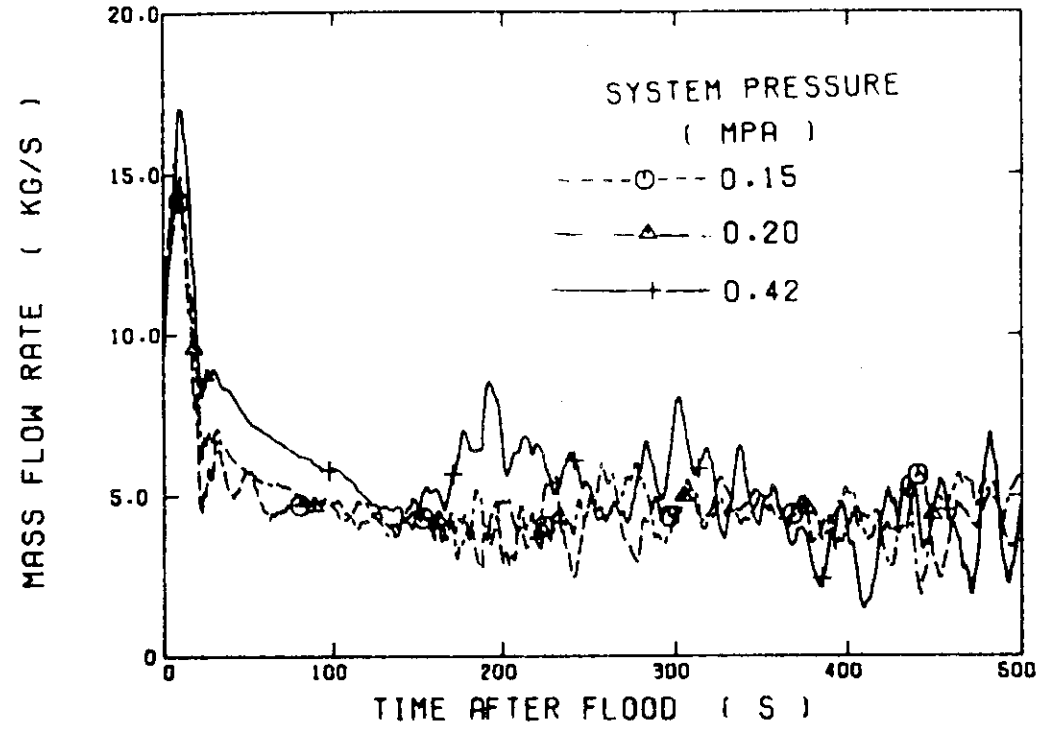

Fig. 4.12 System pressure effect on the core inlet mass flow rate

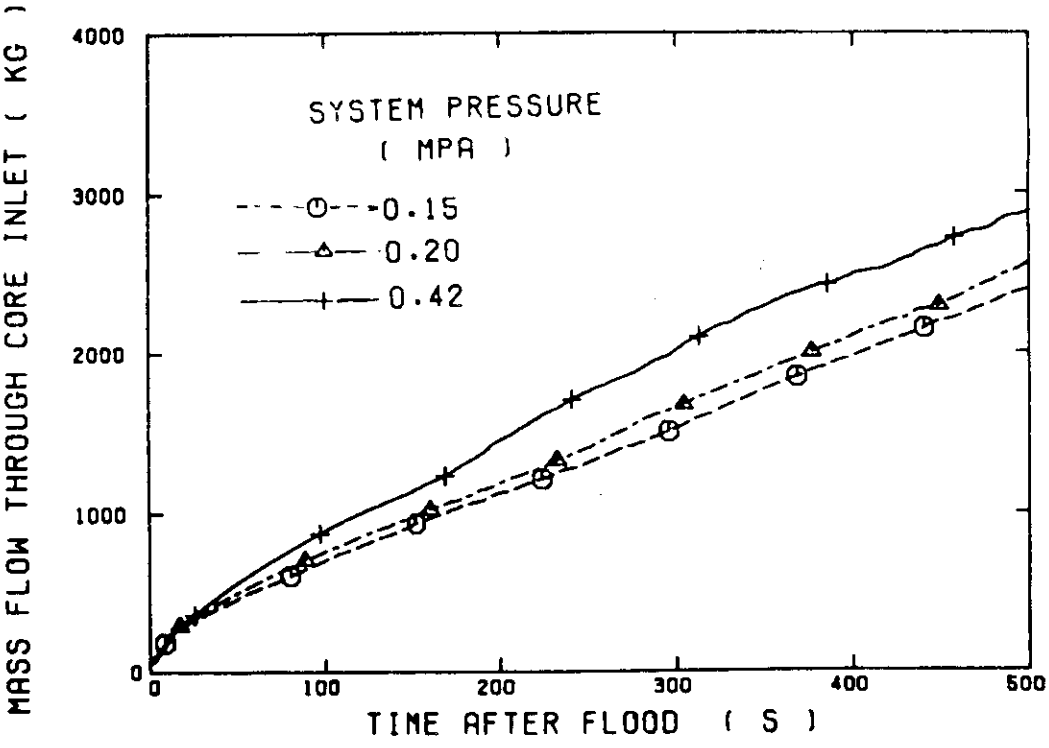

Fig. 4.13 System pressure effect on the core inlet mass flow

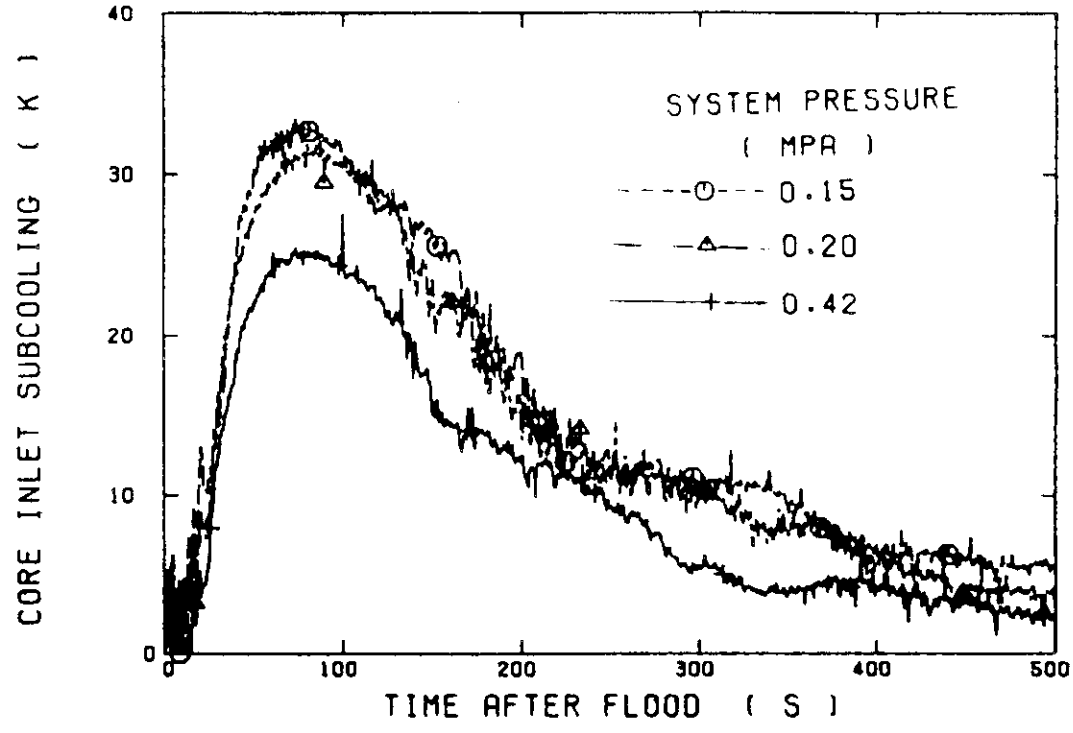

Fig. 4.14 System pressure effect on the core inlet subcooling

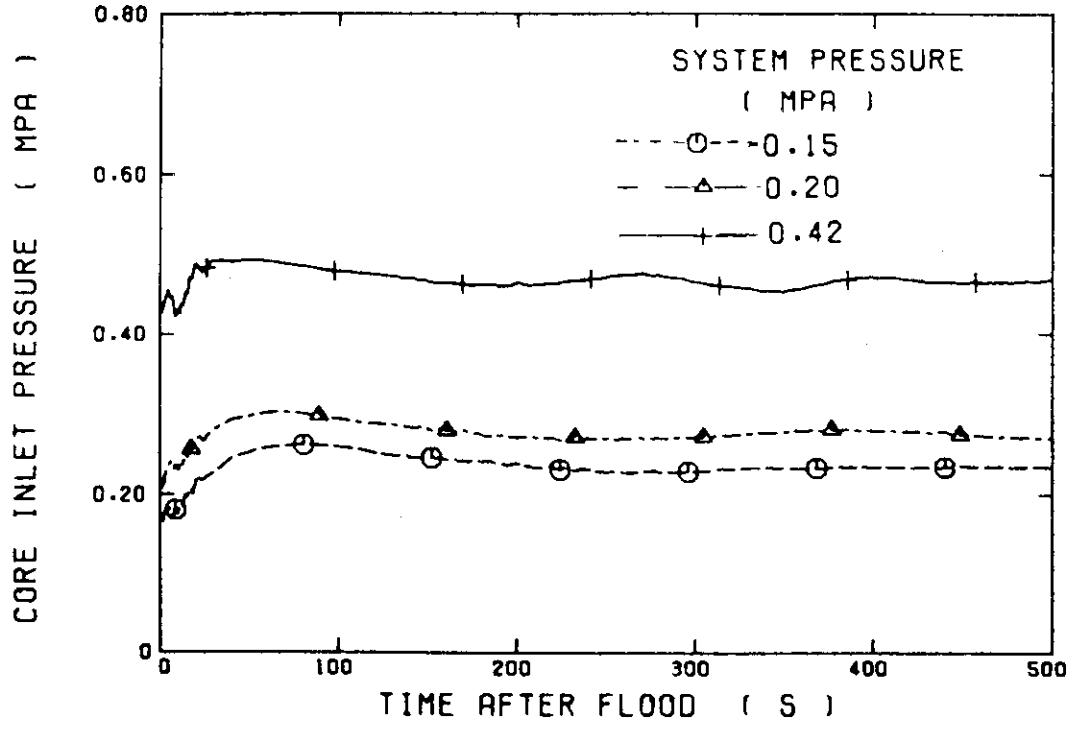

Fig. 4.15 Comparison of the core inlet pressure among the high pressure, the base case and the low pressure tests

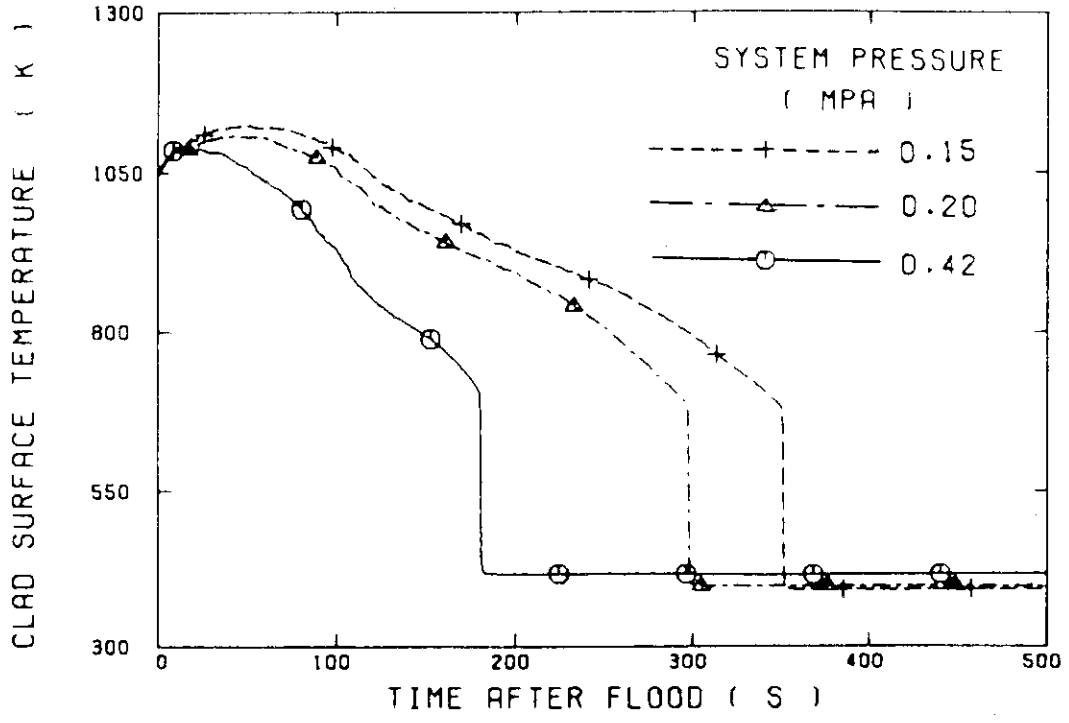

Fig. 4.16 System pressure effect on the clad surface temperature at the midplane of the peak powered rod

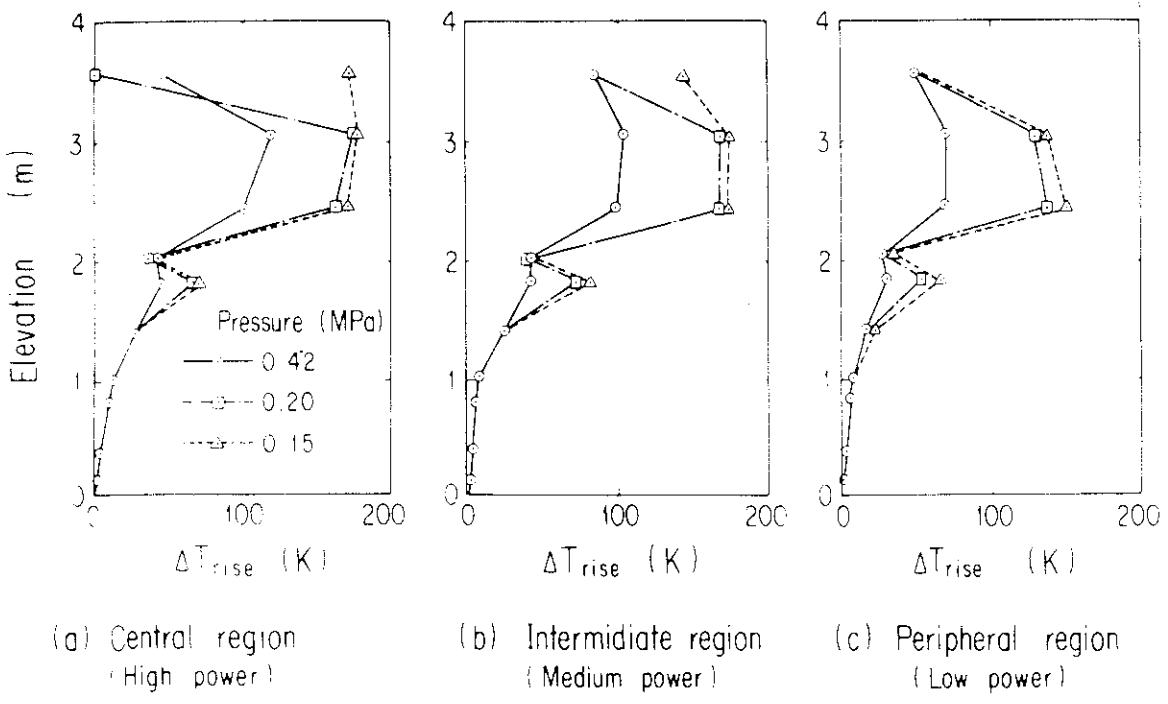

Fig. 4.17 System pressure effect on temperature rise

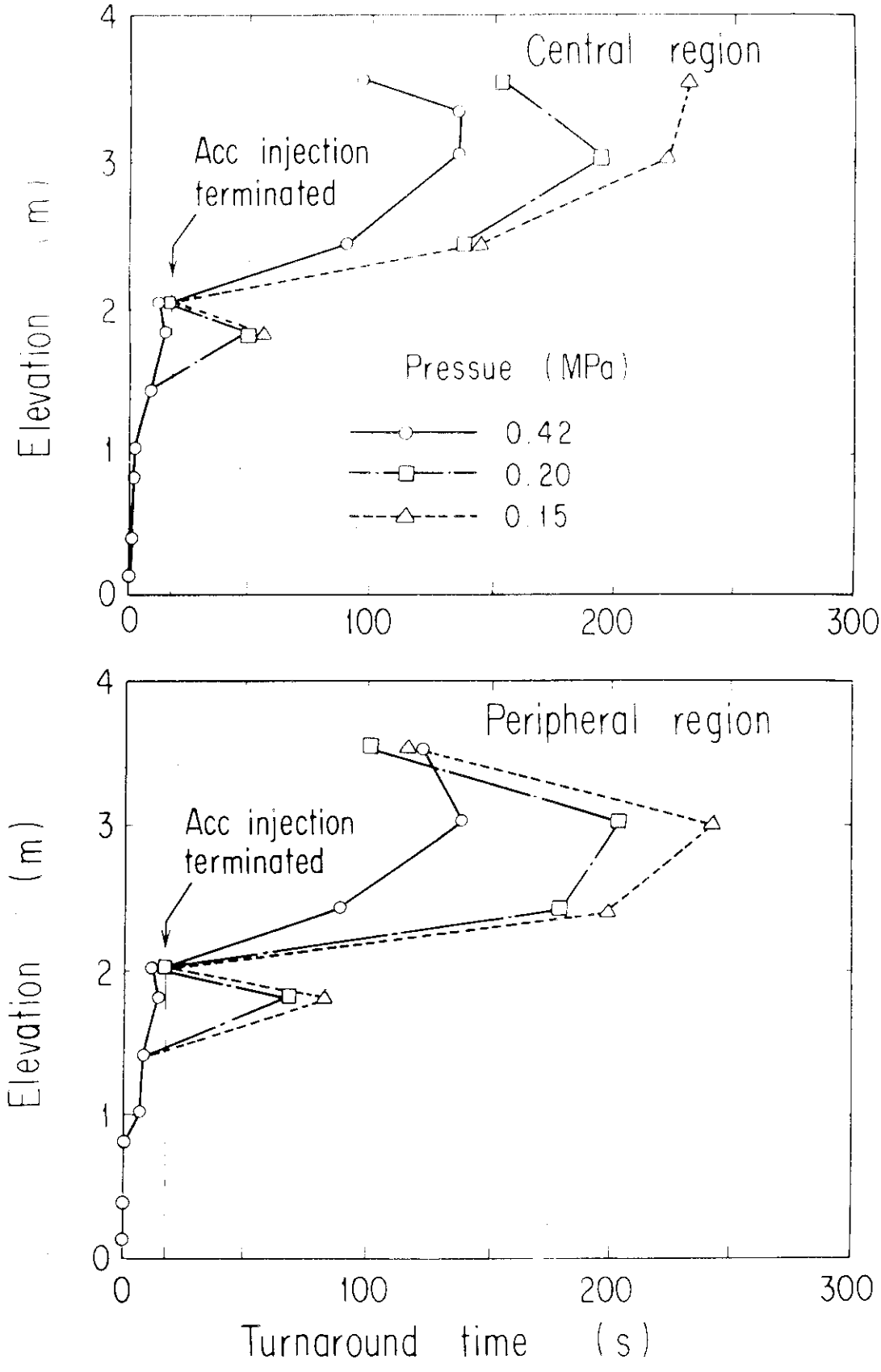

Fig. 4.18 System pressure effect on turnaround time

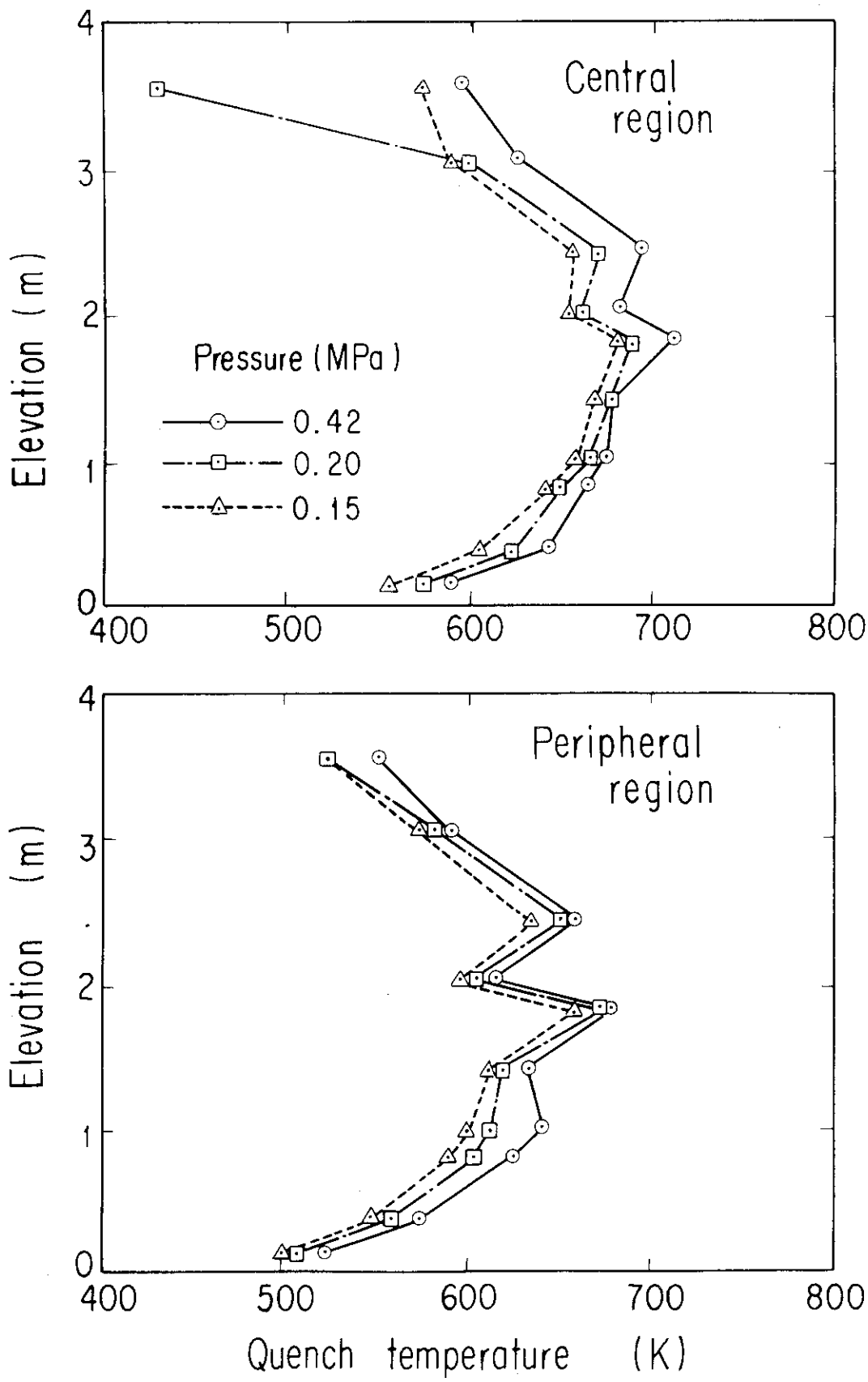

Fig. 4.19 System pressure effect on quench temperature

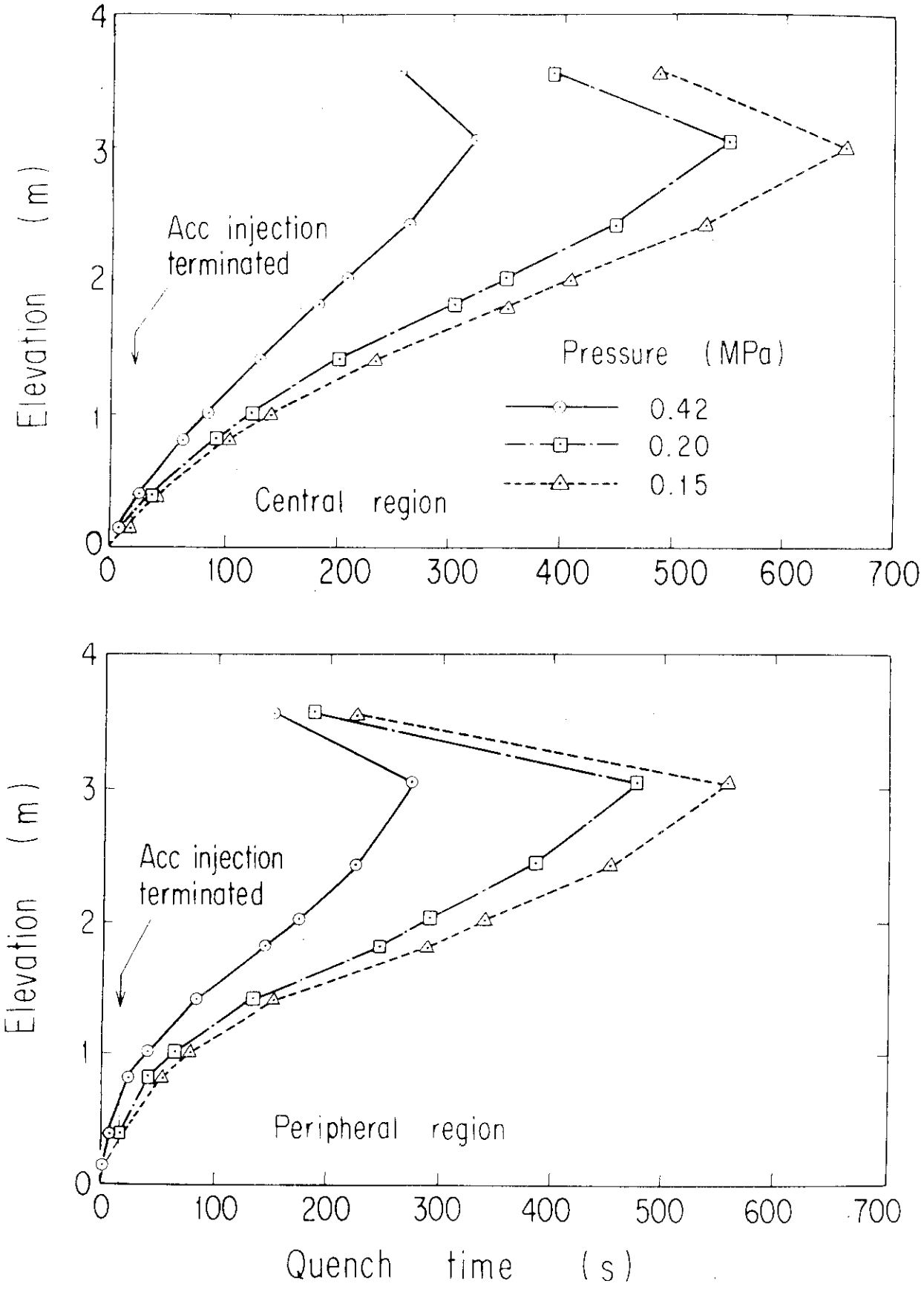

Fig. 4.20 System pressure effect on quench time

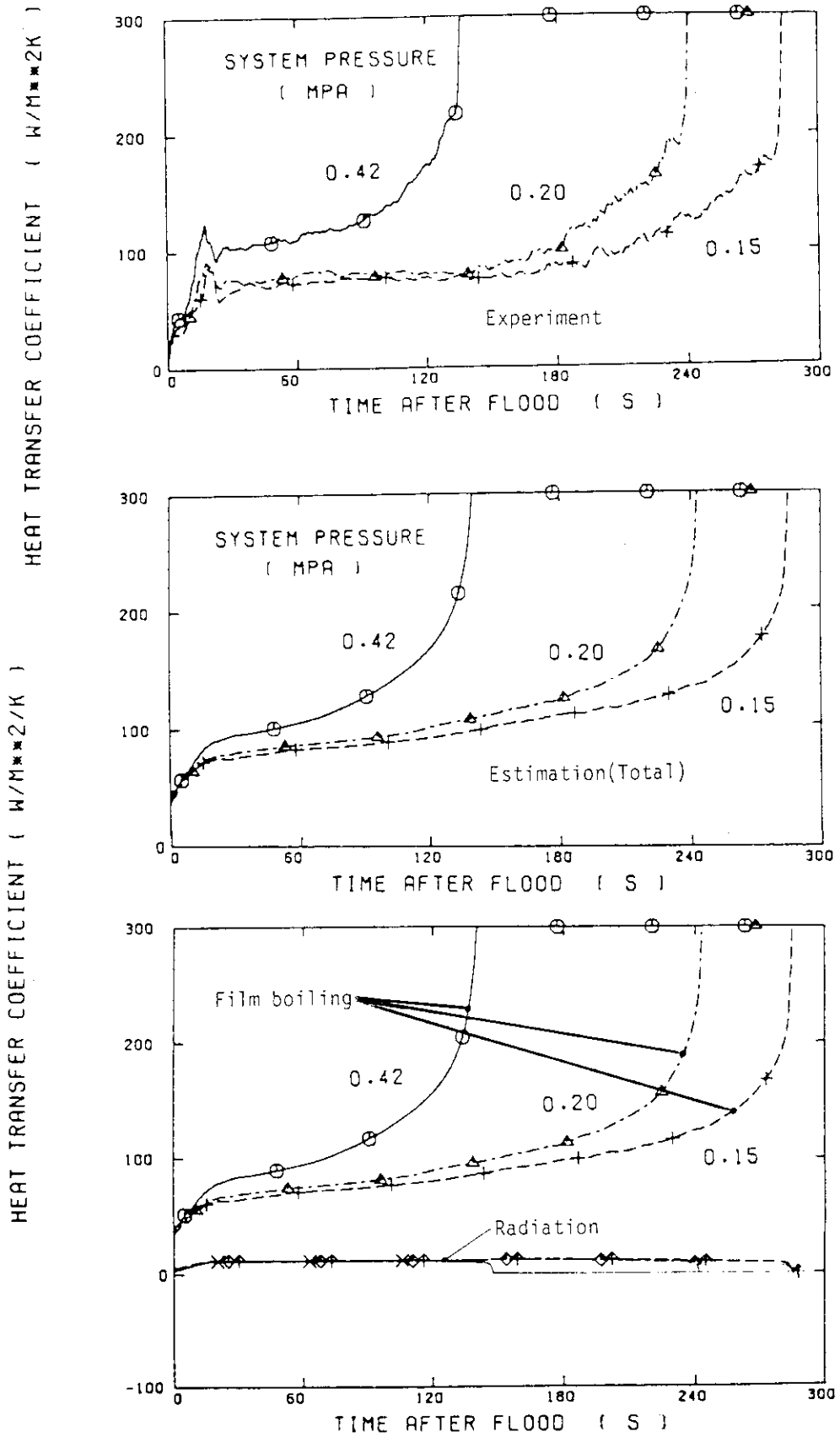

Fig. 4.21 Comparison of the heat transfer coefficient in the peripheral region between the experimental and estimated results

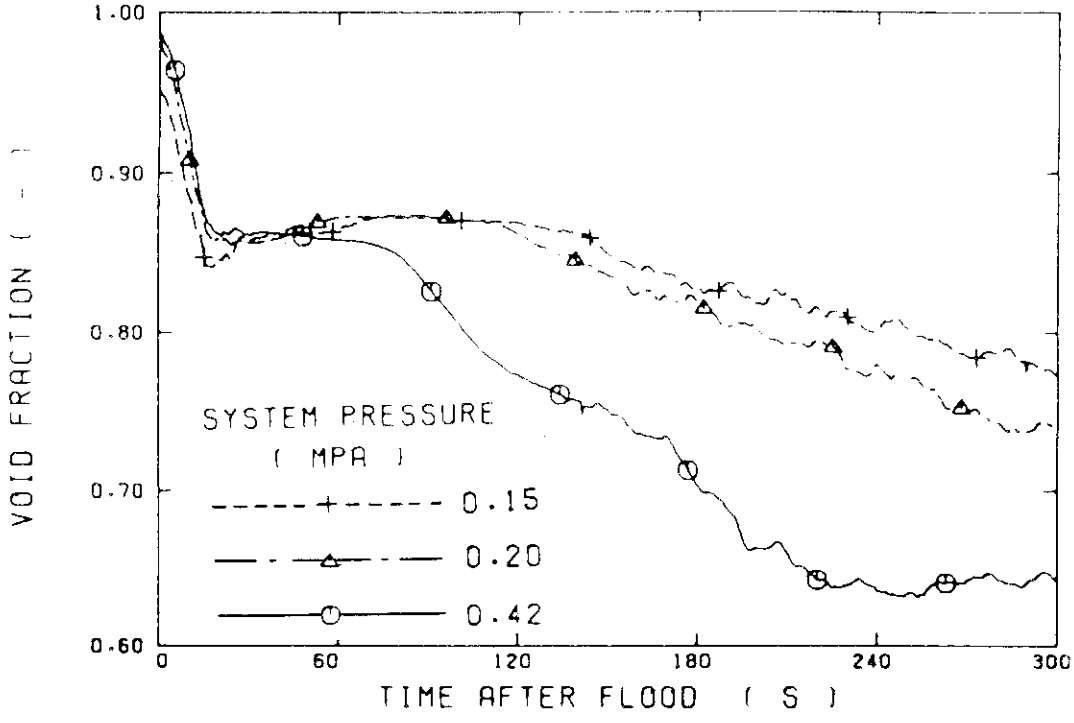

Fig. 4.22 System pressure effect on the void fraction at the elevation of 1.83 m from the bottom of the core heated part

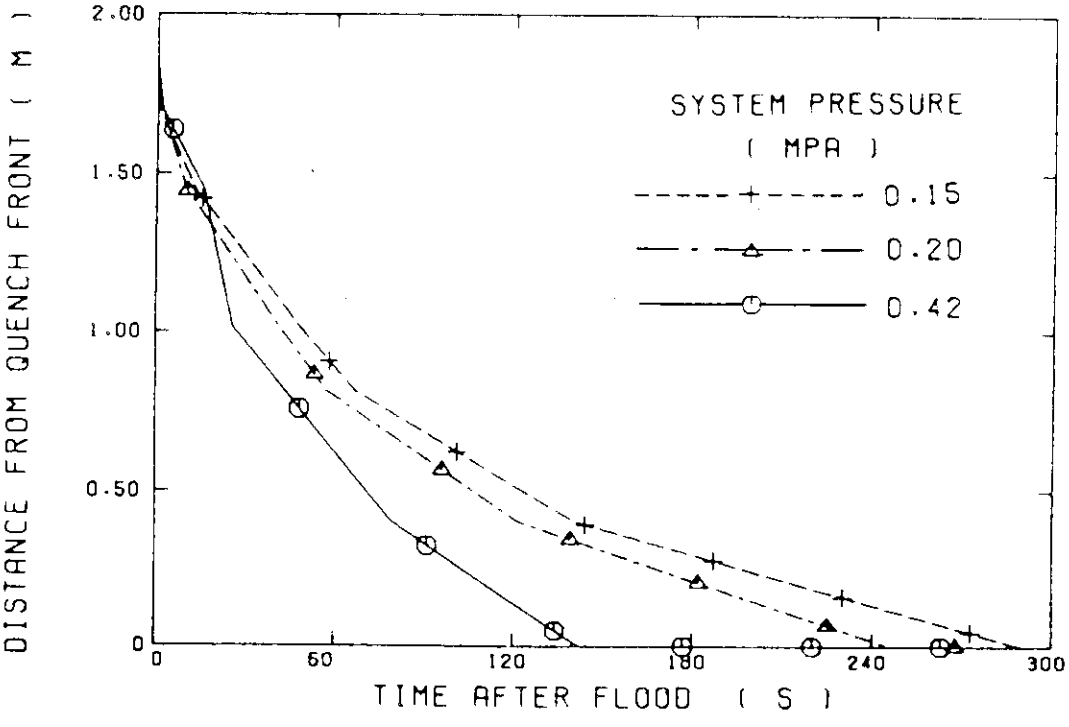

Fig. 4.23 System pressure effect of the distance from the quench front at the elevation of 1.83 m from the bottom of the core heated part

5. CONCLUSIONS

In order to study the system pressure effect of the core cooling and flow behavior during the reflood phase of a PWR LOCA, a test was performed with CCTF under the system pressure of 0.15 MPa as a counterpart test of the CCTF test C2-1(system pressure 0.42 MPa) and the CCTF test C2-4(system pressure 0.20 MPa). Through the comparisons of results from these three tests, the following conclusions were obtained:

(1) The higher system pressure resulted in the lower temperature rise, the shorter turnaround time and the shorter quench time. Based on the correlation developed by Murao and Sugimoto[8] , it is confirmed that the increase in the core heat transfer with the system pressure is attributed to the increase of the steam density in the early period(before 60 s). In the later period(after 60 s), the core heat transfer rate is increased with the system pressure due to the effect of the local void fraction and the distance from the quench front in addition to the effect of the steam density.

(2) The higher system pressure resulted in higher core water head, higher upper plenum water head, higher mass flow rate through the primary loops. On the other hand, the higher system pressure resulted in lower downcomer water head and lower pressure drop through the primary loops and the broken cold leg. These system pressure effects on the flow behavior in the primary system are almost the same as observed in the similar tests in the CCTF Core-I test series.

(3) Before the mixture level in the upper plenum reached the level of the hot leg nozzle, the loop flow resistance coefficient of the intact loops was nearly constant regardless of the system pressure. After the mixture level reached the level of the hot leg nozzle, the loop flow resistance coefficient was increased due to the water accumulation in the hot leg piping and the inlet plenum of the steam generator in these tests.

Acknowledgements

The authors are much indebted to Drs. M. Nozawa, K. Hirano, K. Sato, and T. Shimooke of Japan Atomic Energy Research Institute (JAERI) for their guidance and encouragement for this program.

The authors would like to express appreciation to the members of SCTF analysis group, especially Messrs. H. Adachi, T. Iwamura, A.Ohnuki and Y. Abe for valuable discussions. The authors are deeply indebted to Messrs. Y.Fukaya, I. Arase, T. Wakabayashi, T.Oyama, Y. Niitsuma, K. Nakajima, T. Chiba, J. Matsumoto, K. Komori and H. Sonobe for their contribution of the test conduction.

References

(1)Hirano,K. and Murao Y., J. At. Energy Soc. Japan,(in Japanese), 22(10), 681 (1980).

(2)Murao,Y.,et al., 12 th water reactor safety research information meeting, October (1984).

(3)Murao,Y.,et al., J. Nucl. Sci. Technol.,19(9),705 (1982).

(4)Akimoto,H. and Murao,Y., JAERI-M 83-091, June (1983).

(5)Sawan,M.E. and Carbon, M.W., Nucl. Eng. Des.,32,191 (1975).

(6)Lilly,G.P., et al., WCAP-8838, (1977).

(7)Waring,J.P. and Hochreiter,L.E., WCAP-8583, (1975).

(8)Murao,Y. and Sugimoto,J.,J. Nucl. Sci. Technol.,18(4),275 (1981).

(9)Sugimoto, J. and Murao, Y., J. Nucl. Sci. Technol., 21 (2), 103 (1984).

Acknowledgements

The authors are much indebted to Drs. M. Nozawa, K. Hirano, K. Sato, and T. Shimooke of Japan Atomic Energy Research Institute (JAERI) for their guidance and encouragement for this program.

The authors would like to express appreciation to the members of SCTF analysis group, especially Messrs. H. Adachi, T. Iwamura, A.Ohnuki and Y. Abe for valuable discussions. The authors are deeply indebted to Messrs. Y.Fukaya, I. Arase, T. Wakabayashi, T.Oyama, Y. Niitsuma, K. Nakajima, T. Chiba, J. Matsumoto, K. Komori and H. Sonobe for their contribution of the test conduction.

References

(1)Hirano,K. and Murao Y., J. At. Energy Soc. Japan,(in Japanese), 22(10), 681 (1980).

(2)Murao,Y.,et al., 12 th water reactor safety research information meeting, October (1984).

(3)Murao,Y.,et al., J. Nucl. Sci. Technol.,19(9),705 (1982).

(4)Akimoto,H. and Murao,Y., JAERI-M 83-091, June (1983).

(5)Sawan,M.E. and Carbon, M.W., Nucl. Eng. Des.,32,191 (1975).

(6)Lilly,G.P., et al., WCAP-8838, (1977).

(7)Waring,J.P. and Hochreiter,L.E., WCAP-8583, (1975).

(8)Murao,Y. and Sugimoto,J.,J. Nucl. Sci. Technol.,18(4),275 (1981).

(9)Sugimoto, J. and Murao, Y., J. Nucl. Sci. Technol., 21 (2), 103 (1984).

Appendix A

Definition of Tag IDs for data in Appendix B

Figure List

1. Definition of Tag. ID for clad surface temperatures and heat fransfer coefficients

Notation : TEnnYlm (temperature)

HTEmmYlm (heat transfer coefficient)

nn : Bundle number (see Fig. A.1)

m : Elevation number

	Elevation (m)	Axial power factor
3	0.38	0.651
5	1.015	1.147
7	1.83	1.40
9	2.44	1.256
A	3.05	0.854

2. Definition of power zone and boundle number

See Fig. A.1

3. Definition of Tag. ID for void fraction

See Fig. A.2

4. Definition of Tag. ID for average linear power of heater rod in each power unit zone

See Fig. A.3

5. Definition of Tag. ID for differential pressure through downcomer, upper plenum, core and lower plenum

See Fig. A.4

6. Definition of Tag. ID for differential pressure through intact and broken loop and broken cold leg nozzle

See Fig. A.5

7. Definition of Tag. ID for fluid temperature in inlet and outlet plenum and secondary side of steam generator

See Fig. A.6

8. Definition of Tag. ID for ECC water injection rate, ECC water temperature and vented steam flow rate

See Fig. A.7

9. Definition of initial temperature, turnaround temperature quench temperature, temperature rise, turnaround time and quench time. (See Fig. A.8

T_i : Initial temperature (Clad surface temperature at reflood initiation)

T_t : Turnaround temperature (Maximum clad surface temperature in each temperature history)

ΔT_r : Temperature rise ($= T_t - T_i$)

T_q : Quench temperature (Clad surface temperature at quenching)

10. Definition of quenching

See Fig. A.8

Quench time t_t is determined as

$$t_t = i \times \Delta t - \text{(reflood initiation time)}$$

In above equation, i is determined by the following criteria.

(1) Clad surface temperature is high, compared with the saturation temperature.

$$T_i > T_{sat} + \Delta T_1$$

(2) Decreasing rate of clad surface temperature is large.

$$\frac{T_{i+1} - T_i}{\Delta t} < - C_{st}$$

(3) Clad surface temperature falls around the saturation temperature.

$$T_{i + k_1} \leq T_{sat} + \Delta T_1$$

(4) If the determined i is inadequate, the value i is manually re-determined.

Δt : Data sampling period (s)

T_i : Clad surface temperature (K)

T_{sat} : Saturation temperature at the pressure in upper plenum (K)

ΔT_1 : Temperature discrepancy (K)
Default value = 50.0

C_{st} : Decreasing rate of clad surface temperature (K/S)
Default value = 25.0

k_1 : Number of referred data (-)
Default value = 6

11. Definition of Tag. ID for core inlet mass flow rate, time-integral core inlet mass flow rate and carry-over rate fraction

(1) Core inlet mass flow rate : $\dot{m}_F$
Notation : MLCRI□ (□ = N, 1 or 11)

(2) Time-intefral core inlet mass flow rate : $\int \dot{m}_F dt$
Notation : IMLCRI□ (□ = N, 1 or 11)

(3) Carry-over rate fraction : $(\dot{m}_F - \dot{m}_{CR})/\dot{m}_F$
Natation : CRF□ (□ = N, 1 or 11)

where $\dot{m}_F$: Core inlet mass flow rate (See item 12)

$\dot{m}_{CR}$: Water accumulation rate in core

Suffix	$\dot{m}_F$ base on
N	Eq.(A.2)
1	Eq.(A.1) with K=15
11	Eq.(A.1) with K=20

12. Evaluation of core inlet mass flow rate

The reflood phenomena is a relatively slow transient and a steady state condition can be applied. In a steady state condition, based on the mass balance relations of the system, the core flooding mass flow rates $\dot{m}_F$s can be written as follows:

By using the data measured at the downstream of the core inlet, $\dot{m}_F$ is derived as,

$$\dot{m}_F = \dot{m}_C + \dot{m}_U + \dot{m}_B + \Sigma \dot{m}_I \quad , \qquad (A.1)$$

where $\dot{m}_C$ and $\dot{m}_U$ are the mass accumulation rates in the core and the upper plenum respectively. The $\dot{m}_B$ and $\dot{m}_I$ are the mass flow rates in the broken loop and the intact loop, respectively.

By using the data measured at the upstream of the core inlet, $\dot{m}_F$ is derived as,

$$\dot{m}_F = \Sigma \dot{m}_{DL} - \dot{m}_D - \dot{m}_O + \dot{m}_{ECC/LP} \quad , \tag{A.2}$$

where $\dot{m}_{DL}$ and $\dot{m}_O$ are the mass flow rates of the water flowing into and overflowing from the downcomer, $\dot{m}_{ECC/LP}$ and $\dot{m}_D$ are the mass flow rate of the ECC water injected into the lower plenum and the water accumulation rate in the dowmcomer respectively.

The $\dot{m}_I$s and $\dot{m}_B$ can be obtained from the pressure drops at the pump simulators with orifices by assuming the K-factor of the orifice is constant. The values of $\dot{m}_C$, $\dot{m}_D$ and $\dot{m}_U$ can be evaluated with the differential pressure ΔP_C, ΔP_D and ΔP_U, respectively, as follows:

$$\dot{m}_n = d(\Delta P_n S_n/g)/dt \quad (n : C, D, U) \quad , \tag{A.3}$$

where g is the gravitational acceleration and S_n is the cross sectional area. The value of $\dot{m}_O$ can be obtained from the liquid level X in the Containment tank 1 as,

$$\dot{m}_O = d(X\rho_\ell S_o)/dt \quad , \tag{A.4}$$

where ρ_ℓ is the liquid density and S_o is the cross sectional area of the containment tank 1.

The value of $\dot{m}_{DL}$, $\dot{m}_{DV}$ and h, which are liquid flow rate, steam flow rate and enthalpy of two phase mixture downstream each ECC port respectively, are obtained from the following mass and energy balance relations at each ECC port under the assumption of thermal equilibrium:

$$\dot{m}_{DV} + \dot{m}_{DL} = \dot{m}_{ECC} + \dot{m}_I \quad , \tag{A.5}$$

$$(\dot{m}_{DV} + \dot{m}_{DL})i = \dot{m}_{ECC}h_{ECC} + \dot{m}_I h_I \quad , \tag{A.6}$$

$$\text{if} \quad h_g \geq h \geq h_\ell \ , \ (\dot{m}_{DV} + \dot{m}_{DL})h = \dot{m}_{DV}h_g + \dot{m}_{DL}h_\ell$$

$$\text{if} \quad h \geq h_g \quad , \ \dot{m}_{DL} = 0 \quad , \tag{A.7}$$

$$\text{if} \quad h \geq h_\ell \quad , \ \dot{m}_{DV} = 0$$

where h is enthalpy of fluid and h_ℓ and h_g are enthalpies of liquid and steam at the saturation temperature, respectively.

The fluid temperatures can be measured with thermocouples immersed in the fluid and the enthalpies h_I and h_{ECC} can be estimated.

Mass balance calculations were performed with Eqs. (A.1) and (A.2). The K-factor of the orifice in the pump simulator was evaluated in the following two ways.

The K-factor of 20 was obtained with the steam and water single phase calibration tests using the flow meter and spool piece data. The K-factor of 15 was obtained with the Pitot tube measurement in a typical reflood condition assuming the flat velocity profile in the pipings. In the differentiation, higher frequency components of the data tends to be amplified more. Therefore, in the differentiation of the differential pressure data, the smoothing procedure was used to suppress the high frequency components of the data.

In the Acc injection period, the calculated $\dot{m}_F$s with Eqs. (A.1) and (A.2) are significantly different from each other. This discrepancy may be caused by inaccuracy of the mass flow rate injected into the system and by the unaccounting of the storage of water in the cold leg pipe. The former might be introduced from the slow time response of the flow meter (time constant 1 second) and the change of the gas volume in the injection line. In this period, especially before the steam generation from the core becomes noticeable, the mass flow rate, $\dot{m}_F$, calculated with Eq. (A.1) is probably reasonable, since the calculation uses the increasing rates of the masses in the core and the upper plenum and their accuracy is good enough for our estimation.

In the LPCI injection period, the calculated $\dot{m}_F$s are slightly different from each other. Judging from the time-integral values of both $\dot{m}_F$s, their average values are nearly proportional. The discrepancy was inferred to be caused by the disregard of the bypass of steam and liquid from the upper plenum without going through the hot legs in the calculation with Eq. (A.1). And additionally the discrepancy was caused by the disregard of the steam generation in the downcomer due to the hot wall of the pressure vessel in the calculation with Eq. (A.2). It was estimated that the disregard of the downcomer steam generation causes the error of 0.25 kg/s on predicted $\dot{m}_F$. The estimation was made by comparing the results of the tests with hot and cold downcomer conditions.

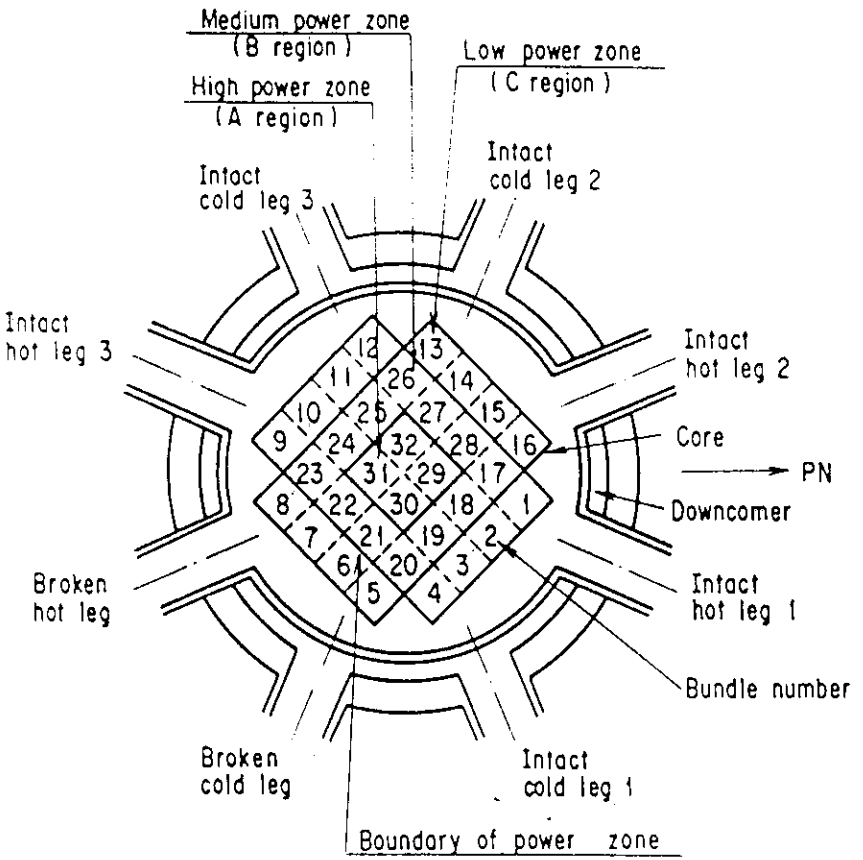

Fig. A. 1 Definition of power zones and bundle numbers

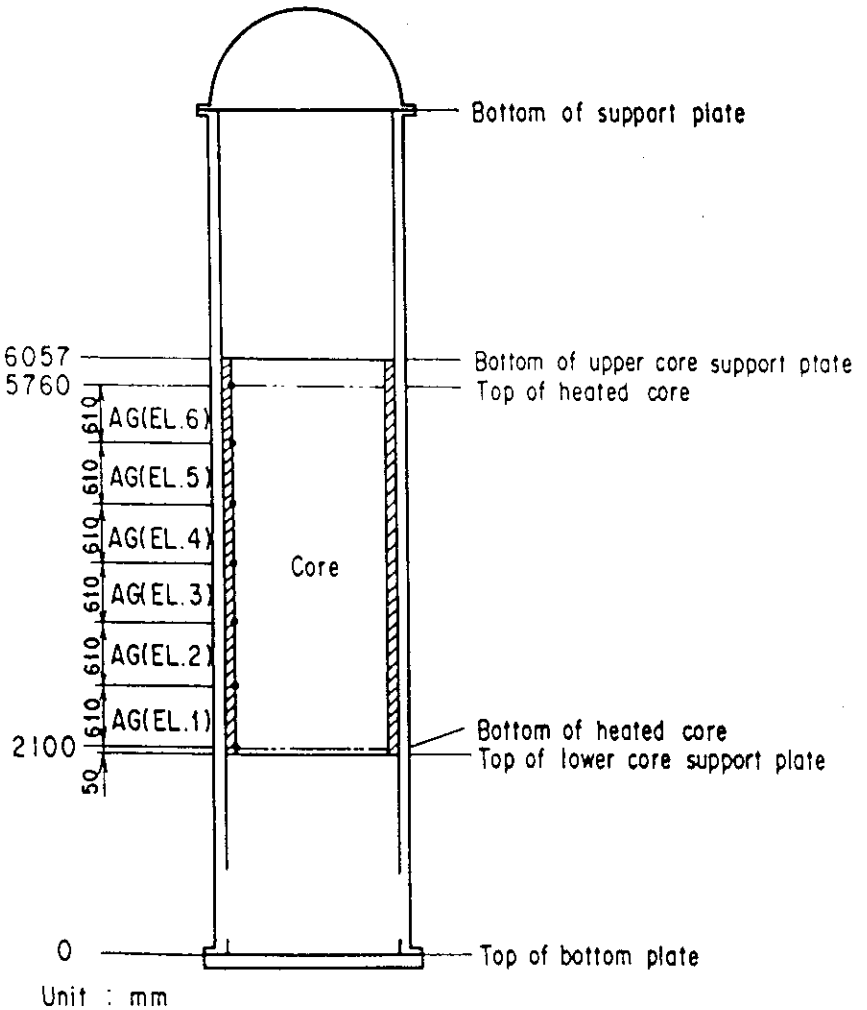

Fig. A. 2 Definition of Tag ID for void fraction (AG(EL. 1) ~ AG(EL. 6))

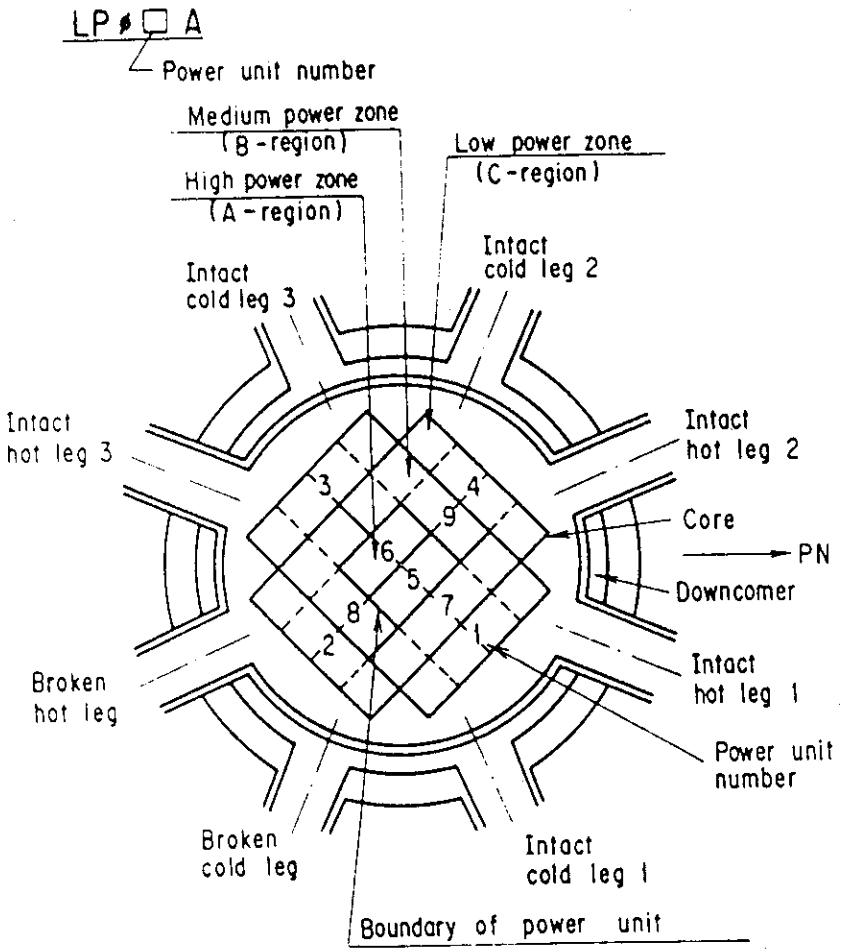

Fig. A. 3 Definition of Tag. ID for average linear power of heater rod in each power unit zone
(LP01A ~ LP09A)

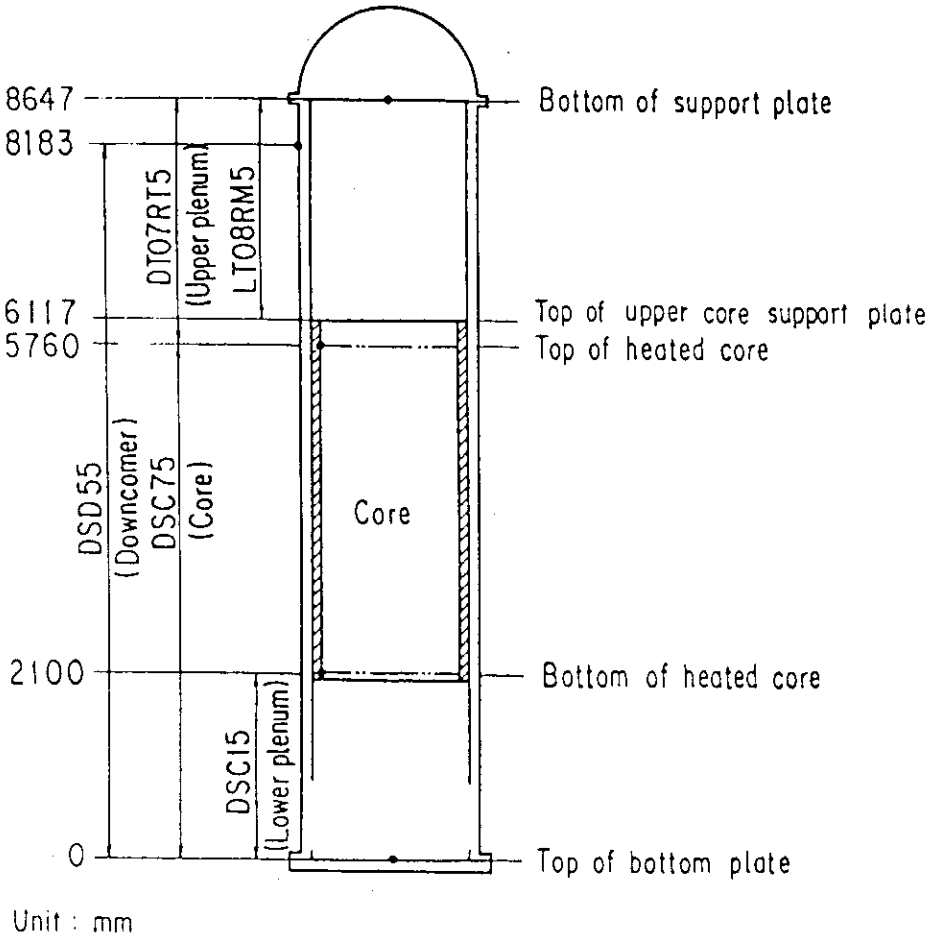

Fig. A. 4 Definition of Tag. ID for differential pressure through downcomer, upper plenum, core, and lower plenum
(DSD55, DT07RT5, LT08RM5, DSC75, DSC15)

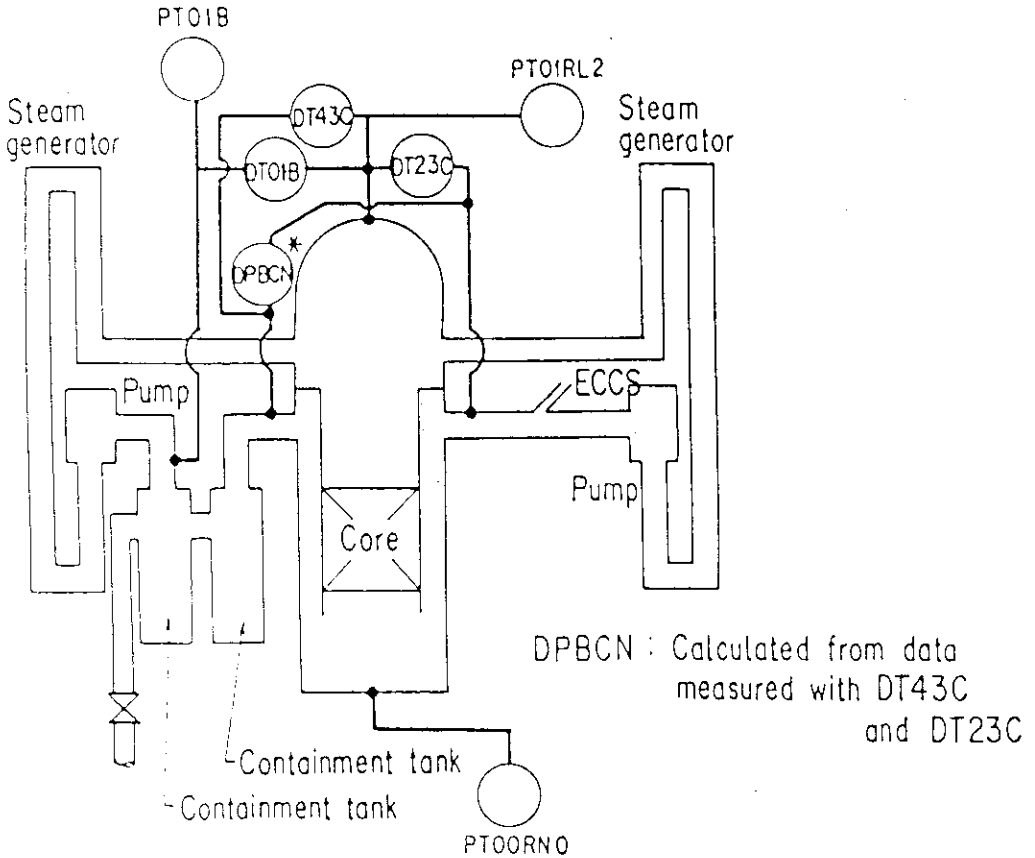

Fig. A. 5 Definition of Tag. ID for pressures in upper and lower plena and containment tank 2 (PT01RL2, PT00RN0, PT01B) and for differential pressure through intact and broken loop and broken cold leg nozzle (DT23C, DT01B, DPBCN)

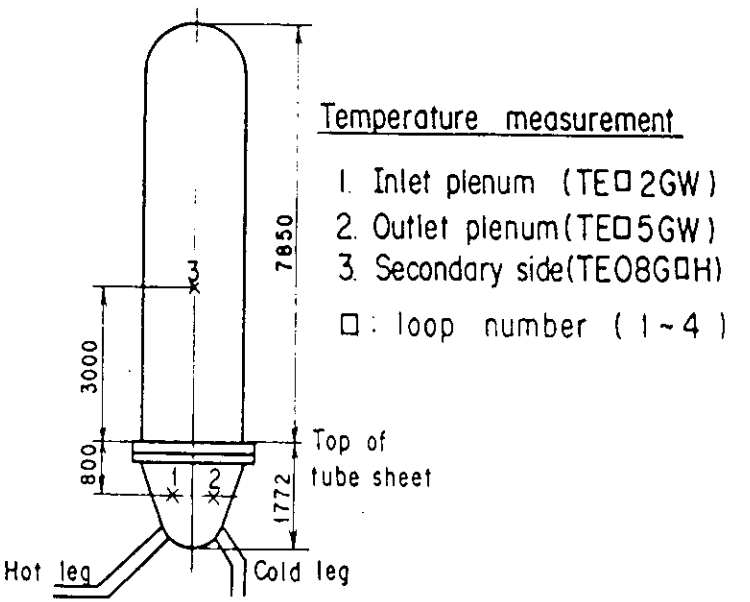

Fig. A. 6 Definition of Tag. ID for fluid temperature in inlet and outlet plenum and secondary of steam generator (TE□2GW, TE□5GW, TE08G□H)

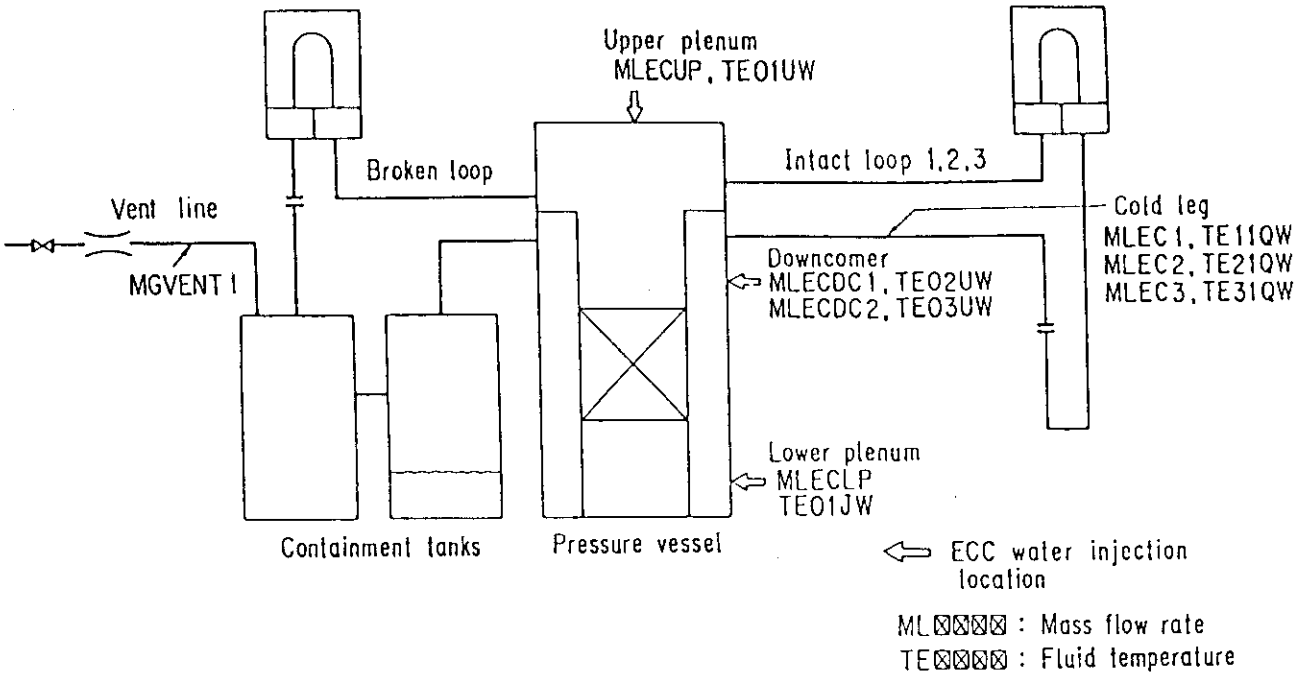

Fig. A. 7 Definition of Tag. ID for ECC water injection rate, ECC water temperature and vented steam flow rate

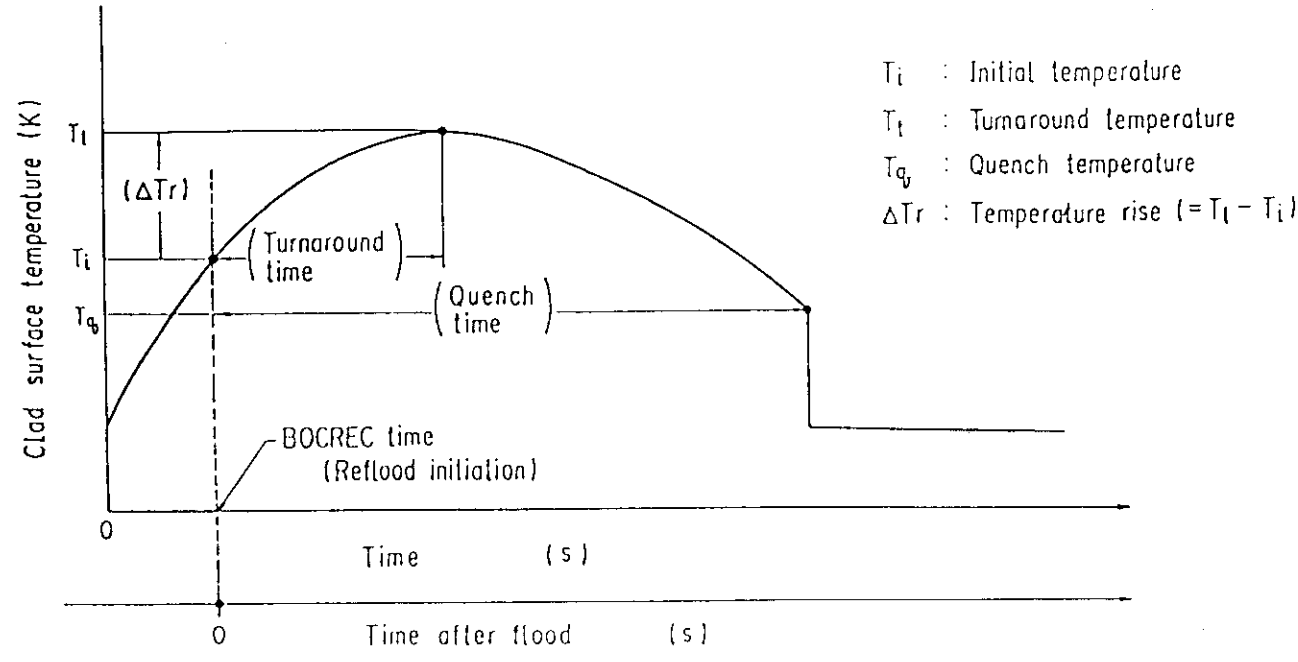

Fig. A. 8 Definition of initial temperature, turnaround temperature, quench temperature, temperature rise, turnaround time and quench time

Appendix B

Selected data of CCTF Test C2-8 (Run 67)

Figure List

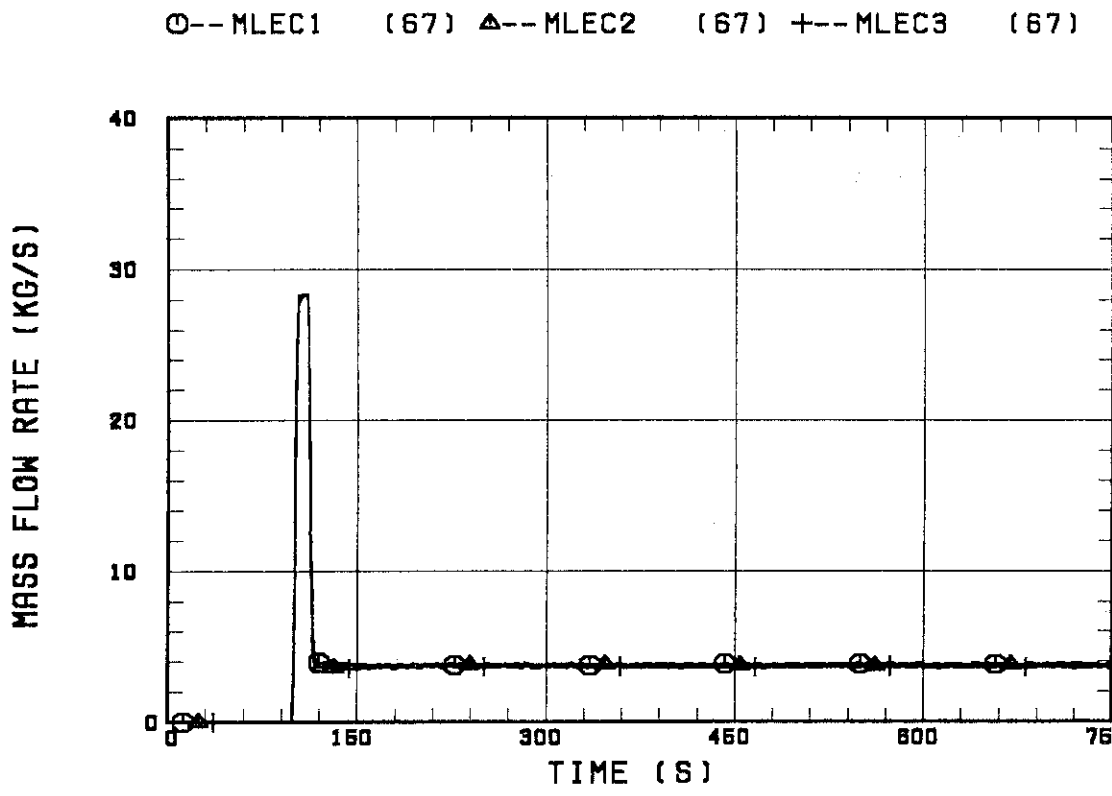

Fig. B.1 ECC water injection rates into the primary system.

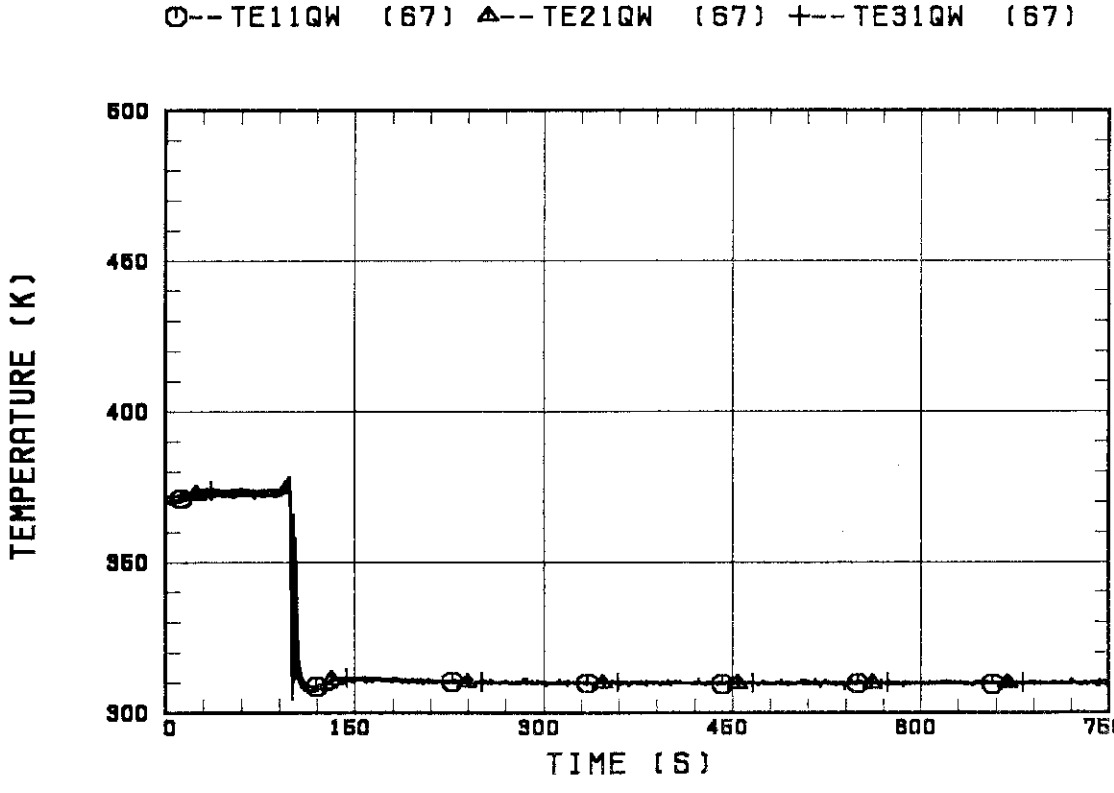

Fig. B.2 ECC water temperature.

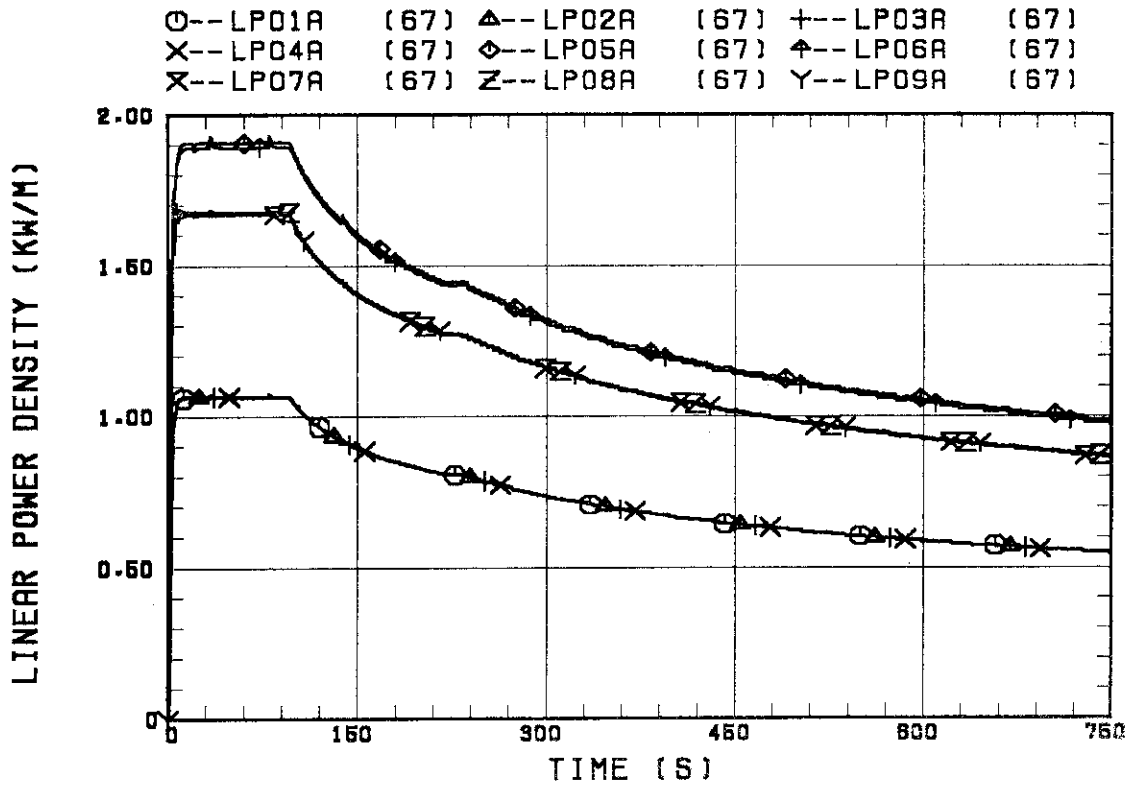

Fig. B.3 Average linear power of heater rod in each power unit zone.

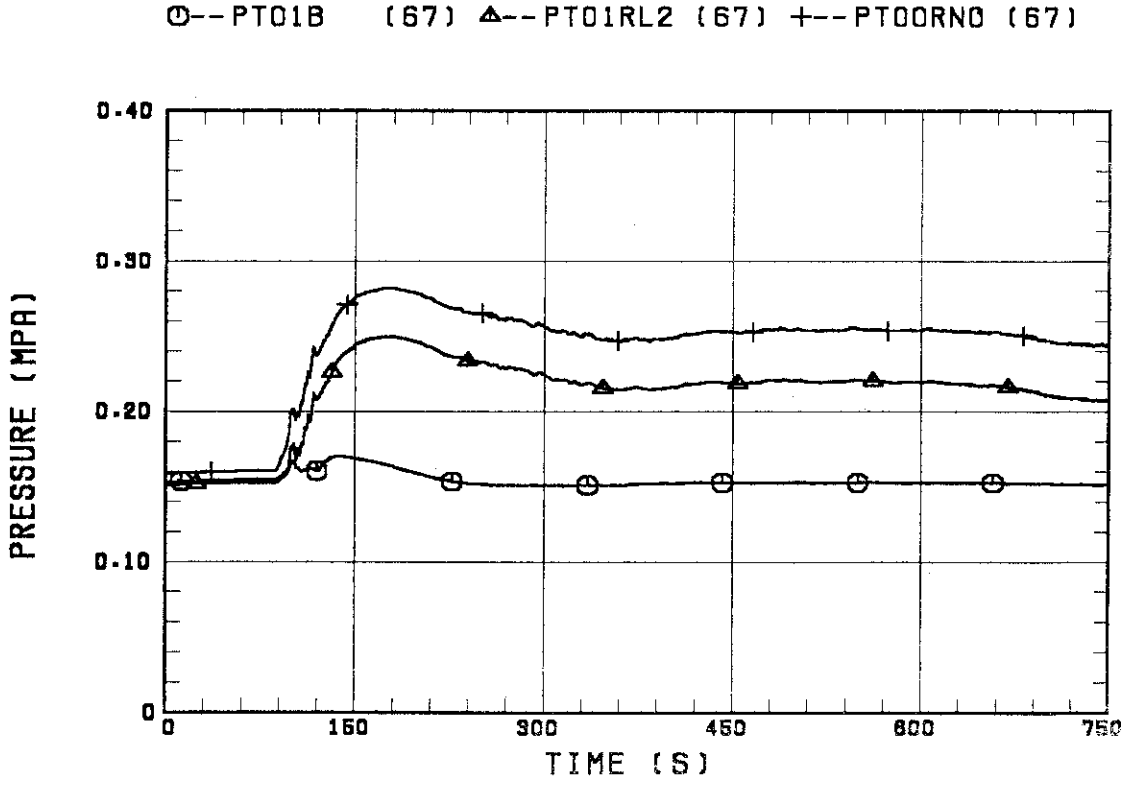

Fig. B.4 Pressure history in containment tank 2, upper plenum and lower plenum.

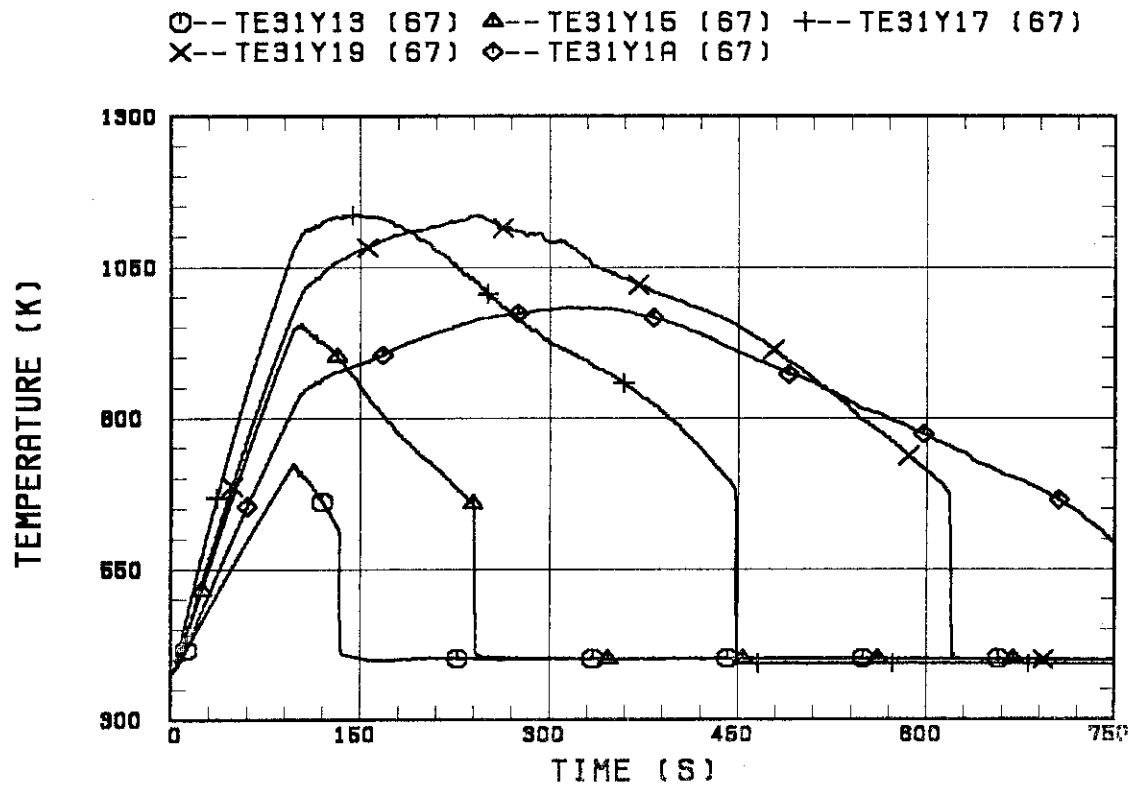

Fig. B.5 Clad surface temperature at various elevations along a heater rod in high power region (A region).

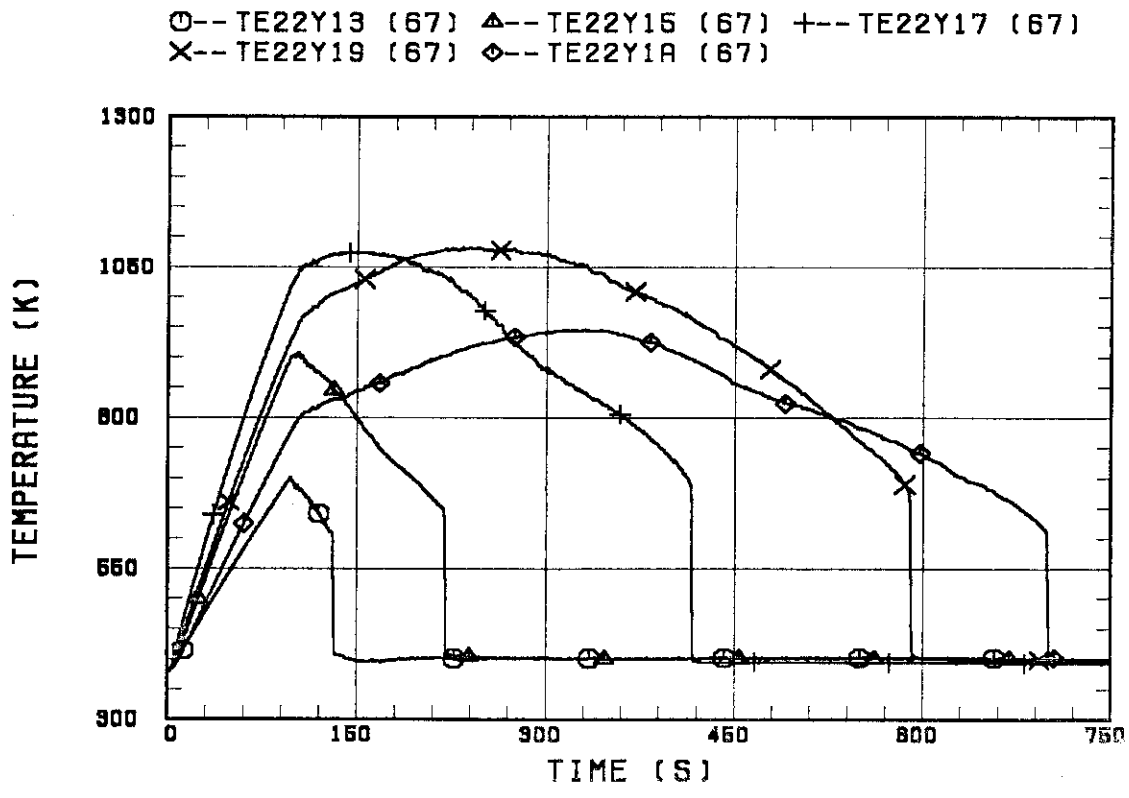

Fig. B.6 Clad surface temperature at various elevations along a heater rod in medium power region (B region).

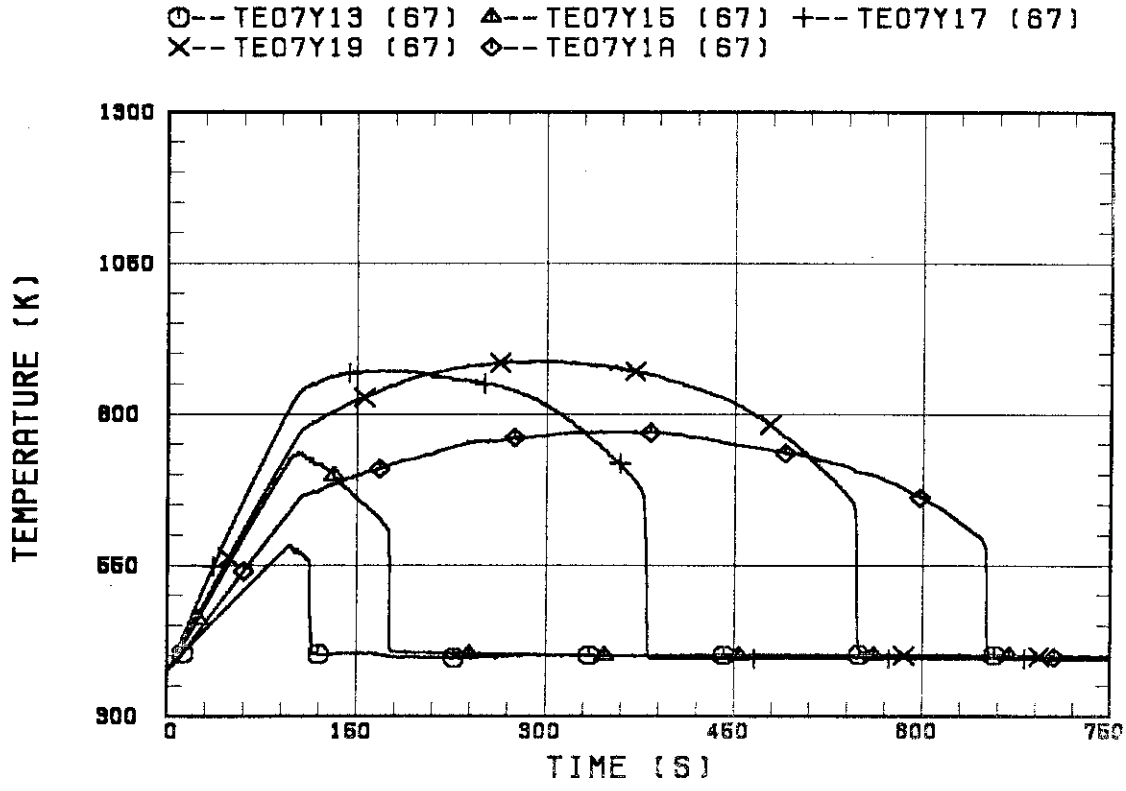

Fig. B.7 Clad surface temperature at various elevations along a heater rod in low power region (C region).

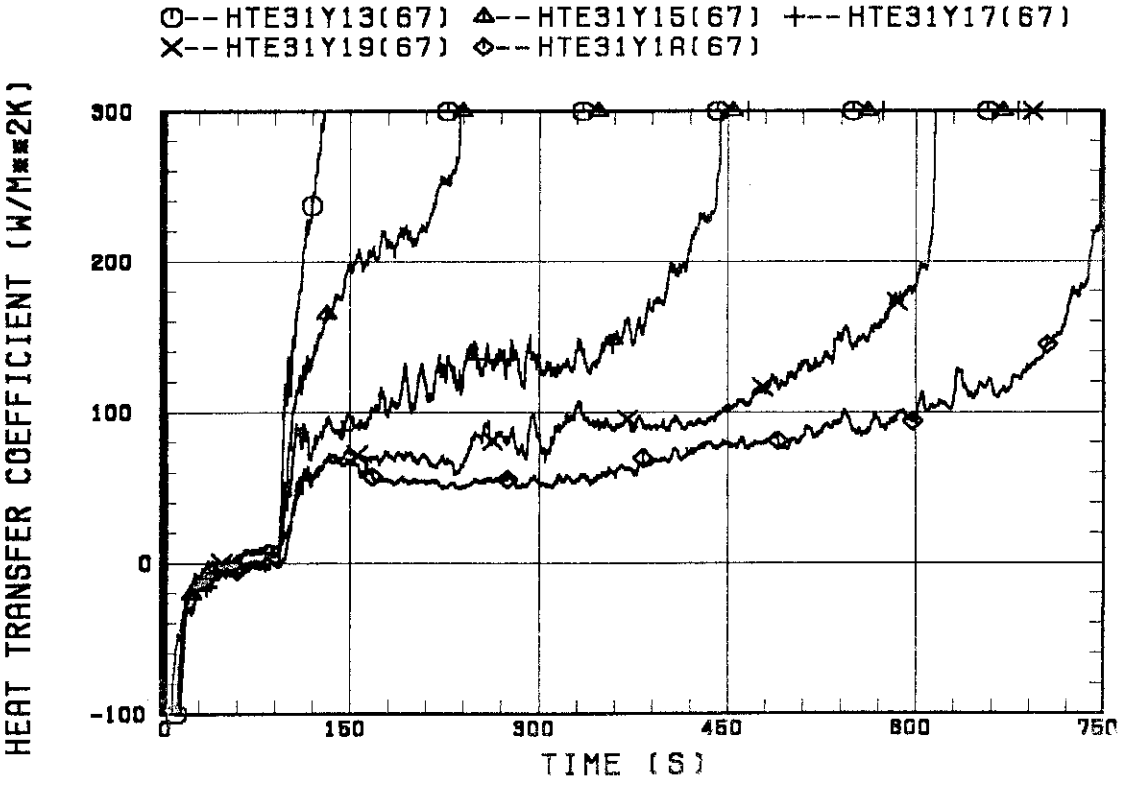

Fig. B.8 Heat transfer coefficient at various elevations along a heater rod in high power region (A region).

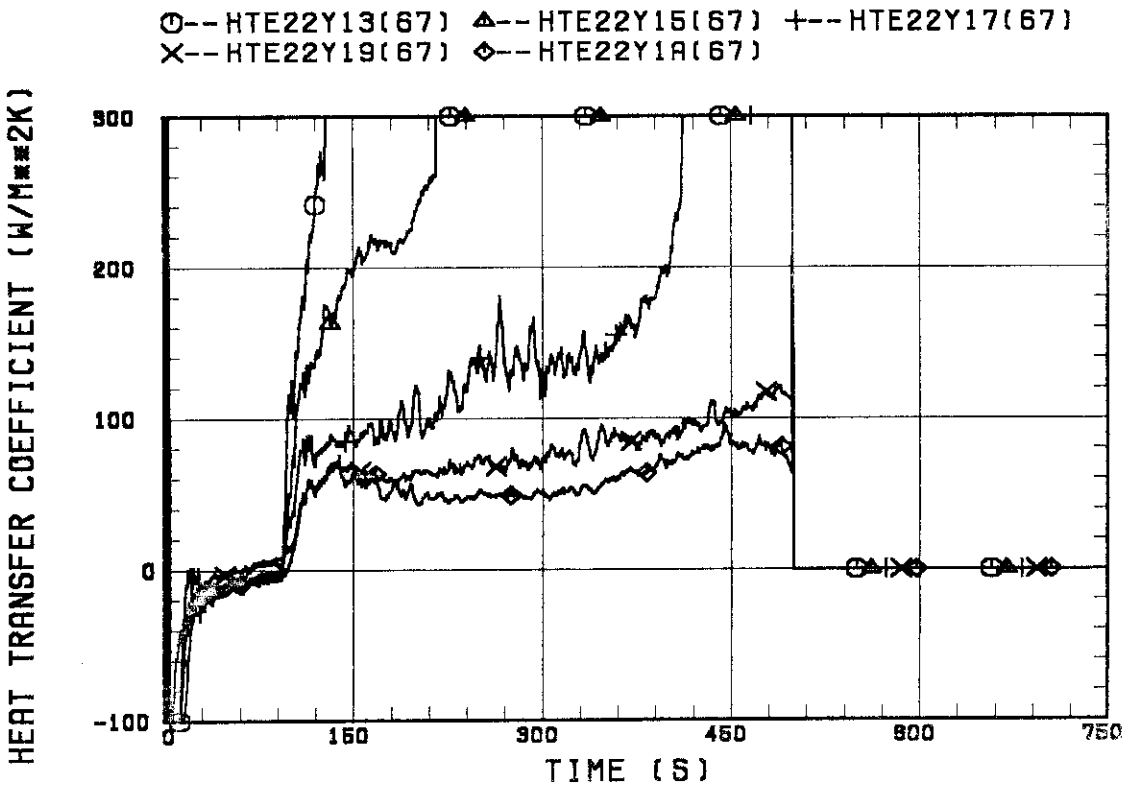

Fig. B.9 Heat transfer coefficient at various elevations along a heater rod in medium power region (B region).

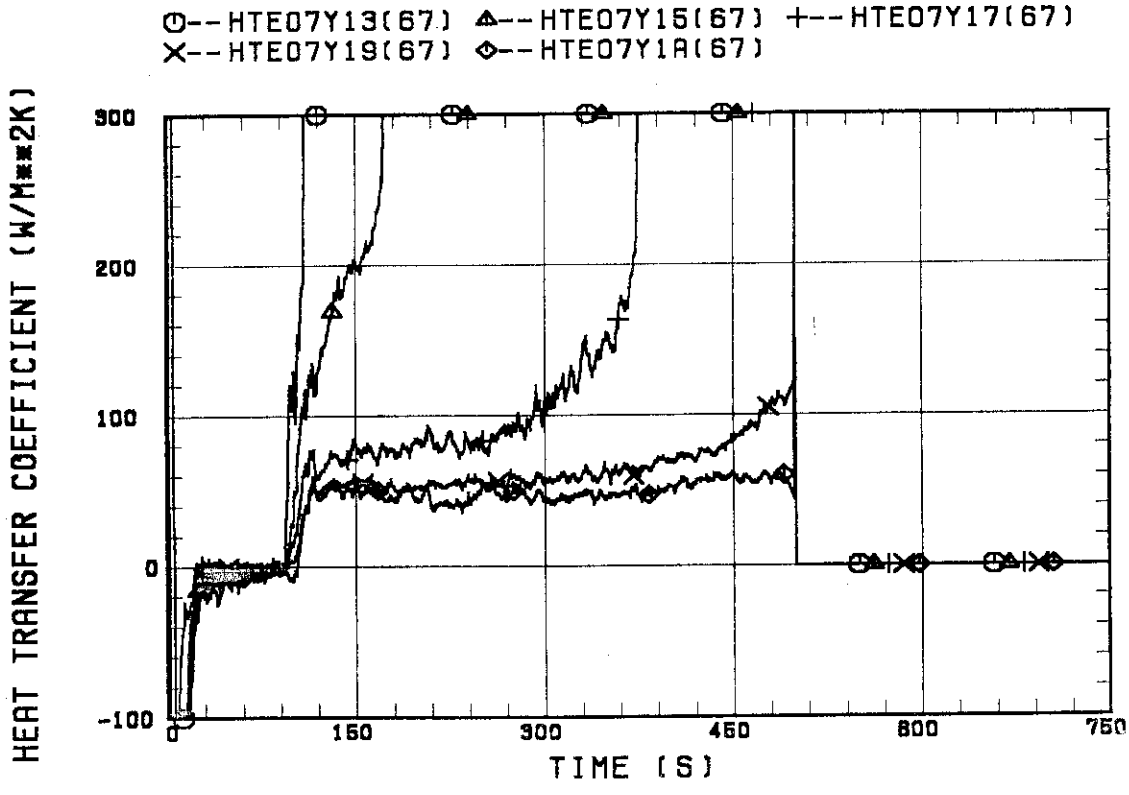

Fig. B.10 Heat transfer coefficient at various elevations along a heater rod in low power region (C region).

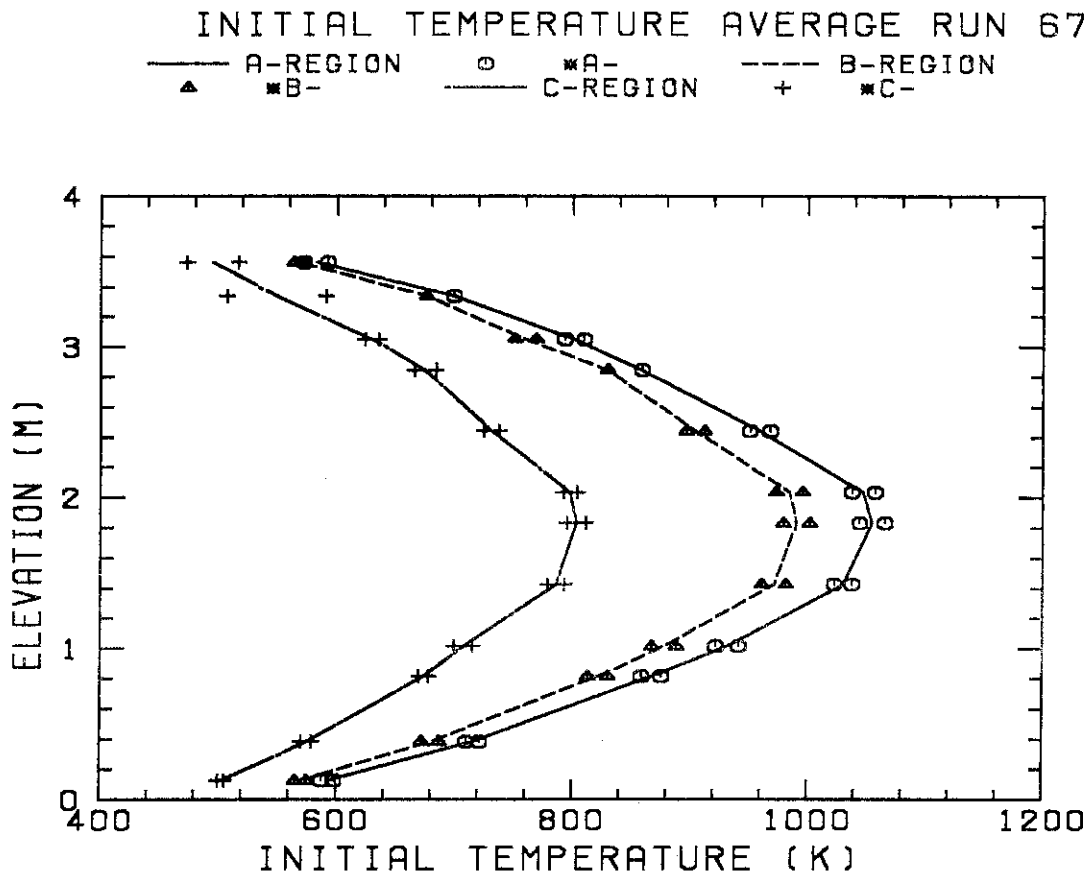

Fig. B.11 Initial clad surface temperature.

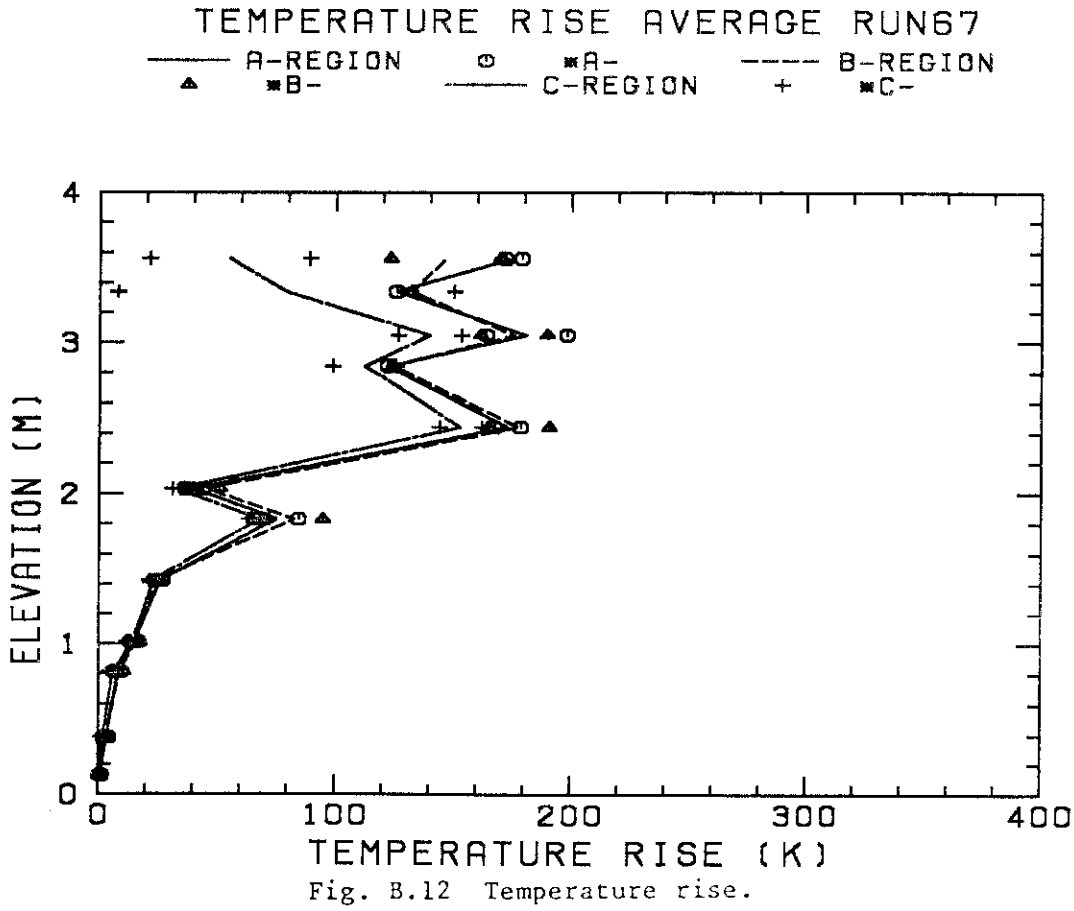

Fig. B.12 Temperature rise.

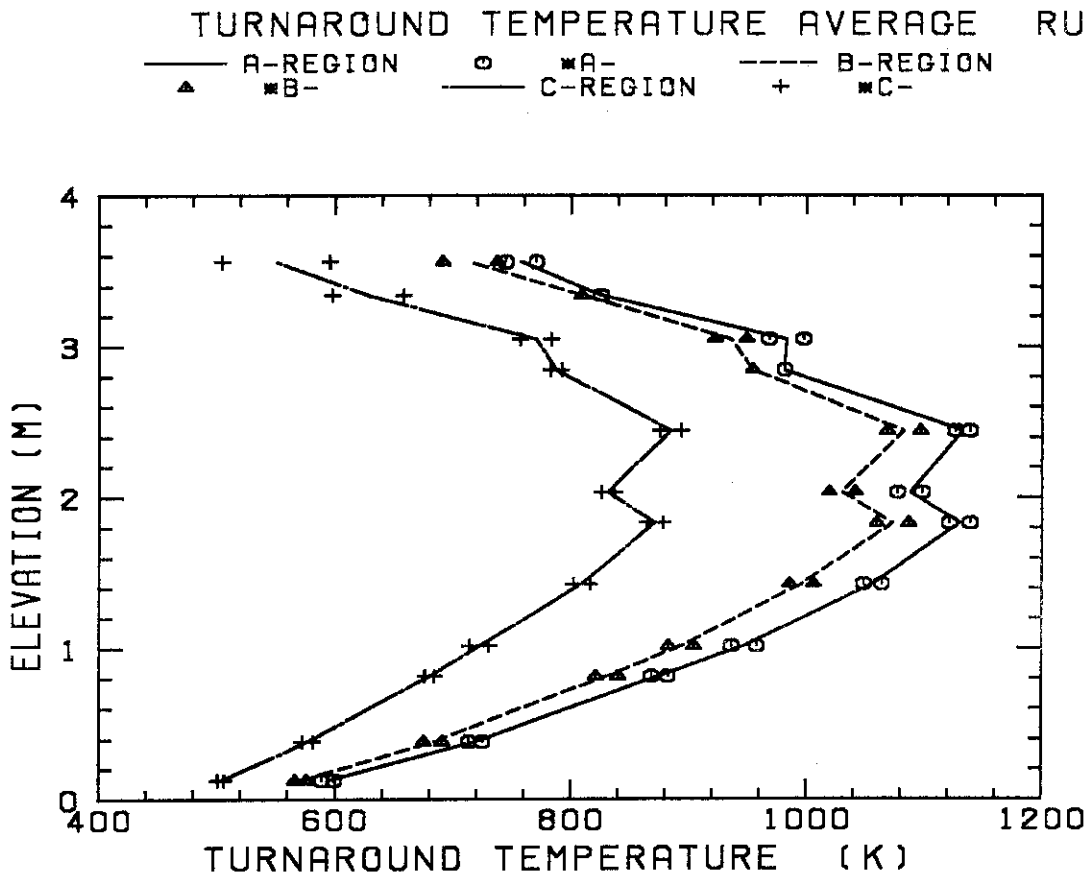

Fig. B.13 Turnaround temperature.

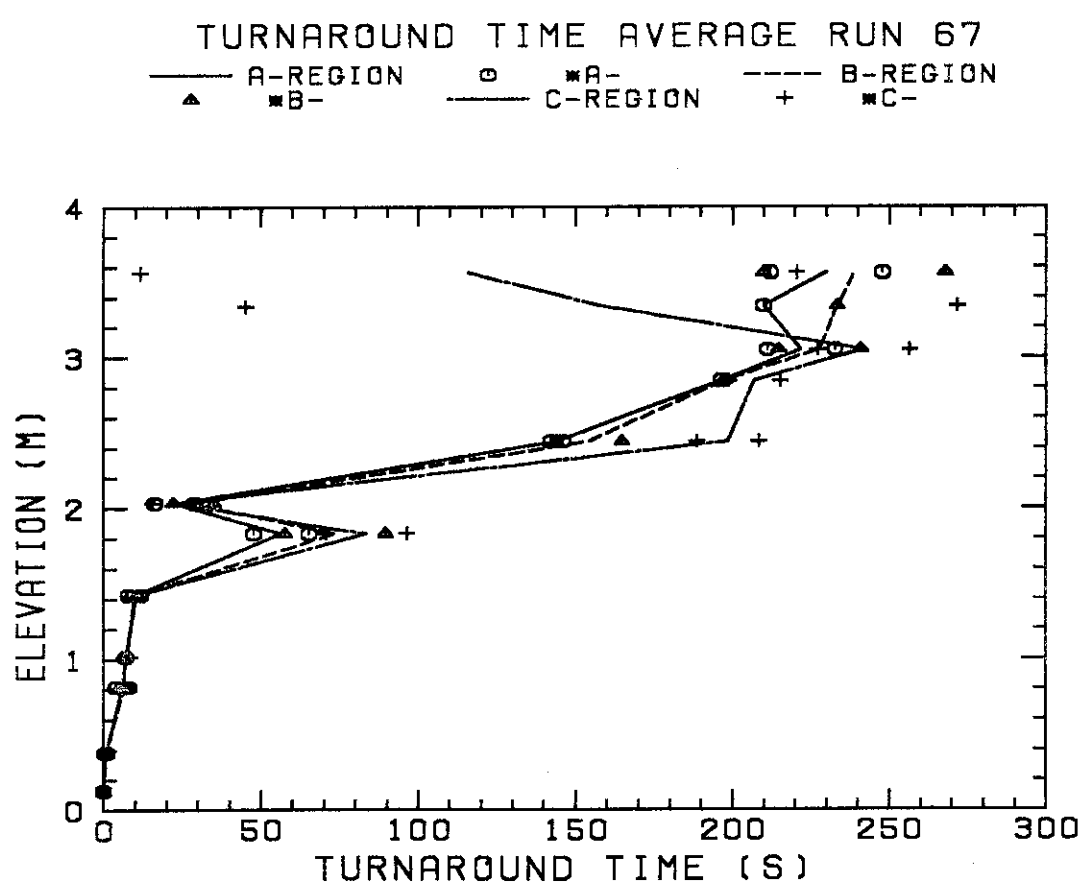

Fig. B.14 Turnaround time.

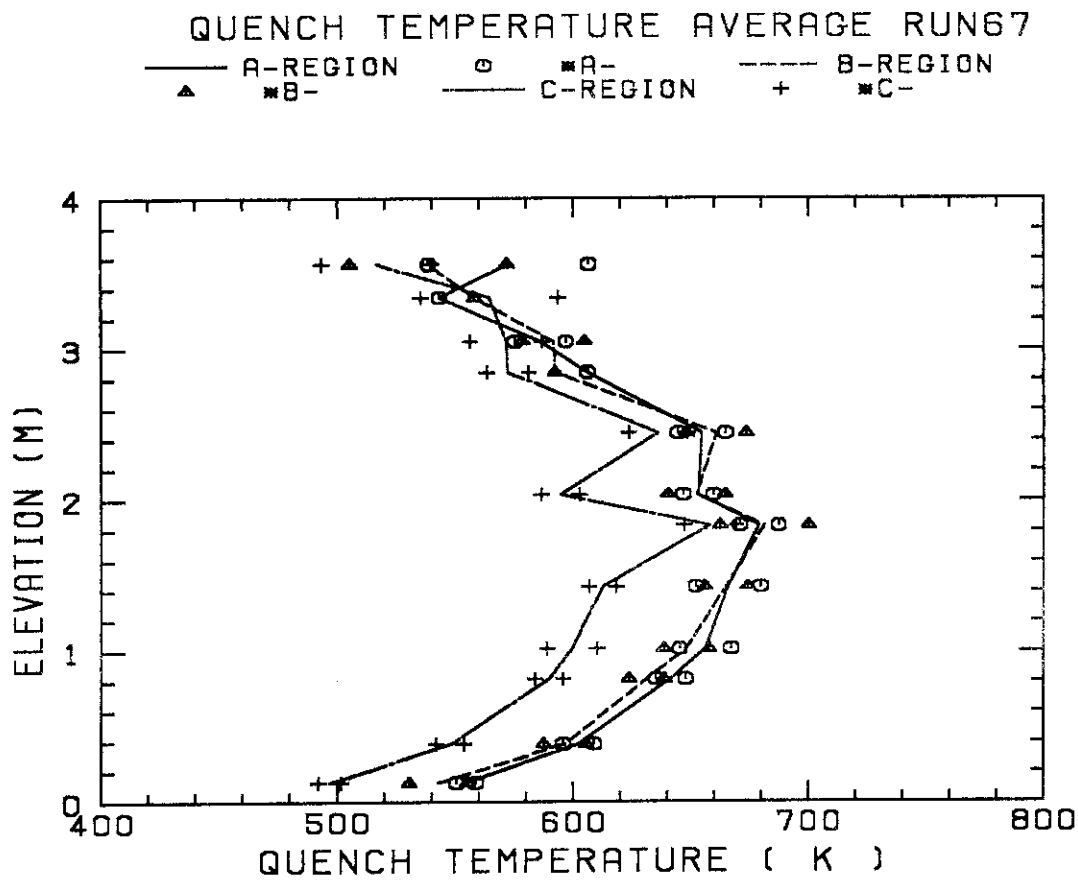

Fig. B.15 Quench temperature.

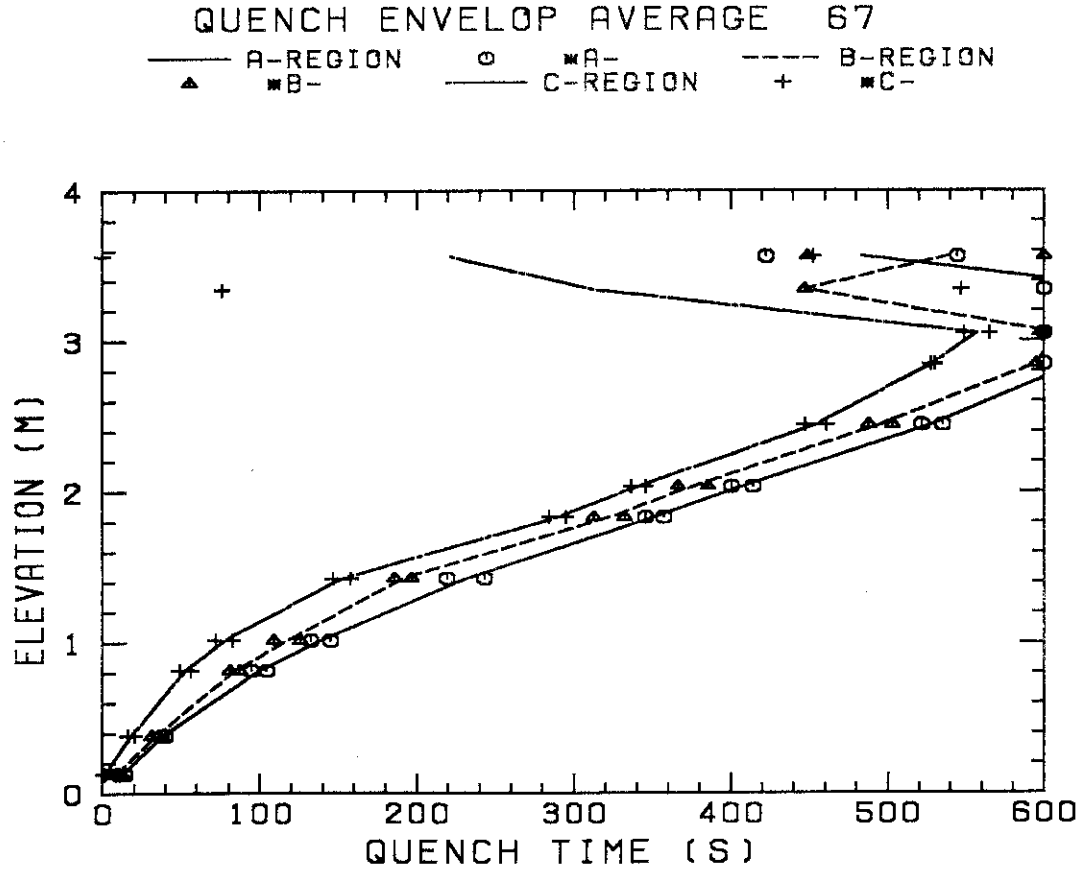

Fig. B.16 Quench time.

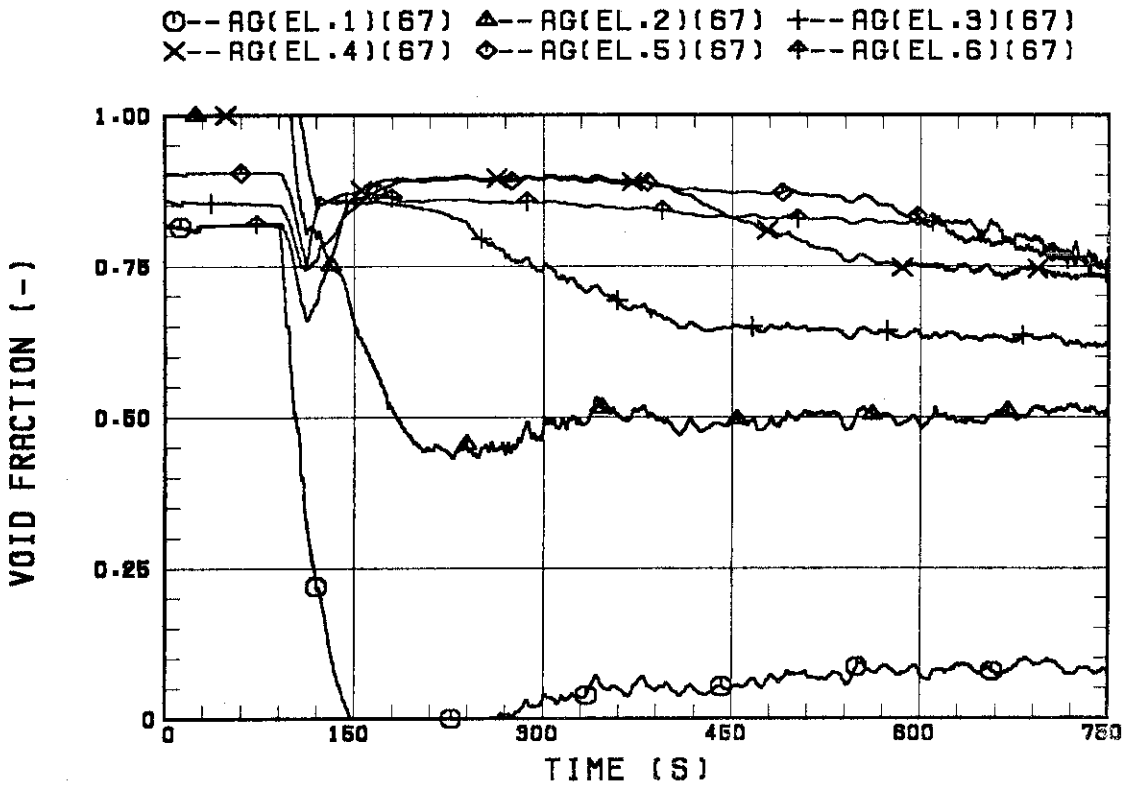

Fig. B.17 Void fraction in core.

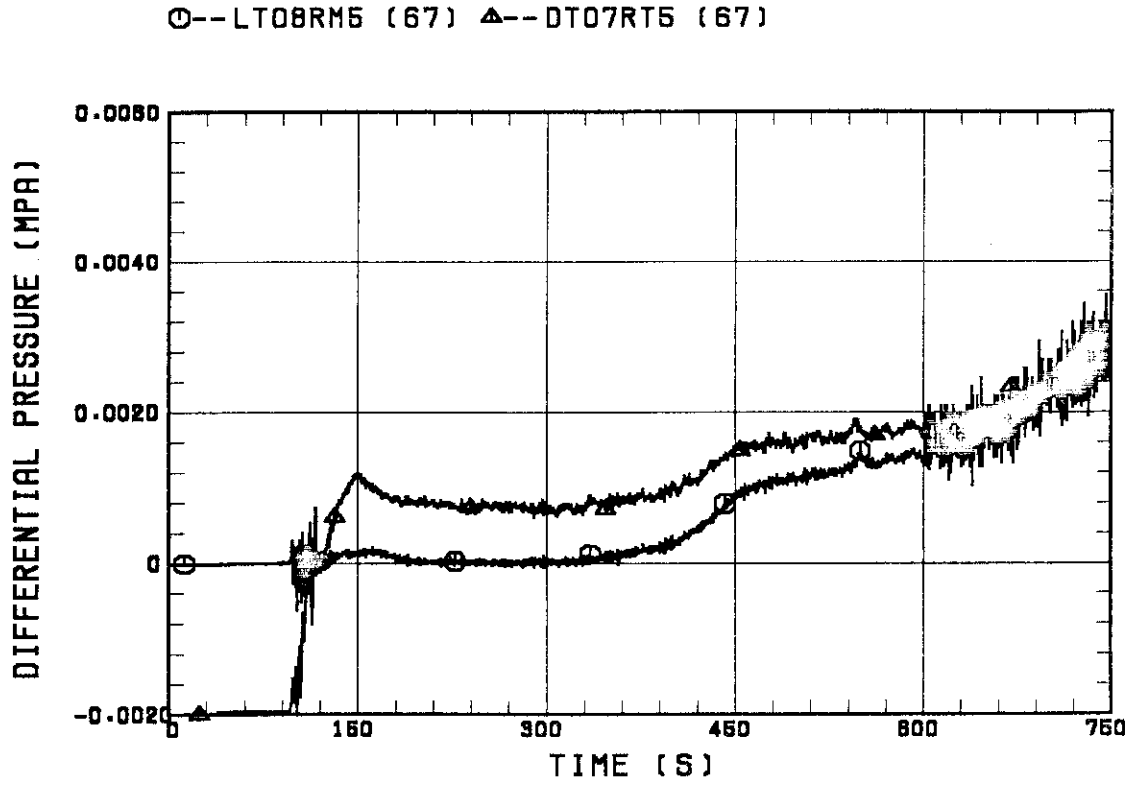

Fig. B.18 Differential pressure through upper plenum.

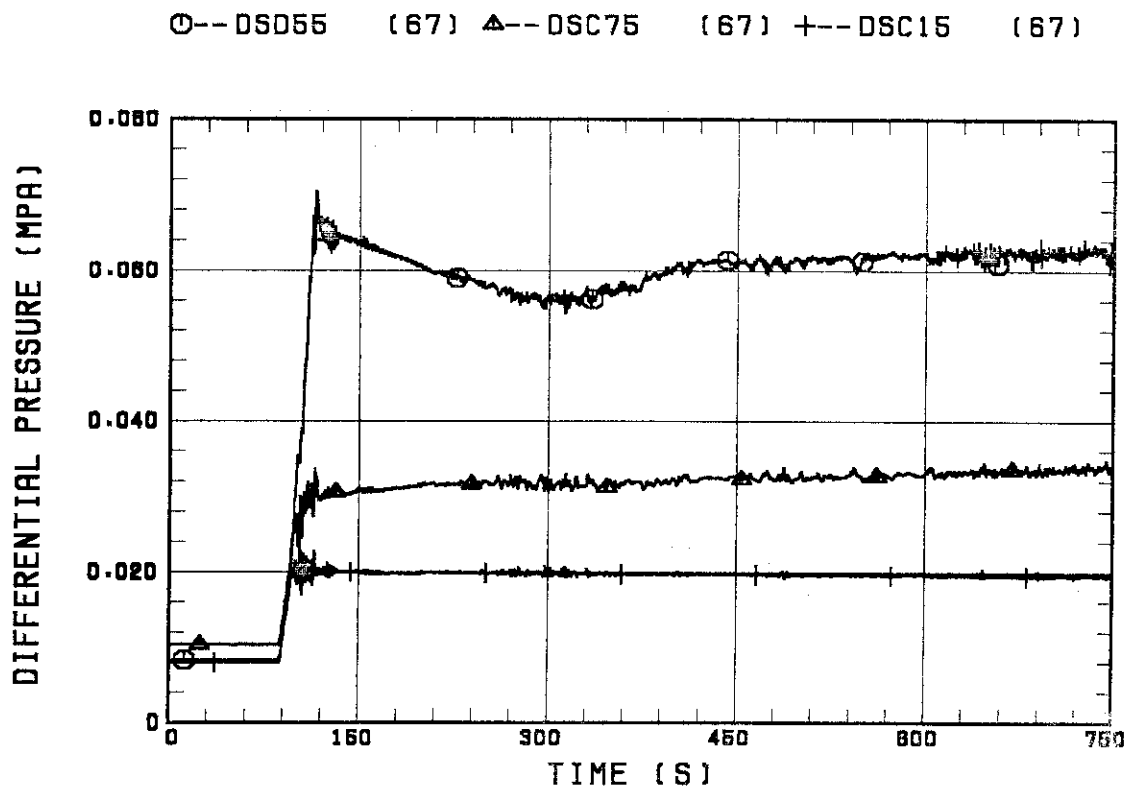

Fig. B.19 Differential pressure through downcomer, core, and lower plenum.

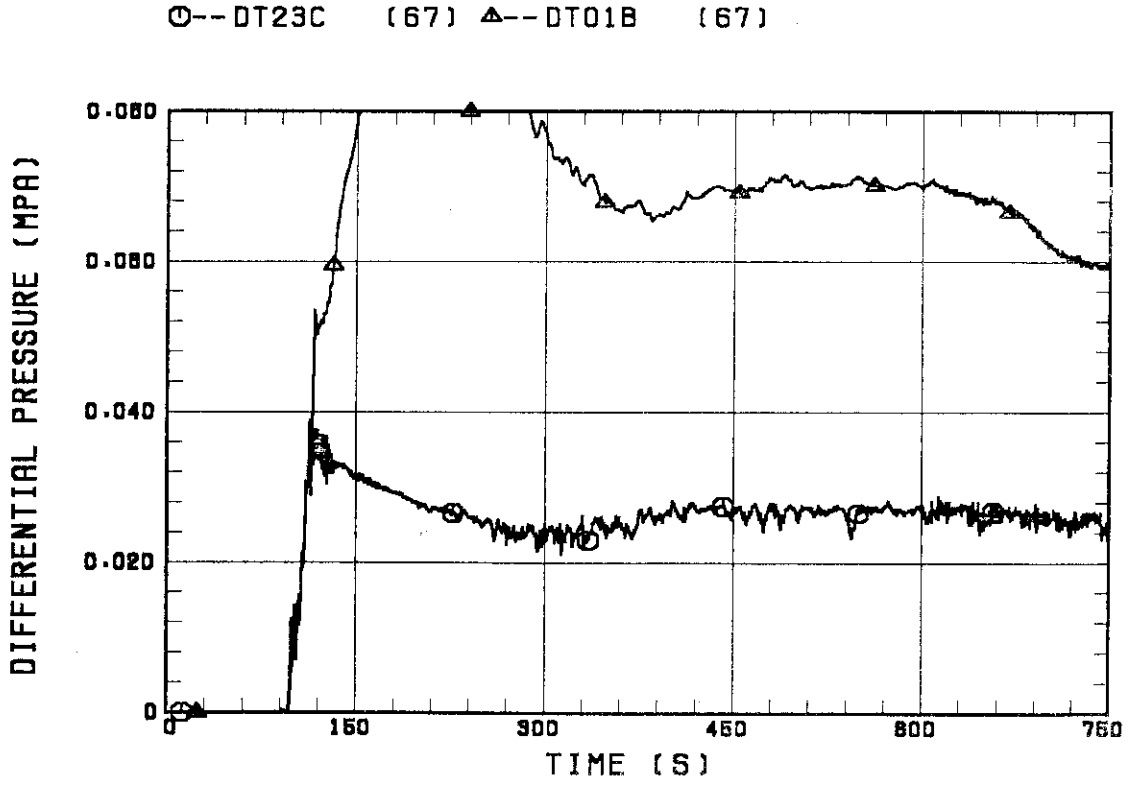

Fig. B.20 Differential pressure through intact and broken loops.

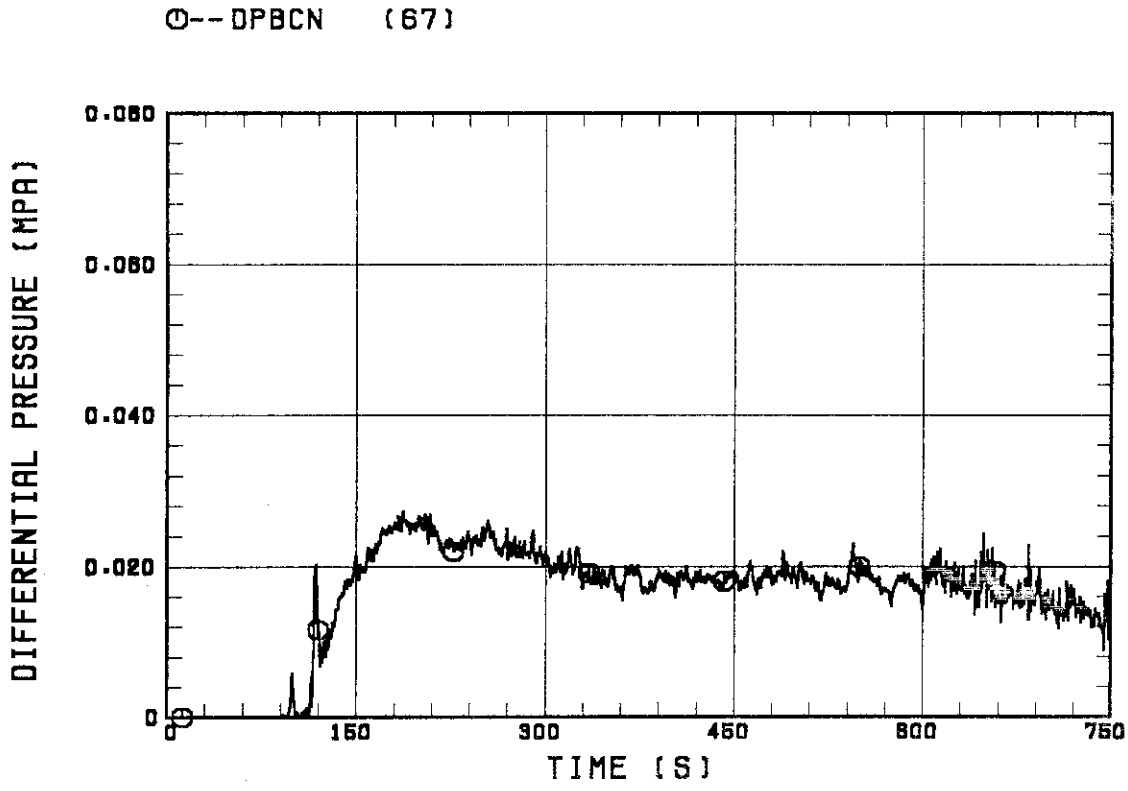

Fig. B.21 Differential pressure through broken cold leg nozzle.

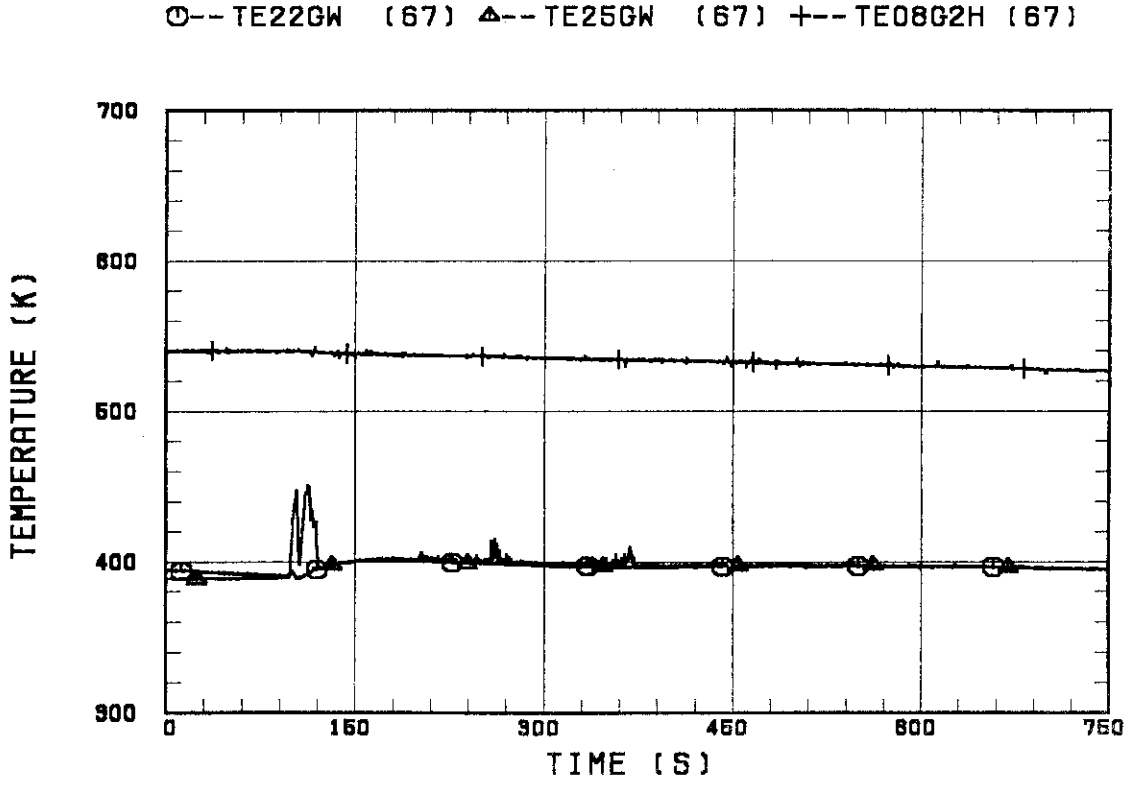

Fig. B.22 Fluid temperature in inlet plenum, outlet plenum, and secondary of steam generator 1.

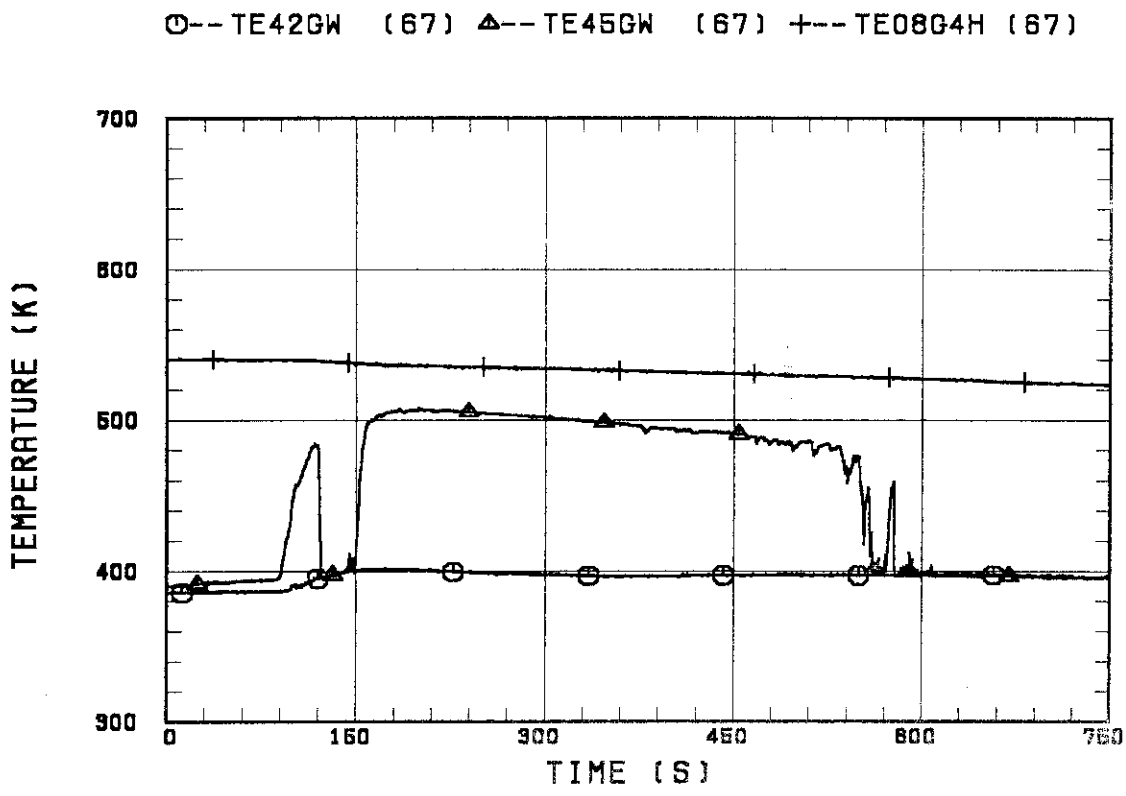

Fig. B.23 Fluid temperature in inlet plenum, outlet plenum, and secondary of steam generator 2.

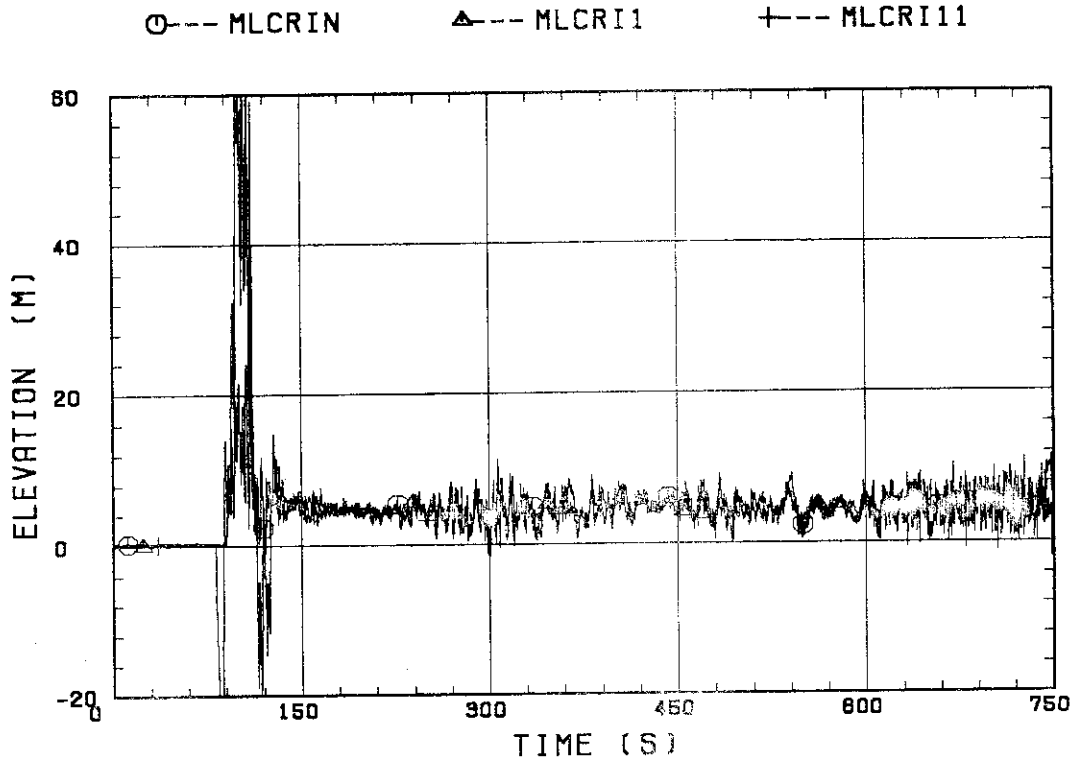

Fig. B.24 Core flooding mass flow rates evaluated with Eqs. (A.1) and

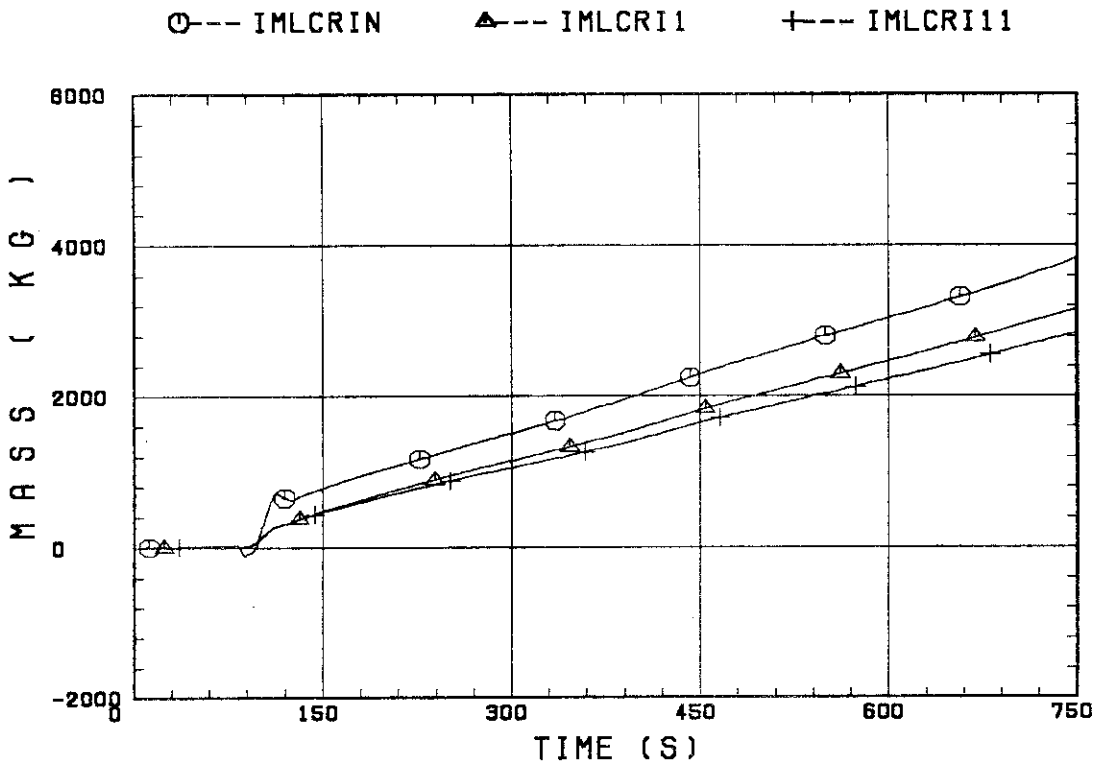

Fig. B.25 Time-integral mass flooded into core evaluated with Eqs. (A.1) and (A.2).

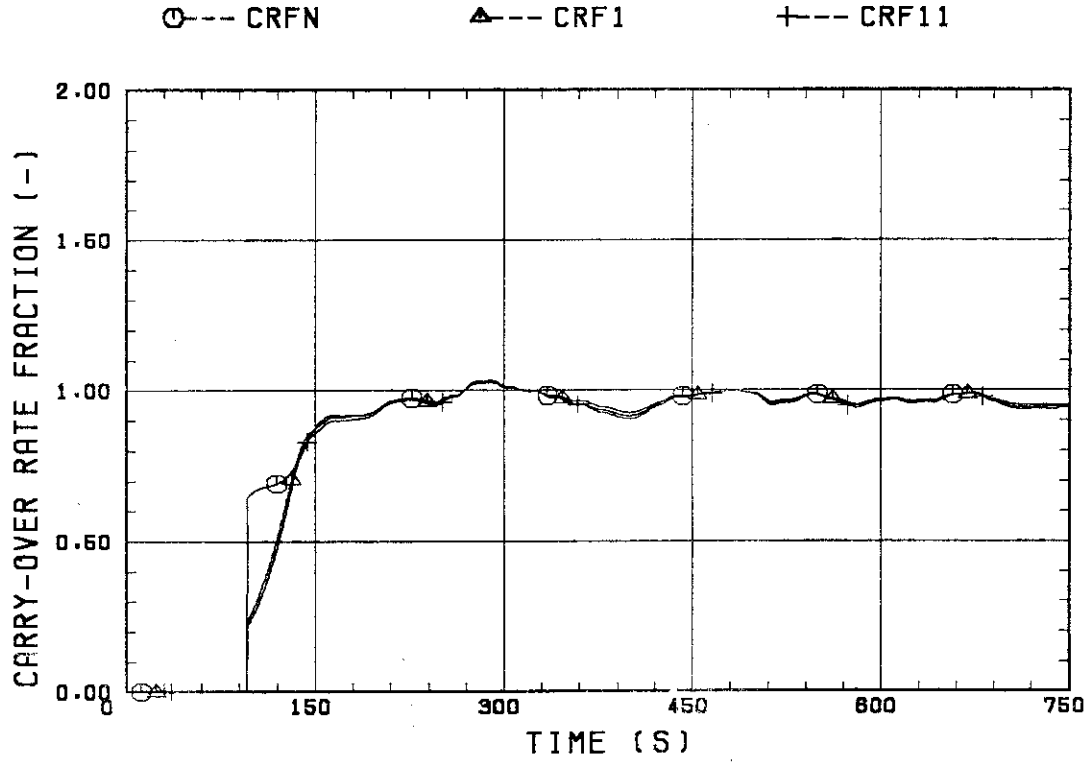

Fig. B.26 Carry-over rate fraction.

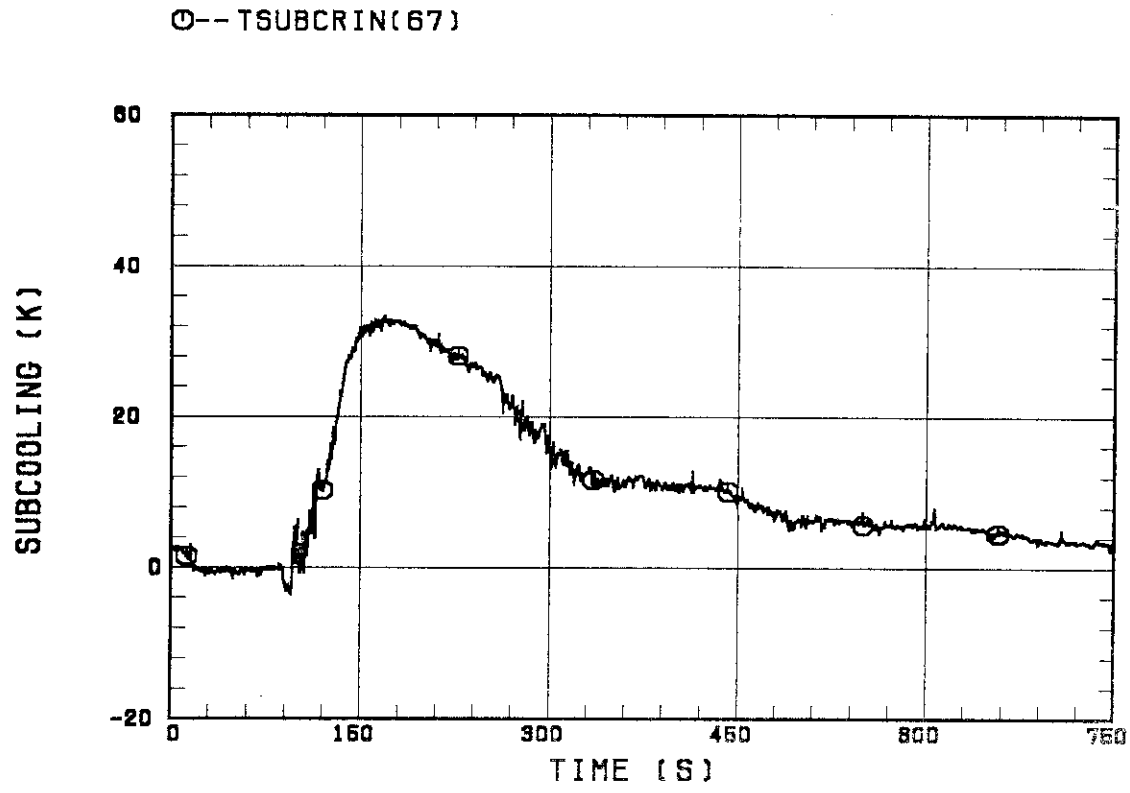

Fig. B.27 Core inlet subcooling.

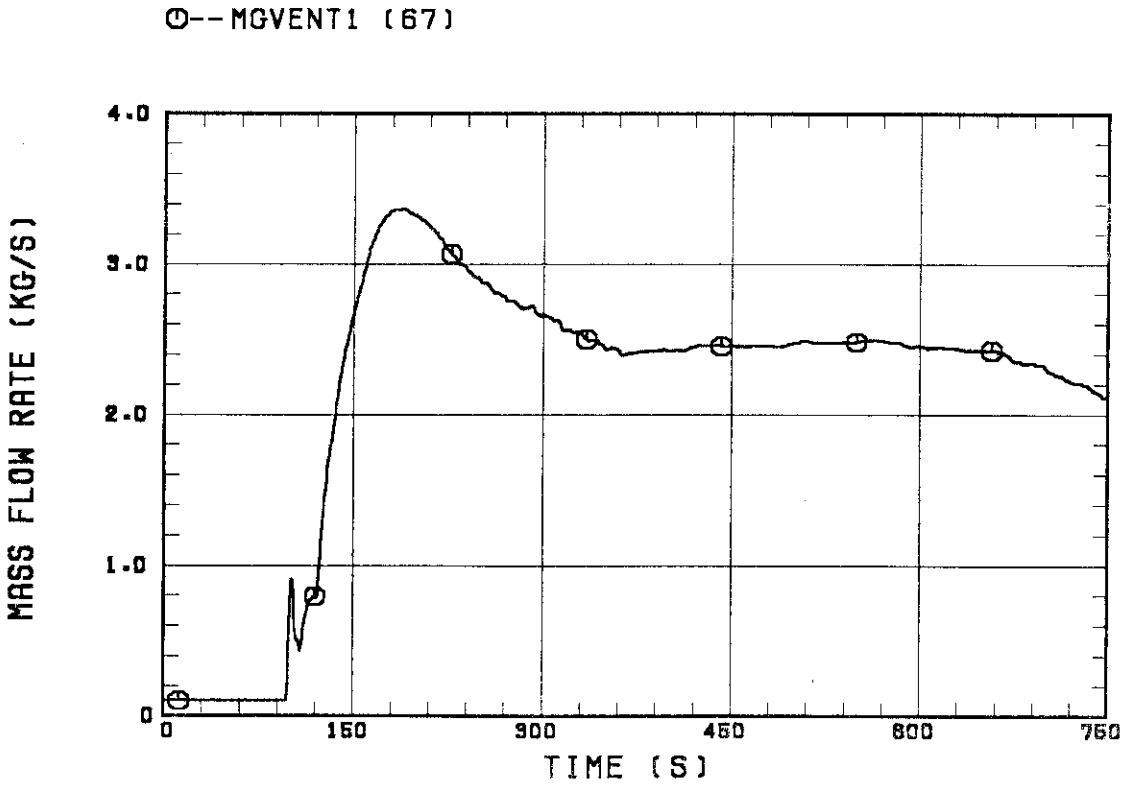

Fig. B.28 Exhausted mass flow rate from containment tank 2.